

**EXPERIMENTAL AND NUMERICAL INVESTIGATION OF A NOVEL SANDWICH
PANEL UNDER FREE AIR BLAST LOADS**

by

Mohamed Rashad Sayed Abdelsalam

M.Sc., Military Technical College, 2013

B.Sc., Military Technical College, 2005

A THESIS SUBMITTED IN PARTIAL FULFILLMENT OF
THE REQUIREMENTS FOR THE DEGREE OF

DOCTOR OF PHILOSOPHY

in

THE FACULTY OF GRADUATE AND POSTDOCTORAL STUDIES
(Civil Engineering)

THE UNIVERSITY OF BRITISH COLUMBIA
(Vancouver)

November 2019

© Mohamed Rashad Sayed Abdelsalam, 2019

The following individuals certify that they have read, and recommend to the Faculty of Graduate and Postdoctoral Studies for acceptance, the dissertation entitled:

Experimental and numerical investigation of a novel sandwich panel under free air blast loads

submitted by Mohamed Rashad Sayed
Abdelsalam in partial fulfillment of the requirements for

the degree of Doctor of Philosophy

in Civil Engineering

Examining Committee:

Prof. Tony T.Y. Yang
Supervisor

Asst Prof. Jasmin Jelovica
Supervisory Committee Member

Asst Prof. Carlos Molina Hutt
Supervisory Committee Member

Prof. Carlos Ventura
University Examiner

Prof. Frank Lam
University Examiner

Abstract

For a long time, Humanity has been suffering from explosive attacks. These attacks mainly focused on essential infrastructure, which cost much money to rebuild. However, these structures can be effectively fortified using protective systems. Sandwich panels are commonly used as protective layers for underground structures. The front panel and interlayer are designed to mitigate the blast energy from reaching the back panel (the main structure).

Traditionally, a sand layer has been used as a protective layer to absorb the blast energy. However, the sand layer has several shortcomings, including (1) rapid plastic compaction after a blast shot, (2) a heavyweight layer and, (3) difficult to control the density and water contents. In this research, a newly lightweight sandwich panel, named reinforced concrete (RC) panel - Helical springs- RC panel (RHR) sandwich panel, is proposed. RHR consists of RC panel attached to a number of helical springs and connected to RC panel (main structure). Numerical and experimental studies of the RHR under free air blast load are conducted. The performance of the RHR is compared to the Sand – RC panel (SR) and the RC panel – Sand – RC panel (RSR) protective systems against free air blast loads. SR consists of a sand layer on the top of the RC panel. The sand layer has the same depth as the front RC panel and helical springs interlayer of the RHR. Whereas, RSR uses the same configuration as RHR, except the helical springs are replaced with a sand layer. To effectively compare the performance of the three systems, an advanced Riedel-Hiermaier-Thoma (RHT) concrete model is calibrated to accurately simulate the post failure behavior of concrete panel under blast loads. The results show that the proposed RHT model can accurately model the damage level of the concrete panel under blast loads when compared with the experimental results.

The result shows that RHR has superior performance in storing the applied energy elastically when compared with the other protective systems. Lastly, a parametric study is conducted to optimize the performance of RHR. The results emphasized that RHR is an effective and efficient protective system for the roof of shallow underground structures.

Lay Summary

One of the key criteria in the underground structure is to design protective layers with minimal additive loads. Due to its abundance, sand is commonly used as a protective layer for underground structures. However, sand layers have several disadvantages, such as heavyweight, rapid compaction and difficulty in controlling its density and water content. To overcome these issues, an innovative lightweight system, which consists of reinforced concrete panels connected to helical springs and attached to the main structure, is proposed. The purpose of this research is to experimentally and numerically investigate the performance of the proposed protective system. An advanced numerical model is developed to enhance the numerical damage pattern of concrete when subjected to blast loads. Lastly, a parametric study is conducted to examine the performance of the proposed system under blast loads. The findings demonstrate that the proposed system is an effective protective layer for shallow underground structures.

Preface

This dissertation is an original intellectual product of Mohamed Rashad Sayed Abdelsalam under the supervision of Prof. Tony Yang. Mohamed Rashad Sayed Abdelsalam performed the work presented in this dissertation, including the identification and design of the research program, numerical analysis, result presentations, and writing this manuscript. Some parts of this dissertation have been published in a reputable journal, as listed below. In addition, one manuscript is under review in a prominent journal. In addition, two other manuscripts are under preparation for being submitted to two reputable journals.

- **Articles published in prominent journals:**

- 1) Parts of Chapter 3 and parts of Chapter 4 are included in the published paper: Rashad, M. and Yang, T.Y. (2018), “Numerical study of steel sandwich plates with RPF and VR cores materials under free air blast loads”, *Steel Compos. Struct., Int. J.*, 27(6), 717-725. DOI: 10.12989/scs.2018.27.6.717.

I conducted all the numerical analysis and wrote most of the manuscript under the supervision of Prof. Tony Yang.

- 2) Parts of Chapter 1 and parts of Chapter 4 are included in the published paper: Rashad, M. and Yang, T.Y. (2019), “Improved nonlinear modeling approach of simply supported PC panel under free blast load using RHT model”, *Comput. Concrete, Int. J.*, 23(2), 121-131. DOI:10.12989/cac.2019.23 .2.121.

I conducted all the numerical analysis and wrote most of the manuscript under the supervision of Prof. Tony Yang. The experimental work presented in this paper was conducted by the manufactural assistance and the technical information provided by Military Technical College, Spring and Transport Needs Manufacturing Company, and Technical Research Centre in Egypt.

- 3) Parts of Chapter 3, Parts of Chapter 4 and parts of Chapter 5 are included in the published paper: Rashad, M., Wahab, M.M.A. and Yang, T.Y. (2019), “Experimental and numerical investigation of RC sandwich panels with helical springs under free air blast loads”, Steel Compos. Struct, Int. J., 30(3), 217-230. DOI:10.12989/scs.2019.30.3.217.

I conducted all the numerical analysis and wrote most of the manuscript under the supervision of Prof. Tony Yang and the guidance from Dr. Wahab, M.M.A from Military Technical College (MTC) in Egypt. The experimental work presented in this paper was conducted by the manufactural assistance and the technical information provided by Military Technical College, Spring and Transport Needs Manufacturing Company, and Technical Research Centre in Egypt.

- **Articles published in the conference proceeding:**

- 1) Chapter 3 is included in the published paper: Rashad, M. and Yang, T.Y. (2019), “Experimental observation of the hyperdynamic behavior of RHR sandwich panel under repetitive free air blast loads using different helical springs stiffness”, Proceedings of the

607th International Conference on Civil and Architectural Engineering (ICCAE), Las Vegas, 17th – 18th May. (Also, forwarded to Journal publication).

I conducted all the work and wrote most of the manuscript under the supervision of Prof. Tony Yang. The experimental work presented in this paper was conducted by the manufacturing assistance and the technical information provided by Military Technical College, Spring and Transport Needs Manufacturing Company, and Technical Research Centre in Egypt.

- **Articles under review in a prominent journal:**

- 1) Parts of Chapter 5 and parts of Chapter 6 are included in the paper: Rashad, M. and Yang, T.Y. (2019), “Performance comparison between RHR and RSR sandwich panels against free air blast loads”, (Under review).

I conducted all the numerical analysis and wrote most of the manuscript under the supervision of Prof. Tony Yang.

- **Articles submitted in a prominent journal:**

- 1) Chapter 7 is included in the paper: Rashad, M. and Yang, T.Y. (2019), “Detailed numerical parametric study on the helical springs interlayer of RHR sandwich panel under free air blast loads” (Submitted).

I conducted all the numerical analysis and wrote most of the manuscript under the supervision of Prof. Tony Yang.

Table of Contents

Abstract.....	iii
Lay Summary	v
Preface.....	vi
Table of Contents	ix
List of Tables	xiii
List of Figures.....	xiii
List of Abbreviations	xiv
Acknowledgments	xxiii
Dedication	xxv
Chapter 1: Introduction	1
1.1 Background.....	1
1.2 Problem statement.....	2
1.3 Objectives and methodology.....	6
1.4 Dissertation overview	8
Chapter 2: Background of the blast loads and common traditional protective systems for shallow underground structure	10
2.1 An overview of blast loading nature.....	10
2.1.1 Explosion materials and Trinitrotoluene (TNT) Equivalent.....	13
2.1.2 Types of blast loading	13
2.1.3 Scaled distance law	14
2.2 An overview of SR and RSR protective systems.....	16

2.2.1	Background of the Sand layer.....	16
2.3	The proposed RHR sandwich panel.....	19
2.3.1	Background of the helical springs.....	19
2.4	Summary.....	25
Chapter 3: Experimental investigation of the performance of the RHR under free air blast		
load	26
3.1	Specimens Preparation.....	26
3.2	Test setup	32
3.3	Field blast tests.....	34
3.4	Discussion and results.....	36
3.4.1	Free air detonation of 1 Kg TNT	36
3.4.2	Free blast test of the plain concrete panel.....	37
3.4.3	Free blast tests on the RHR sandwich panel.....	39
3.4.3.1	RHR-7.....	39
3.4.3.2	RHR-9.....	42
3.4.3.3	RHR-16.....	43
3.5	Summary.....	45
Chapter 4: Analytical modeling of concrete material under hyperdynamic load		47
4.1	Literature review.....	47
4.2	Theory of RHT model.....	51
4.3	Numerical analyses on a single concrete finite element.....	53
4.4	Numerical results and discussion.....	54
4.5	Experimental and numerical application on a PC panel against a free air blast load.....	59

4.5.1	Experimental test	59
4.5.2	Numerical analysis.....	59
4.5.2.1	Numerical modeling of the explosion process.....	61
4.5.2.2	Numerical modeling of the PC panel.....	65
4.5.2.3	Mesh sensitivity analysis	69
4.5.3	Comparison between the experimental and numerical results.....	71
4.6	Summary.....	79
Chapter 5: Numerical investigation of the performance of the RHR under free air blast load		
.....		80
5.1	Literature review.....	80
5.2	Material modeling of the RHR sandwich panel.....	82
5.2.1	RC panels modeling.....	83
5.2.2	Helical spring and rebar modeling.....	83
5.3	Mesh sensitivity analysis	87
5.3.1	Air block	88
5.3.2	RC panels	91
5.3.3	Helical springs	92
5.3.4	Rebar.....	94
5.4	Numerical study of the RHR sandwich panels	94
5.5	Discussion of the results	96
5.6	Summary.....	110
Chapter 6: Comparison between the SR, RSR and RHR protective systems.....		112
6.1	General.....	113

6.2	Numerical modeling of the traditional (SR and RSR) protective systems under free air blast loads.....	113
6.2.1	Dry sand material modeling.....	116
6.2.1.1	Validation of the dry sand modeling.....	120
6.3	Comparison results and discussion.....	123
6.4	Summary.....	149
Chapter 7: Parametric study on the performance of the RHR under free air blast loads		152
7.1	Parametric study factors.....	152
7.2	Numerical results and discussion.....	159
7.2.1	Displacement analysis.....	161
7.2.2	Energy dissipation analysis.....	166
7.3	Summary.....	174
Chapter 8: Conclusions and future work		176
8.1	Summary and conclusions.....	176
8.2	Recommendations for future work.....	182
Bibliography		184

List of Tables

Table 3.1 The blast field test matrix	28
Table 3.2 The Specifications of helical springs used in the blast field tests.....	29
Table 3.3 Maximum displacement of RHR-7 under different blast loads	42
Table 3.4 Maximum displacement of the RHR-16 under different blast loads	45
Table 4.1 The main effective parameters of the default and newly proposed RHT models in this study	53
Table 4.2 Material data of the air and TNT used in modeling (ANSYS-AUTODYN, 2005).....	62
Table 4.3 Summary of the JWL parameters used to model TNT	63
Table 4.4 Material data of concrete used in this study (ANSYS-AUTODYN, 2005).....	68
Table 4.5 The default, the previous and the newly proposed RHT parameters used in this numerical study	76
Table 5.1 Material data of helical springs and rebar used in this research (ANSYS-AUTODYN, 2005)	87
Table 5.2 The difference between the helical spring stiffness measured in the factory and that obtained from static analyses	93
Table 6.1 Material data of the dry sand used in this study (ANSYS-AUTODYN, 2005).....	119
Table 6.2 The experimental and numerical crater diameter values for the dry sand test	122
Table 6.3 Comparison between the weight of the front layer and interlayer of the SR, RSR and RHR systems.....	124
Table 7.1 Outlines of the RHR sandwich panel parameters used in this study	156
Table 7.2 The numerical results for the RHR sandwich panel	167

List of Figures

Figure 1.1 A visualization for the annual number of terrorist attacks globally (Roser et al., 2019)	1
Figure 2.1 Typical blast pressure time history and amplitude frequency relationship of different structural loadings (Goel and Matsagar, 2014).....	12
Figure 2.2 Relationship between the positive pressure phase and the standoff distance (Karlos and Solomon, 2013).....	12
Figure 2.3 Unconfined non-contact blast loading categorization (Yandzio and Gough, 1999) ...	14
Figure 2.4 Positive phase shock wave parameters for a spherical TNT explosion in free air at the sea level (TM5-1300, 1990).....	15
Figure 2.5 Schematic representation of the RSR wall (UFC 3-340-02, 2008).....	17
Figure 2.6 Relationship between the density and pressure for the dry sand (ANSYS-AUTODYN, 2005)	18
Figure 2.7 Schematic representation of a shock isolation system using helical springs (TM5-1300, 1990)	21
Figure 2.8 Compression helical spring mounts (TM5-1300, 1990).....	21
Figure 2.9 Helical springs	23
Figure 3.1 Reinforced concrete formworks	30
Figure 3.2 Configurations of the three RHR sandwich panels and the location of the helical springs in each interlayer	31
Figure 3.3 Test setup of the RHR-7 under 1 Kg TNT at SoD of 1 m.....	32
Figure 3.4 Piezotronics (PCB) pressure smart sensor.....	33

Figure 3.5 Amplifier	34
Figure 3.6 Calibration sheet.....	34
Figure 3.7 Experimental test setup of the free air explosion test of 1Kg TNT at a SoD of 1 m...	35
Figure 3.8 Testing set up of PC panel test	36
Figure 3.9 Field reading and the CONWEP results of detonating of 1 Kg TNT at a SoD of 1 m	37
Figure 3.10 Damage pattern of the PC panel after the explosion process	39
Figure 3.11 Free air explosion process scenes of RHR-7 under 1 kg TNT at a SoD of 1 m.....	40
Figure 3.12 Experimental observation on the RHR-7 after applying different blast loads	41
Figure 3.13 Experimental observation on the RHR-9 under 7.5 Kg TNT at SoD of 1 m	43
Figure 3.14 Experimental observation on the RHR-16	45
Figure 4.1 Three strength surfaces of the RHT model (Riedel <i>et al.</i> 1999)	51
Figure 4.2 Uniaxial numerical compression test on a single concrete finite element.....	54
Figure 4.3 Axial stress-strain curves of the default and proposed RHT models for tension	56
Figure 4.4 Axial stress-strain curves of the default and proposed RHT models for compression	57
Figure 4.5 Damage pattern of the PC panel after applying the blast load	59
Figure 4.6 A quarter numerical model of the PC panel subjected to free air blast load.....	61
Figure 4.7 Remapping of the air and TNT charge from 1D to 3D	64
Figure 4.8 Pressure time histories of 1 kg TNT detonated at a SoD of 1 m.....	65
Figure 4.9 Peak overpressure value of a spherical charge of 1 Kg TNT detonated at a SoD of 1 m	65
Figure 4.10 Concrete equation of state (Herrmann 1969)	67
Figure 4.11 Effect of changing air element size on the peak overpressure value of detonating 4 Kg TNT at a SoD of 1 m.....	70

Figure 4.12 Damage levels at the midpoint of the front and back faces of the PC panel of the experimental test and that observed from the numerical simulations using the default, newly proposed and previously proposed RHT models	73
Figure 4.13 Damage level time history at the midpoint of the front and back faces of PC panel using the default RHT parameters and proposed RHT parameters	74
Figure 4.14 Experimental and numerical damage pattern and crack trajectory observations on the PC panel	79
Figure 5.1 Helical spring modeling methods	82
Figure 5.2 A FE model of the RHR sandwich panel with 16 helical springs	83
Figure 5.3 Kinds of helical spring simulation.....	85
Figure 5.4 Comparison of peak overpressure values	89
Figure 5.5 Effect of changing the element size on the peak overpressure value for detonating 1 Kg TNT at a SoD of 1 m.....	90
Figure 5.6 Effect of changing the element size on the peak overpressure value for detonating 5 Kg TNT at a SoD of 1 m.....	90
Figure 5.7 Effect of changing the element size on the peak overpressure value for detonating 10 Kg TNT at a SoD of 1 m.....	91
Figure 5.8 Helical spring stiffness obtained from the static numerical analyses.....	93
Figure 5.9 Helical spring stiffness for different element sizes	93
Figure 5.10 A quarter model of RHR sandwich panel.....	95
Figure 5.11 Comparison of peak overpressure values at the front face of the front RC panel, midpoint of the RHR sandwich panel and back face of the back RC panel	96

Figure 5.12 Comparison between the maximum displacements of the front RC panel obtained from the numerical analysis and that measured in the field.....	97
Figure 5.13 Damage contours of the front and back RC panels of the RHR sandwich panel subjected to 1, 5 and 10 Kg TNT at SoD of 1 m	98
Figure 5.14 Damage level-time histories at the midpoint of the front and back RC panels of the RHR sandwich panel under different free air blast loads	99
Figure 5.15 Experimental and numerical damage observation of the front RC panel of the RHR sandwich panel under three different blast loads of 1, 5 and 10 Kg TNT at a SoD of 1 m.....	100
Figure 5.16 Internal energy time histories of the front and back RC panel under the three blast loads	102
Figure 5.17 Internal energy time histories of the helical springs interlayer under the three blast loads	103
Figure 5.18 Total energy, internal energy and kinetic energy time histories of the front RC panel, helical springs interlayer and back RC panel in the case of 1 Kg TNT at a SoD of 1 m.....	105
Figure 5.19 Total energy, internal energy and kinetic energy time histories of the front RC panel, helical springs interlayer and back RC panel in the case of 5 Kg TNT at a SoD of 1 m.....	106
Figure 5.20 Total energy, internal energy and kinetic energy time histories of the front RC panel, helical springs interlayer and back RC panel in the case of 10 Kg TNT at a SoD of 1 m.....	107
Figure 5.21 Maximum plastic work done for the front and back RC panels under the three blast loads	109
Figure 5.22 The Material status of the helical spring under 10 kg TNT	110
Figure 6.1 Full numerical configuration of the a) SR, b) RSR and c) RHR protective systems	115
Figure 6.2 A quarter numerical model of the RSR sandwich panel	116

Figure 6.3 Dry sand material properties as used in the numerical modeling.....	119
Figure 6.4 Test setup of the dry sand experiment (Bergeron et al., 1998).....	120
Figure 6.5 A half numerical model developed in this study to simulate the dry sand experimental test.....	121
Figure 6.6 The trend of the a) experimental (Bergeron et al., 1998) and b) numerical crater formation of the dry sand test	122
Figure 6.7 Material status of the components of a quarter model of the RHR sandwich panel after subjecting to three different blast loads	125
Figure 6.8 Material status of the sand layer and back RC panel after applying three different blast loads on the SR protective system	126
Figure 6.9 Material status of the front RC panel, sand interlayer and back RC panel after applying three different blast loads on the RSR sandwich panel.....	128
Figure 6.10 Damage contours of the back RC panel of the SR, RSR and RHR systems when subjected to 1, 5 and 10 Kg TNT at a SoD of 1 m.....	130
Figure 6.11 Comparison of the maximum plastic work done by the front RC panel of the RSR and RHR sandwich panels	131
Figure 6.12 Comparison of the maximum plastic work done by the back RC panel of the SR, RSR and RHR protective systems	132
Figure 6.13 Comparison between the total, internal and kinetic energy absorbed by the components of the RSR and RHR sandwich panels under 1 Kg TNT at a SoD of 1 m.....	136
Figure 6.14 Comparison between the total, internal and kinetic energy absorbed by the components of the RSR and RHR sandwich panels under 5 Kg TNT at a SoD of 1 m.....	137

Figure 6.15 Comparison between the total, internal and kinetic energy absorbed by the components of the RSR and RHR sandwich panels under 10 Kg TNT at a SoD of 1 m	138
Figure 6.16 The total, internal and kinetic energy absorbed by the sand layer of the SR protective system and the back RC panel of the SR and RHR systems under 1 Kg TNT at a SoD of 1 m	140
Figure 6.17 The total, internal and kinetic energy absorbed by the sand layer of the SR protective system and the back RC panel of the SR and RHR systems under 5 Kg TNT at a SoD of 1 m	141
Figure 6.18 The total, internal and kinetic energy absorbed by the sand layer of the SR protective system and the back RC panel of the SR and RHR systems under 10 Kg TNT at a SoD of 1 m	141
Figure 6.19 The maximum total energy dissipated by the SR, RSR and RHR protective systems under the three different blast loads.....	143
Figure 6.20 Ratio of the total energy dissipated by each component of the SR, RSR and RHR protective systems for the three different blast loads.....	145
Figure 6.21 Stress time histories at the center of the upper face of the front layer (black color) and back RC panel (red color) for the SR, RSR and RHR systems when subjected to 1 Kg TNT at a SoD of 1 m	147
Figure 6.22 Stress time histories at the center of the upper face of the front layer (black color) and back RC panel (red color) for the SR, RSR and RHR systems when subjected to 5 Kg TNT at a SoD of 1 m	148
Figure 6.23 Stress time histories at the center of the upper face of the front layer (black color) and back RC panel (red color) for the SR, RSR and RHR when subjected to 10 Kg TNT at a SoD of 1 m	149
Figure 7.1 Different helical spring arrangements used in the parametric study	155

Figure 7.2 Effect of changing the wire diameter and the number of helical springs on the total stiffness of the interlayer..... 160

Figure 7.3 Effect of changing the interlayer weight on the total stiffness of the interlayer 160

Figure 7.4 Relationship between the front RC panel displacements and wire diameters when using different numbers of helical springs under different scaled distance of 1, 0.58 and 0.46 m/Kg^{1/3} 163

Figure 7.5 Effect of changing the scaled distance on the reduction percentage of the maximum displacement of the front RC panel using different numbers of helical springs with different wire diameters 164

Figure 7.6 Relationship between the maximum displacements of the front RC panel and total stiffness of the interlayer under different scaled distance of 1, 0.58 and 0.46 m/Kg^{1/3} 165

Figure 7.7 Relationship between the plastic work done by the front and back RC panel of the RHR-7 and the interlayer stiffness under the three scaled distance of 0.46, 0.58 and 1 m/Kg^{1/3} 171

Figure 7.8 Relationship between the plastic work done by the front and back RC panel of the RHR-9 and the interlayer stiffness under the three scaled distance of 0.46, 0.58 and 1 m/Kg^{1/3} 171

Figure 7.9 Relationship between the plastic work done by the front and back RC panel of the RHR-16 and the interlayer stiffness under the three scaled distance of 0.46, 0.58 and 1 m/Kg^{1/3} 172

Figure 7.10 Relationship between the plastic work done by the front and back RC panel of the RHR-25 and the interlayer stiffness under the three scaled distance of 0.46, 0.58 and 1 m/Kg^{1/3} 172

Figure 7.11 Total energy dissipated by Front RC panel, helical springs interlayer and back RC panel under three different scaled distance 174

List of Abbreviations

ASCE	American Society of Civil Engineers
BETA-B-500	Betonobojnaja Aviacionnaja bomb 500-kilogram
C-4	Composition No. 4 (Plastic Explosive)
CONWEP	Conventional weapons calculation software
DL	Damage Level
DOB	Depth of burial
EOS	Equation of State
Euler-FCT	Euler-Flux Corrected Transport
FEM	Finite element method
ICCAE	International Conference on Civil and Architectural Engineering
JWL	Jones-Wilkins-Lee
MTC	Military Technical College
PC	Plain concrete
PCB	PicoCoulomB
RC	Reinforced concrete
RHR	RC panel – Helical springs - RC panel
RHT	Riedel-Hiermaier-Thoma
RSR	RC panel – Sand – RC panel
SoD	Standoff distance
SR	Sand – RC panel
TM5	Technical manual 5

TNT	Trinitrotoluene
UFC	Unified Facilities Criteria
UI	Unitless

Acknowledgments

First and foremost, I would like to thank ALLAH the almighty for providing me with the strength, patience, knowledge and opportunity to undertake this research study and to complete it successfully. Without his blessings and mercy, this dissertation would not have been achieved.

I, lovingly, would like to extend wholeheartedly my love and appreciation to the soul of my dear father, Prof. Rashad Sayed Abdelsalam, who wished to see this happen and Inshaa Allah, he is in heaven now. My parent's way of bringing me up is the main reason for my success. Certainly, I am truly grateful to my mother Nadia Mohamed (school principal). Without her love, dedication, endless support, and prayers, this work has never been completed. Despite the long distance between us, my brothers and sisters have been a constant source of unconditional love, support, endless patience and encouragement in every step of my life. Words cannot express my heartfelt appreciation to them.

I am thankful to my wife Eman for the love, support and care she had provided me during this program. I thank my son Omar and my upcoming daughter for providing a cheerful atmosphere at home and for entertaining, encouraging and helping me during this work.

I would like to express my sincere gratitude towards my supervisor Prof. Tony Yang for encouraging and guiding me throughout my Ph.D. program. I have been gratefully fortunate to have his supervision on the hard moments of life. I am profoundly grateful to him for giving me the freedom and guidance in choosing and exploring the way in the ocean of knowledge while

providing me with fruitful opportunities on this adventurous journey. Indeed, this thesis would have not been possible without his insightful support and comments.

I offer my enduring gratitude to the other members of my supervisory committee, Dr. Jasmin Jelovica and Dr. Carlos Molina Hutt. Their feedback was essential to the success of this work.

I would like to express my special appreciation and deepest gratitude to Professor Carlos Ventura for the encouragement, continuous support and advice that he provided during my PhD program. It has been a pleasure to know you.

My appreciation extends to all my colleagues and friends for their help and joyful company during this journey.

To my beloved family and to those who have suffered from the blast attacks

بِسْمِ اللَّهِ الرَّحْمَنِ الرَّحِيمِ

Al-Quraan – Surat AlFatiha – Verse 1

Chapter 1: Introduction

1.1 Background

Terrorist activities have increased around the world. Most of these attacks are directed to vital structures in the form of explosion shots. Figure 1.1 shows a visualization for the annual number of terrorist attacks all over the world by 2017 (Roser et al., 2019). These attacks have caused a significant number of victims and financial losses. To mitigate the risks by blast load, different types of protective layers for underground structures have been developed over the last century, which commonly consists of sand layers and/or reinforced concrete panels (TM5-1300, 1990; UFC 3-340-02, 2008).

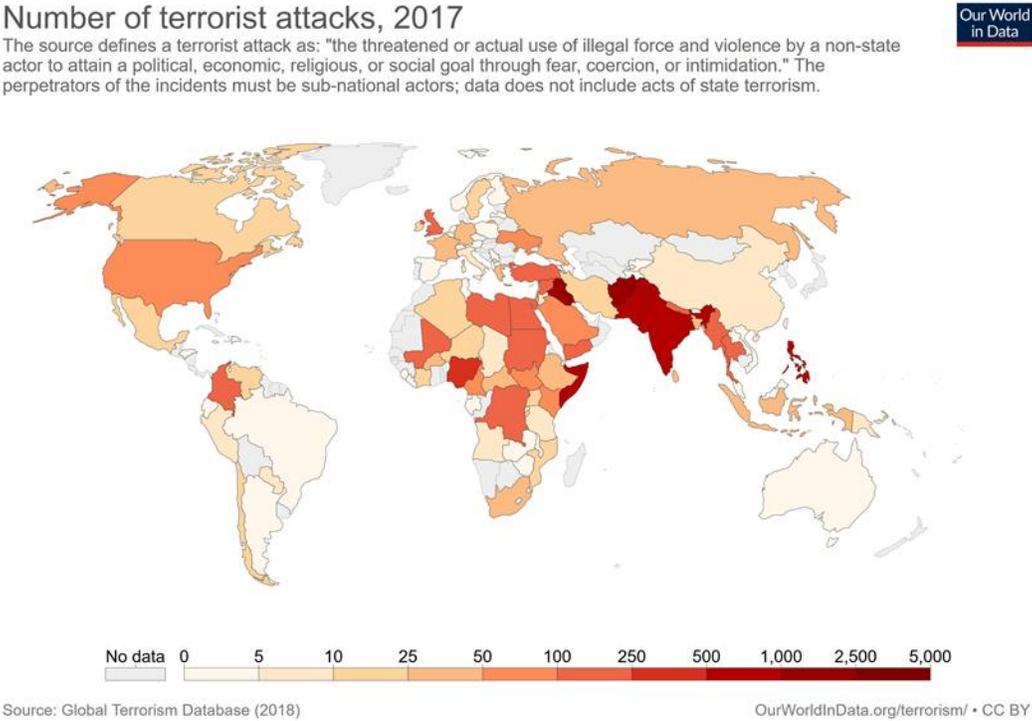


Figure 1.1 A visualization for the annual number of terrorist attacks globally (Roser et al., 2019)

1.2 Problem statement

An explosive charge causes a shock wave that strikes the structures with a very strong shock wave, which creates a high pressure over the normal atmospheric pressure called overpressure. This overpressure has a peak value, which happens in a very short duration. This sudden strong shock wave can cause different damage levels depending on the explosive weight and the distance between the charge and the target. Therefore, it is not feasible to design the structure elements elastically to be undamaged under the maximum value of the applied blast load. In addition, it is costly and time consuming to change the design of existing structures to strengthen their blast resistant capability. Besides, redesigning will lead to an increased size of the structural elements to be able to encounter these threats without being damaged. This solution is costly and not desired. Alternatively, it is better to attach proper blast resistant layers to the existing structure to enhance its blast resistant capability and prevents the main body of the structure from being damaged. These protective layers should be characterized by high strength, low weight, high energy dissipation, sustainability and economy.

Traditionally, protective layers are used as sacrificial systems, which needs to be replaced after each blast load (Mazek, 2014; Mazek and Mostafa, 2013; Nurick et al., 2009; Rashad, 2013; Vinson, 2001; Wahab and Mazek, 2016; Xia et al., 2016; Zhu, 2008). A sand layer is a common protective layer in civil engineering, where it is can be cheaply sourced and readily available. However, a sand layer still has many disadvantages, which includes:

- 1) High self-weight, which could add a considerable value of dead loads. This could make the design of the underground structure uneconomical.

- 2) Unable to withstand additional blast shots. After the blast wave impact, the sand will be compacted and the entire protective system will need to be replaced.
- 3) Self-compaction of solid particles and water drainage issues, which make it difficult and expensive to control the sand density (TM5-1300, 1990; UFC 3-340-02, 2008).

To alleviate such deficiencies, novel protective layers need to be developed. New blast protective layers should offer the following advantages: 1) add minimum load to the existing structure; 2) ability to withstand repetitive blast loads and; 3) ability to be repaired or replaced easily. The proposed protective system in this research is designed to withstand this hyperdynamic load in two ways:

- 1) Absorbing a portion of the applied energy in the form of kinetic energy and elastic internal energy and reflecting a portion of the shock wave in the opposite direction of the applied load.
- 2) Storing a portion of the applied energy in a form of internal energy expressed in strain, cracks, etc.

Based on these criteria, the proposed sandwich panel will be able to withstand successive blast loads and repaired efficiently.

By the early years of the twentieth century, concrete was used as a common material for the protective systems. Reinforced concrete (RC) structure has since become an excellent system for protecting structures against blast load due to its high strength, workability and affordability. This study offers a potentially new way of designing a protective system by using RC panel and helical springs. Based on the literature, helical springs have never been used as an interlayer of blast

resistant sandwich panels. However, helical springs are used as a shock absorber in the vehicles and trains industry. Some of the available truck helical springs are examined to be modeled as an interlayer in this research as it is more feasible than designing new helical springs with special specifications, which might decrease the availability of producing it in the local market and might increase its cost. These compression helical springs are selected to examine and evaluate their blast resistant capability when used as an interlayer of the newly proposed sandwich panel. One of the most important criteria for selecting such helical springs is its ability to store and reflect most of the applied high impact loads and accordingly, decrease the amount of the imparted loads to the protected structure. In addition, the cost of these helical springs is reasonable and they are commercially available due to the abundance of their production by the factory. Accordingly, RC panels and helical springs are used as the main protective layers of the newly proposed RC panel - Helical springs- RC panel (RHR) sandwich panel. RHR sandwich panel consists of two facing RC panels and a number of helical springs as an interlayer between them. The back RC panel is considered in this thesis as the roof of a shallow underground structure. The main role of the front RC panel and the helical springs interlayer is to prevent the back RC panel from being fully damaged under successive blast loads with different values. Consequently, it will protect the equipment and devices located inside the protected structure.

Another issue has occurred during this research. Due to the heterogeneity of concrete material, it is hard to simulate the proper behavior of concrete structures against blast loads. The nonlinear behavior of concrete structures can be modeled using mesoscale and macroscale modeling (Gebben and Ruppert, 2000; Govindjee S, Gregory JK, 1995; Hentz et al., 2004; Malvar et al., 1997). Mesoscale modeling is advanced but more sophisticated and time consuming than the

macroscale modeling. In the mesoscale modeling, the concrete material is assumed to be simulated by three phases, which are, the mortar matrix, the coarse aggregates and the interaction between the surface of the aggregate and the mortar matrix. Relatively, the macroscale model is simpler and computationally more efficient, but unable to accurately simulate the damage pattern and the crack trajectory of the concrete structure. The Riedel- Hiermaier-Thoma (RHT) model is one of the most well-known macroscale models, which used to simulate brittle materials like concrete (Riedel W, Thoma K, 1999; Riedel, 2009, 2000; Riedel et al., 2008). In the existing literature, a series of modified parameters of the RHT concrete models have been proposed to simulate the nonlinear response of different concrete structures under different load conditions (Codina et al., 2016; Hu et al., 2016; Nyström and Gylltoft, 2011a, 2009; Tu and Lu, 2010, 2009; Wang et al., 2013). The numerical results of these studies show that the default RHT model gives undesirable behavior under blast loads due to the unrealistic post softening behavior of the proposed stress strain curve and its overestimated residual strength. In general, all of the mentioned studies proposed modified RHT models, which were able to simulate their concrete structure performance for their studied application. However, the accuracy of the model significantly relies on the specimen dimensions, loading conditions, boundary and initial conditions. Therefore, these proposed RHT models are found to be not useful in simulating concrete behavior for different applications. Thus, it is crucial to examine and evaluate the previously proposed RHT models and find the proper parameters, which can accurately simulate the physical post failure behavior of concrete under free air blast loads.

In the literature, the Single Degree of Freedom (SDOF) models have been used extensively to predict the response of structures under dynamic loads. However, SDOF models cannot predict

the localized damage of a structural member (Li and Meng, 2002; Naito and Wheaton, 2006; Zhou et al., 2008). Besides, the protective systems are too complex to be analyzed using SDOF models. Accordingly, finite element analysis could be a feasible method to accurately examine the behavior of such protective systems. One of the main motivations for using the finite element analysis in this study is its ability to simulate the behavior of complex detailed structures such as helical springs, with reliable results, which cannot be achieved using simple analytical equations. Therefore, the new protective system is numerically simulated using AUTODYN program (ANSYS-AUTODYN, 2005), taking into consideration sensitivity to meshing and using proper boundary and initial conditions to simulate it as in the physical tests. In addition, the geometric nonlinearity (large deformation) and the material nonlinearity (plasticity, strain hardening, strain softening and failure) are considered. In this thesis, the developed numerical model is validated with available experimental tests to ensure the accuracy of the numerical results.

Based on the validated numerical model of the RHR sandwich panel, a comparative numerical study is then conducted between the blast resistant behavior of the traditional protective systems, namely SR protective system and RSR sandwich panel with that of the proposed RHR sandwich panel to evaluate their performance under different range of blast loads. Additionally, a parametric study is conducted to examine the effective parameters of the helical springs interlayer, which can control the behavior of the proposed RHR sandwich panel. Eventually, useful design guidelines are introduced to help blast resistant engineers to design this new lightweight protective layer.

1.3 Objectives and methodology

The main objectives of this dissertation are as follows:

1. Develop a novel protective layer, which can withstand additional blast loads and can be replaced or repaired efficiently.
2. Validate experimentally and numerically the performance of the newly proposed sandwich panel.
3. Compare the performance of the newly proposed sandwich panel with the traditional sand – RC (SR) protective system and RC – Sand – RC (RSR) sandwich panel.
4. Study numerically the design parameters of the newly proposed sandwich panel.

The methodology employed in addressing the objectives of this dissertation are described as follows:

1. Conduct a detailed literature review of the existing protective layers and identify the strength and weaknesses of the existing protective layers. Based on the detailed literature review, propose an innovative lightweight protective layer to withstand the free air blast loads.
2. Investigate experimentally the behavior of the newly proposed sandwich panel under different range of free air blast loads.
3. Develop advanced numerical models, including a new modified RHT concrete model, to simulate an accurate behavior of the proposed protective layer against different ranges of free air blast loads.
4. Compare the blast resistant behavior of the RHR sandwich panel with the traditional SR and RSR protective systems under different range of blast loads.
5. Conduct a detailed parametric study on the proposed RHR sandwich panel to investigate the influence of design parameters of the helical springs on the performance of the system.

1.4 Dissertation overview

This dissertation aims to address the objectives presented in the previous section and establish general design guidelines to help the blast engineers to design the newly proposed lightweight RHR sandwich panel. Accordingly, this thesis is organized as follows:

- Chapter 1 provides an introduction to the current research, including general background information, problem statement, research objective, methodology and overview of this thesis.
- Chapter 2 presents an overview of the nature of blast loads and the traditional protective systems for shallow underground structures and tunnels.
- Chapter 3 includes a detailed experimental investigation of the performance of the newly proposed RHR sandwich panels, with different numbers of helical springs located in the interlayer, under different range of blast loads.
- Chapter 4 focuses on developing a modified RHT concrete model in order to accurately simulate the physical behavior of a simply supported plain concrete panel subjected to free air blast load. A single concrete element model is examined at the material level by carrying out numerical tests under various loading conditions. The results are presented in the form of axial stress-strain curves for each load condition. Accordingly, modifications are proposed to the parameters, which effectively can enhance the strain softening behavior of the stress strain curve to yield the failure strain value to an accurate value when compared with the laboratory results. Consequently, at the component level, a numerical and experimental application is conducted on a simply supported plain concrete panel against

free air blast load to evaluate the proposed RHT model in predicting the damage level and the crack trajectory of the concrete panel. Besides, the same concrete panel is simulated using the previous modified RHT models to emphasize the fidelity of the newly proposed RHT model.

- Chapter 5 investigates the numerical performance of the newly developed RHR sandwich panel using different numbers of helical springs as an interlayer under different free air blast loads and compares its numerical results with the experimental observation. Accordingly, the developed finite element model is used to obtain the energy analysis results, which cannot be obtained from the experimental work.
- Chapter 6 compares the blast resistant behavior of SR and RSR protective systems with the RHR sandwich panel under different ranges of free air blast loads to benchmark their performance and costs.
- Chapter 7 presents a numerical parametric study by wire diameter and the number of helical springs located in the interlayer. The main target of this study is to investigate the influence of these parameters on the performance of the entire RHR sandwich panel under different ranges of blast loads. The results are presented in the form of charts that can help blast engineers to design the RHR sandwich panel under the considered range of blast loads.
- Chapter 8 presents the contributions, conclusions and the recommendation for future work.

Chapter 2: Background of the blast loads and common traditional protective systems for shallow underground structure

Chapter 2 presents an overview of the nature of blast loads and common traditional protective systems for shallow underground structures and tunnels. The common protective layers are named by Sand layer – RC panel (SR) protective layer and RC panel – Sand interlayer – RC panel (RSR) sandwich panel. The disadvantages of these protective layers are presented and a new blast resistant sandwich panel is proposed to overcome these shortcomings.

2.1 An overview of blast loading nature

An explosion is defined as a sudden release of a huge amount of energy in a very short time duration. This energy is generated from a quick chemical reaction in solids or gases where an expansion of matter occurs. This released energy changes the normal pressure and temperature of the surrounding air to a very high pressure value of about 3×10^7 Pa and a high temperature of about 3000°C (Yandzio and Gough, 1999). The blast wave is then propagated from the center of detonation to the surrounding air with a very high velocity (TM5-1300, 1990). For example, the detonation velocity of high explosives such as TNT is about 6930 m/s. The distance between the origin of the detonation point and the point, where the pressure time history is measured, is called standoff distance (SoD).

Figure 2.1 shows the typical blast pressure time history for an explosion at a certain point. As shown in the figure, the incident peak overpressure is reached instantly upon the arrival of the shock wave at that point. This peak overpressure is then decayed until being below the ambient

pressure and finally returned to the ambient pressure value. The duration of the blast time history is divided into three intervals. The first duration is the arrival duration where the shock wave starts to travel from the origin of the detonation and arrives at a certain point. The second duration is between the arrival time and the time where the pressure decays until having the ambient pressure value. This duration describes the positive pressure phase. The third duration describes the negative pressure phase where the blast pressure changes from the ambient pressure to a peak negative pressure then diminishes again to the ambient pressure. In most analytical methods, the effect of the negative pressure phase is ignored because it usually has little effect on the maximum response, so it is commonly omitted in design and analysis. For further simplification, an equivalent triangular load for the positive phase is considered (TM5-1300, 1990).

Figure 2.1 shows a schematic representation of the relationship between the amplitude and the frequency of different structural loads. These relationships illustrate the different nature of blast loading when compared with other kinds of structural loads. It is essential to understand this relationship as it governs the design approach of any structure under any hazard (TM5-1300, 1990). It is noted that blast loads have the highest amplitude with different ranges of frequency among the other structural loads. This can be explained as when the blast weight is located near a structure; a highly impulsive and high intensity pressure load occurs over a localized area of the structure. whereas, when the blast charge is located far away from the structure, a lower intensity with a longer duration uniform pressure distribution imposes over the entire structure (Ngo et al., 2007; TM5-1300, 1990). Figure 2.2 shows a schematic relationship between the pressure value and the distance from the detonation point.

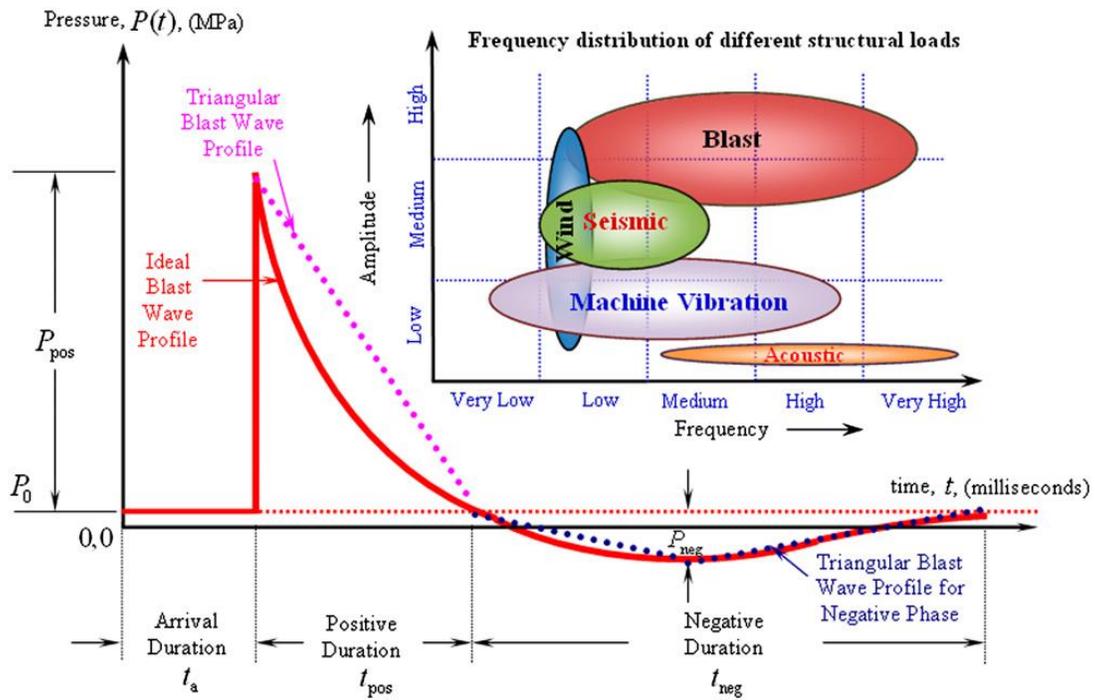


Figure 2.1 Typical blast pressure time history and amplitude frequency relationship of different structural loadings (Goel and Matsagar, 2014)

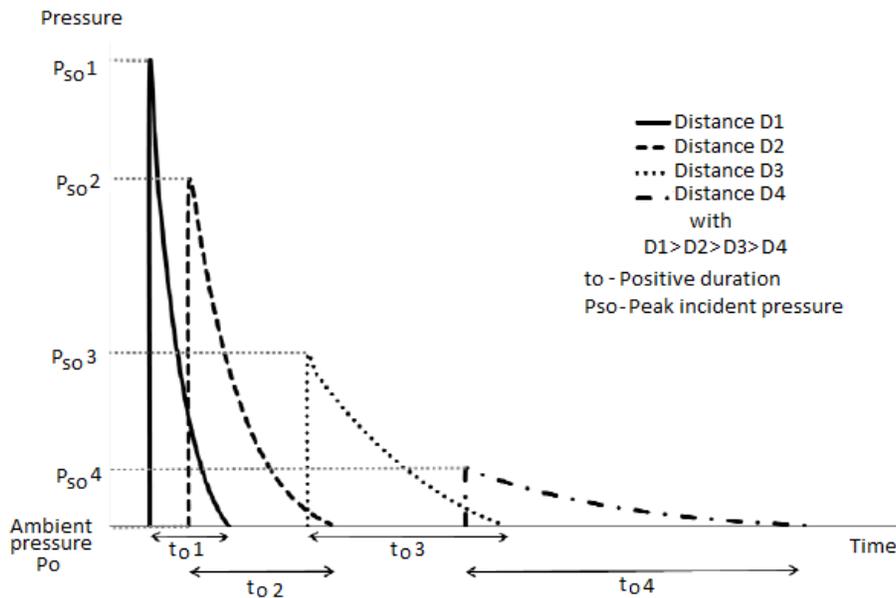


Figure 2.2 Relationship between the positive pressure phase and the standoff distance (Karlos and Solomon, 2013)

2.1.1 Explosion materials and Trinitrotoluene (TNT) Equivalent

Due to the variety of explosives and their different characteristics, TNT was selected as a standard for assessing the detonation characteristics of all other explosives. Accordingly, any explosion material is expressed in terms of standard TNT equivalent mass for the purpose of design (Yandzio and Gough, 1999). The weight of the equivalent TNT needed to produce the same effect of a given explosive can be expressed as illustrated in equation 2.1.

$$TNT \text{ Equivalence} = \frac{W_E}{W_{EXP}} = \frac{H_{EXP}^d}{H_{TNT}^d} \quad (2.1)$$

Where W_E is the effective charge mass or TNT equivalent mass (kg); W_{EXP} is the mass of explosive (kg); H_{EXP}^d is the heat of explosion (J/kg); and H_{TNT}^d is the heat of the explosion of TNT (J/kg).

2.1.2 Types of blast loading

There are two types of blast loads: confined blast load, which occurs inside a structure and unconfined blast loads, which occurs outside a structure. Besides, blast charges can be located on the structure surface (contact blast loading) or can be located at a certain distance from the structure (non-contact blast loading). The unconfined blast loading is divided into three types: 1) free air blast load, 2) air blast load and 3) surface blast load. In this thesis, the unconfined, free air blast loading is considered, as shown in Figure 2.3, where the structure is subjected to blast load in an open area without being affected by any reflection waves induced from the ground or any adjacent structure. This can be controlled by placing the target structure above the ground by enough distance, which allows the blast wave to hit the target structure before any reflection occurs.

Accordingly, an accurate analysis can be conducted to investigate the effect of the free air blast load on the target structure.

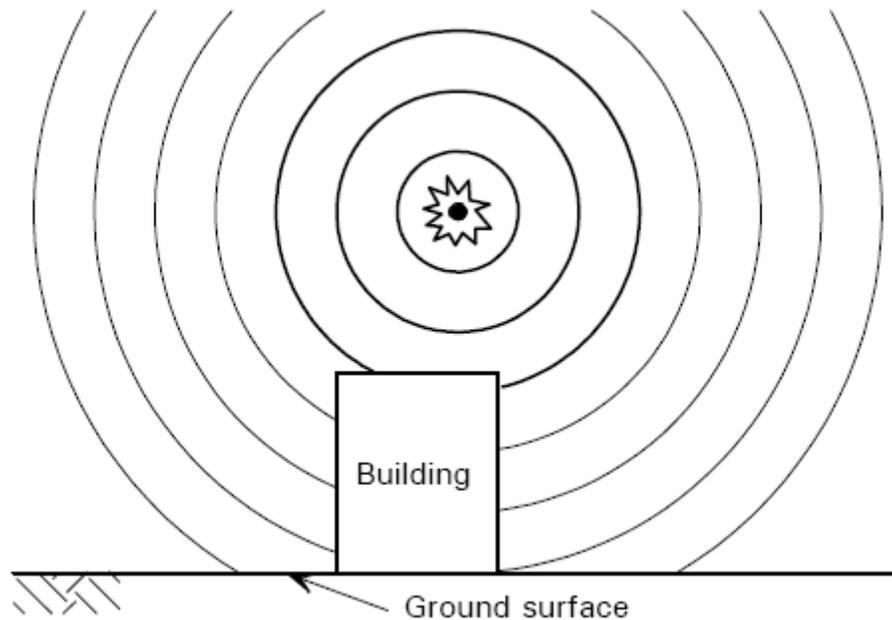


Figure 2.3 Unconfined non-contact blast loading categorization (Yandzio and Gough, 1999)

2.1.3 Scaled distance law

There are many parameters, which can characterize blast loads. These parameters mainly depend on the blast weight and the standoff distance. These two parameters are used by Hopkinson (1915) to formulate a relationship named Hopkinson-Cranz scaling law. This law is then widely used to simply characterize any blast load. The output of this scaling law is the scaled distance, which is considered in the blast design as an important characterization for the blast load and it is commonly calculated as expressed in equation 2.2 (Baker, 1973). The concept of the scaling law is that different blast weights with different standoff distances having equal scaled distance produce an

equally blast load. The blast parameters of the positive phase of the shock wave can be obtained by the scaled distance using the following chart shown in Figure 2.4.

$$Z = \frac{R}{\sqrt[3]{W}} \quad (2.2)$$

Where Z is the dimensional scaled distance (m/Kg^{1/3}), R is the standoff distance (SoD) in meters (m) and W is the blast weight in kilograms (kg) of TNT.

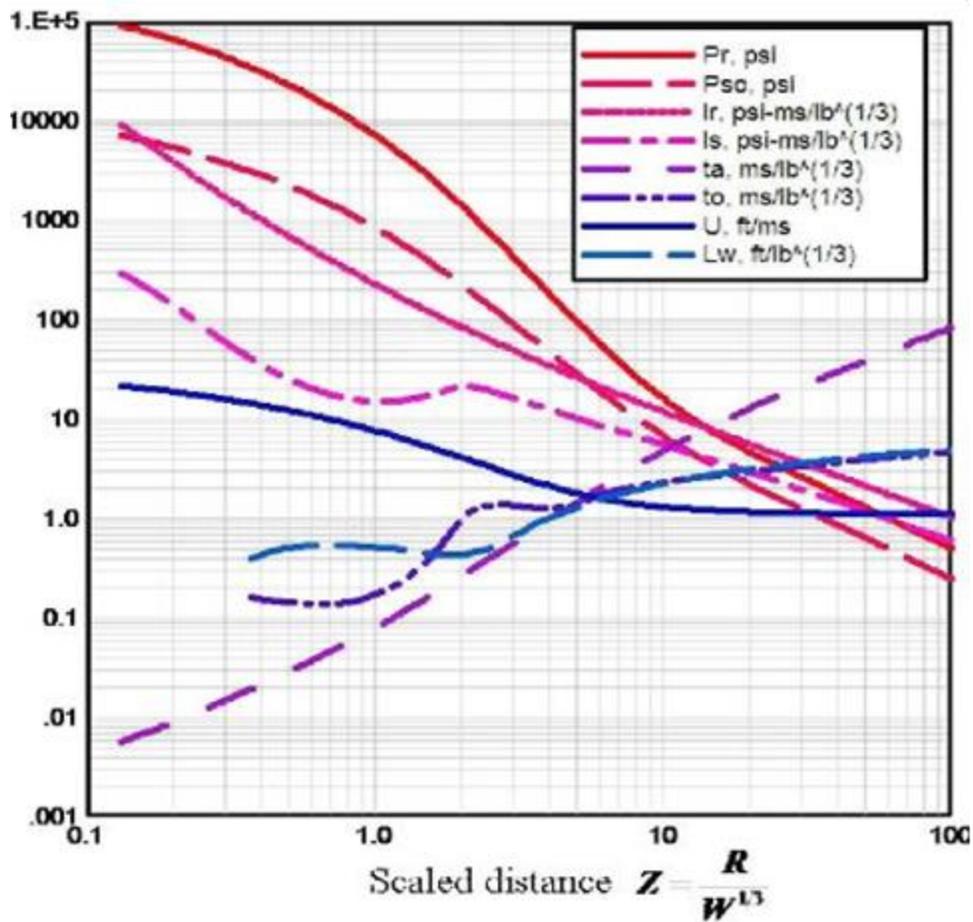


Figure 2.4 Positive phase shock wave parameters for a spherical TNT explosion in free air at the sea level

(TM5-1300, 1990)

2.2 An overview of SR and RSR protective systems

Shallow underground structures and tunnels are some of the most critical infrastructures for military operations such as weapons and ammunition stores. Once the underground structure is damaged by blast shot, it is time-consuming and expensive to repair.

In this thesis, the behavior of two commonly used protective systems is studied and evaluated. The first protective system consists of a single sand layer that is used to protect a RC panel (the structure to be protected) from blast shots. This protective system is named SR protective system. The other protective system consists of a front RC panel and sand interlayer, which is used to protect a back RC, panel (the structure to be protected). This protective system is named by the RSR sandwich panel. Both protective systems are used to protect the same RC panel. Both protective systems rely on the sand behavior in attenuating the applied blast load. Accordingly, the behavior of the sand layer is studied and evaluated.

2.2.1 Background of the Sand layer

Historically, a sand layer was used as a protective barrier or a mitigation layer/interlayer to protect underground structures against blast loads (Matsagar, 2016; TM5-1300, 1990; UFC 3-340-02, 2008; Wu et al., 2004). This practice was attributed to its availability and its economic cost. However, a sand layer is usually very heavy and not efficient in taking additional blast loads due to its plastic behavior (Cheeseman et al., 2006; Fiserova, 2006). Besides, RSR was commonly used as a blast resistant wall/barrier between two large quantities of explosives. It was usually designed as a sacrificial system when an explosion occurs (UFC 3-340-02, 2008). The mechanism of the RSR to encounter blast loads relies on the strength and the ductility of the RC panel and the blast

attenuating ability of the sand layer. Figure 2.5 shows a schematic representation of the commonly used blast resistant RSR wall.

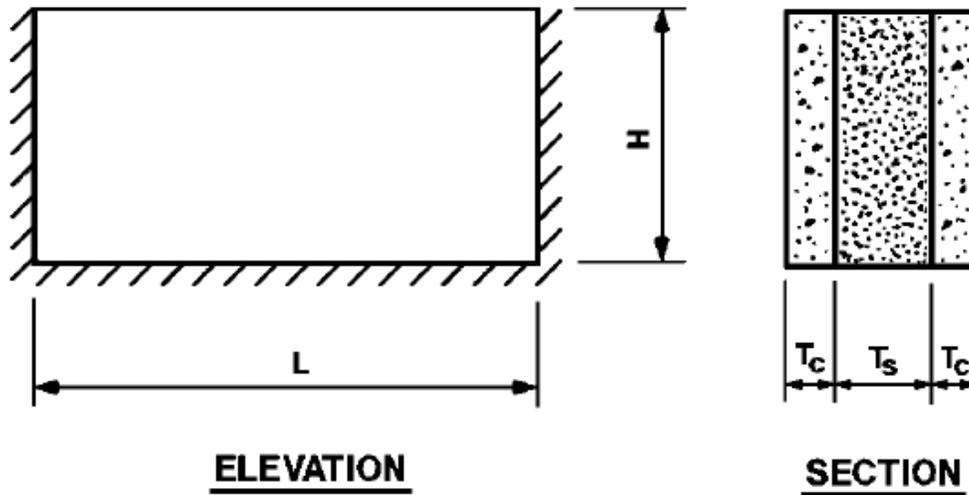


Figure 2.5 Schematic representation of the RSR wall (UFC 3-340-02, 2008)

The plastic behavior of the sand layer characterized by performing plastic compaction between the solid particles of the sand layer. This compaction depends mainly on the existence of the air pores between the sand particles (Cheeseman et al., 2006; Fiserova, 2006; Pickering et al., 2012). The existence of moisture/water in the pores decreases the amount of internal energy absorbed by sand as water will prevent the compression process and will be trapped in the pores (TM5-1300, 1990; UFC 3-340-02, 2008; Wu et al., 2004).

In general, sand is considered as a porous granular material and it consists of small solid mineral particles in contact, which leads to the formation of pores. These pores are filled with air or water, which is controlled by the saturation level of the sand layer. In this study, dry sand is assumed, which means that the spaces between its particles are filled with air and accordingly allow sand to

absorb more energy when compared with the partially and fully saturated sand layers. In the literature, it was found that the dynamic behavior of the dry sand is not rate dependent, but rather dominated by plastic densification processes (Bergeron et al., 1998; Fairlie and Bergeron, 2002; Henrych, 1979; Loret and Khalili, 2000). At high pressures, the air is firmly enclosed by the dry sand pores and the deformation mechanism is dominated by the deformation and the volume fraction of the constituent materials (i.e., solid mineral particles and air) (Cheeseman et al., 2006). Figure 2.6 shows the relationship between the dry sand density and the pressure. It is noted that sand has poor elastic behavior and tends to behave in the form of plastic compaction especially when subjected to high pressure.

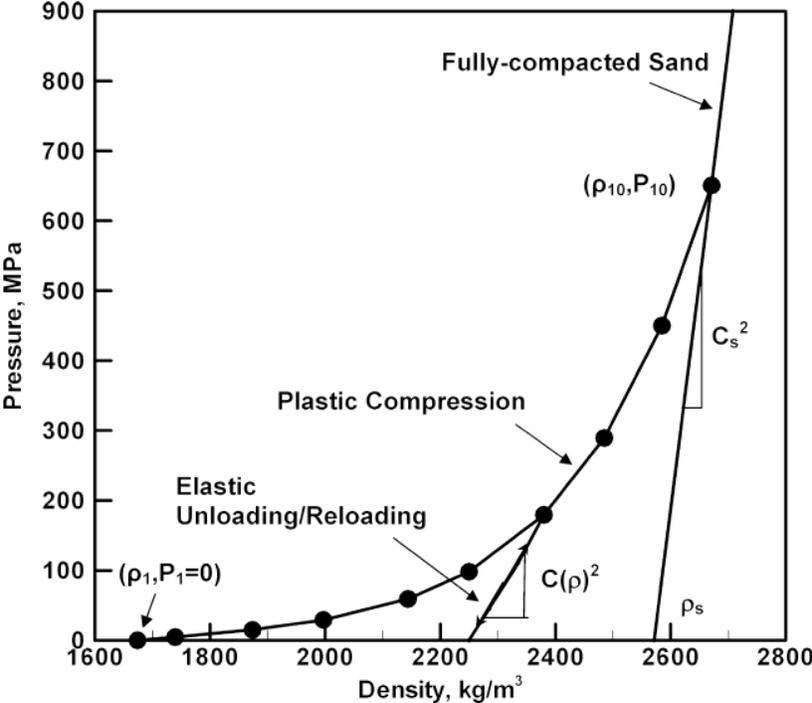


Figure 2.6 Relationship between the density and pressure for the dry sand (ANSYS-AUTODYN, 2005)

2.3 The proposed RHR sandwich panel

To overcome the shortcoming of the sand layer, mentioned in the previous section, and improve the blast resistant performance of underground structures, lightweight and high strength blast protective layers should be used. These lightweight blast protective layers should offer significant advantages: 1) High stiffness to weight ratio; 2) can withstand additive blast loads and 3) can be replaced or repaired easily; 4) High energy dissipation. In this thesis, a newly proposed sandwich panel is presented to replace the traditional SR and RSR protective system. This proposed RHR sandwich panel consists of front RC panel and helical springs interlayer that are used together to protect the back RC panel, which is considered in this study as the main structure. RHR sandwich panel mainly relies on the behavior of the helical springs interlayer, which consists of a number of helical springs. In general, it is noted that the RHR sandwich panel is lighter than the traditional SR and RSR protective systems.

2.3.1 Background of the helical springs

Helical springs were invented early in the 15th century. In 1676, Robert Hooke discovered the principle behind springs' action, i.e. when a spring is compressed or extended, the force it performs is directly proportional to its change in length (Hooke *et al.*, 1678). The stiffness or spring constant of a spring is the change in the force, divided by the change in displacement and its unit is N/mm. A helical spring is a mechanical device that can store and release energy. It is commonly used to absorb/attenuate impacts or shocks. Helical spring is commonly manufactured in a cylindrical shape, which consists of several successive coils. These helical springs are usually formed around steel jigs while the wire is still annealed or soft, then tempered or hardened to produce the resilient, resistive qualities of the finished spring and to give the spring its compression characteristics.

In the shock isolation systems design, the main task of the isolator device is to reduce the amount of the applied load imparted from structure to a shock sensitive element or equipment. The shock isolation system consists of an isolated component, isolator device and main structure. The fundamental feature of the isolator is to support the isolated component and reduce the static and/or dynamic load imparted from the main structure, as shown in Figure 2.7. Besides, the isolator should not allow any shock loads to be imparted to the isolated component and it should have an elastic force displacement relationship in order to restore its equilibrium position after the dynamic load has been applied. Besides, isolators should have long service, high reliability, low maintenance and economical cost. Most of these features are possessed by the helical springs. Accordingly, in the literature, helical springs are used as shock isolator devices especially for supporting large masses. For Instance, helical springs are used as a shock isolator device to protect shock sensitive equipment from the induced structure motion. Figure 2.7 shows a shock isolation system using helical springs. Figure 2.8 shows different types of compression helical spring mounts.

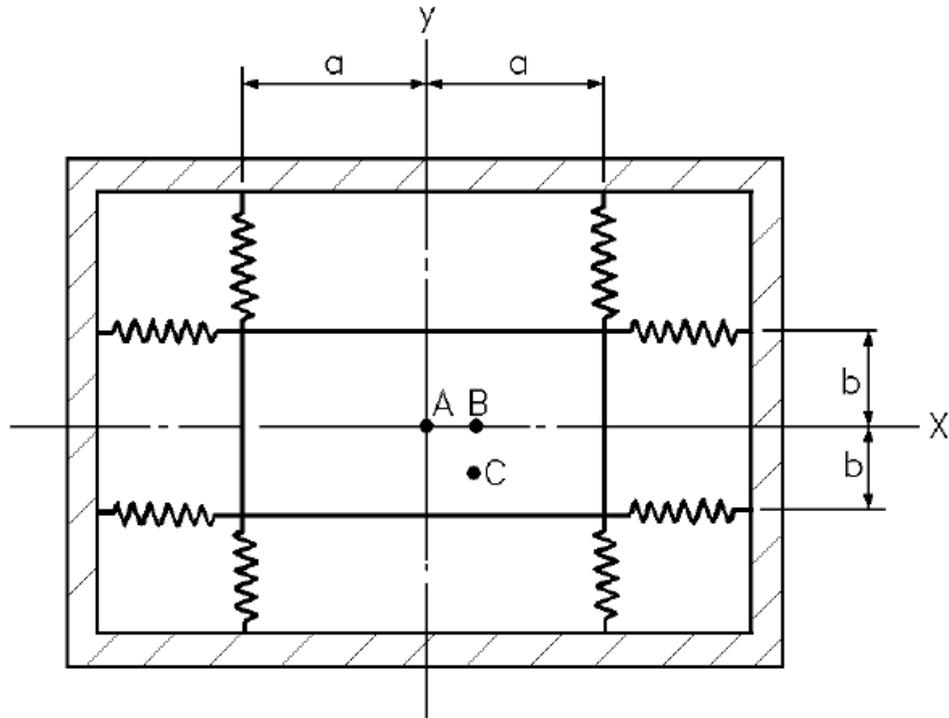


Figure 2.7 Schematic representation of a shock isolation system using helical springs (TM5-1300, 1990)

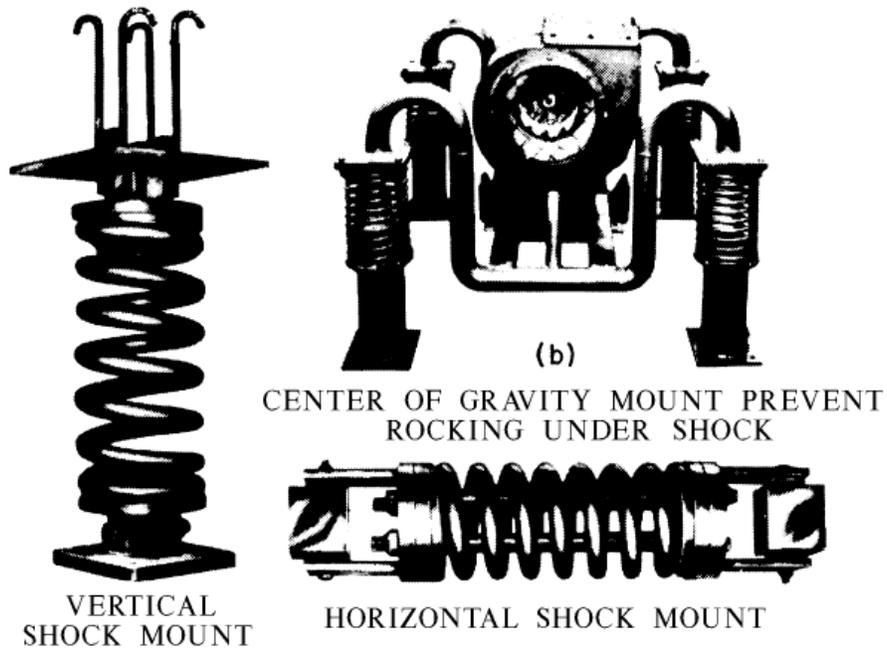


Figure 2.8 Compression helical spring mounts (TM5-1300, 1990)

Typically, structural vibration can be eliminated using viscous damper. However, a viscous damper is not effective in the high blast loads where the load is very fast compared to the natural frequency of the structure. In this study, the compression helical springs are used with their natural inherent damping characteristics and self-restoring ability to diminish the applied blast load.

One of the most important considerations in designing helical springs as a shock isolator is the ability to find such helical springs with the desired specification in the market. These specifications may include many parameters such as maximum dynamic displacement, maximum height, maximum diameter and factors of safety such as allowable stress. By increasing the number of design parameters, the availability of springs in the market decreases and their cost increases. Accordingly, due to the various number of parameters, which can control the behavior of the helical springs, the desired specifications are adapted to match that of the available helical springs, which easily can be found in the market. Besides, to limit the scope of the parametric study applied on the behavior of the helical springs, only certain parameters are selected which mainly changes the total stiffness of the helical springs interlayer such as wire diameter, which is obtained from the manufacturer's data, and the number of helical springs.

Based on the literature, helical springs have never been used as an interlayer of protective sandwich panels against blast loads. However, helical springs were used as a shock isolator and vibration absorber for shock sensitive equipment under static and dynamic loads, as mentioned above. In this study, compression helical spring is proposed to be the interlayer of the proposed RHR sandwich panel. All the helical springs are designed to absorb the applied blast loads without

reaching its closed length, which may lead to inelastic action and permanent damage in the spring body and accordingly, transmit additional loads to the back panel. The closed length of compression helical spring means that the helical spring reached its maximum compressive displacement in which all its coils touch each other. Consequently, helical spring will act as a solid body and plastic deformation may occur. Whereas, the free length of helical spring is the unloaded length, where there is no load applied. Figure 2.9(b and c) shows the free length and closed length of the helical spring.



a) Helical springs after being coated with anti-corrosion material



b) Free length of helical spring



c) Closed length of helical spring

Figure 2.9 Helical springs

These helical springs are manufactured using round carbon steel wire grade D, according to DIN 17223, which is a standard designation of steel spring wires. The main mechanical property of

helical spring is its stiffness (i.e. spring rate), which is an indication of its capacity to absorb energy. Spring stiffness depends on the type of wire material, mean coil diameter; wire diameter and its active length as illustrated in equation 2.3 (Shimozaki, 1997; Wahl, 1963). Maximum shear stress τ_{max} can be expressed as shown in equation 2.4. After manufacturing the helical springs, the helical springs are coated with anti-corrosion material, as shown in Figure 2.9(a). Finally, a compression test is carried out for each helical spring to ensure its physical stiffness and its closed length.

$$K = \frac{F}{\Delta} = \frac{d^4 G}{8D^3 N} \quad (2.3)$$

Where: K is the spring stiffness; F is the applied force; Δ is the deflection; d is the wire diameter; G is the shear modulus of elasticity; D is the mean coil diameter and N is the number of the active coils.

$$\tau_{max} = K_W \frac{8pD}{\pi d^3} \quad (2.4)$$

Where: K_W is the Wahl factor which is the curvature correction factor and can be expressed as shown in equation 2.5 (Wahl, 1963).

$$K_W = \frac{4C - 1}{4C - 4} + \frac{0.615}{C} \quad (2.5)$$

Where: C is the spring index and equal to D/d .

2.4 Summary

In this Chapter, a background of the nature of blast loads and its different characteristics is presented. In addition, a background of the traditional SR and RSR protective layers and its usage in the blast resistance field is presented. The advantages and disadvantages of using SR and RSR are illustrated. In addition, a literature review on the usage of the helical springs is provided. Lastly, the motivation for using helical springs as an interlayer instead of the sand layer is stated.

Chapter 3: Experimental investigation of the performance of the RHR under free air blast load

It is difficult to recreate the realistic impact of the free air explosion process, including the fireball and the thermal effect without doing a blast field test. In this Chapter, field tests are carried out to understand the response and the failure shape of the newly RHR sandwich panel against different levels of free air blast loads. There are many parameters, which control the behavior of the RHR sandwich panel under blast loads as mentioned in Chapter 2. To limit the scope of this Chapter, the behavior of the RHR sandwich panel is experimentally investigated by changing the stiffness of the helical springs interlayer and changing the free air blast loads. In this fieldwork, the helical springs interlayer is changed by changing the number of helical springs. Besides, the free air blast load is changed by changing the scaled distance. The variation of pressure with time at different locations and the maximum displacement of the front RC panel are monitored and analyzed.

3.1 Specimens Preparation

Nine different experimental tests are carried out. The first experimental test is a free air blast test, which is conducted to verify the pressure sensor. A 1 Kg spherical charge of TNT is detonated in the free air and a pressure sensor is fixed at a standoff distance (SoD) of 1 m from the blast charge to measure the incident pressure time history.

The second test is applied to evaluate the default concrete model and accordingly, calibrate the effective parameters of the finite element model to better simulate the physical behavior of a concrete panel. For this test, a plain (unreinforced) concrete (PC) panel is simply supported on a

test rig. This PC panel is subjected to free air blast load generated from a blast charge of 4 kg TNT hanged above the center of the PC panel at a standoff distance of 1 m. The dimension of the PC panel is 1 m x 1 m and its thickness is 20 cm. The damage pattern and the crack trajectory are observed and later evaluated when compared with its corresponding numerical results obtained from using the default, previously modified and proposed concrete material models.

The third, fourth and the fifth field tests are conducted to evaluate the blast resistant capacity of the proposed (RHR-7) sandwich panel with seven helical springs located in the interlayer under a different range of blast loads generated from detonating 1, 5 and 10 Kg TNT at a SoD of 1 m which can be expressed as scaled distance of 1, 0.58 and 0.46 m/Kg^{1/3}, respectively. The dimension of the RC panels is 1 m x 1 m with a thickness of 10 cm.

The sixth test is conducted to evaluate the blast resistant capacity of the proposed (RHR-9) sandwich panel with nine helical springs located in the interlayer under a different blast load, generated from detonating 7.5 Kg TNT at a SoD of 1 m which can be expressed as a scaled distance of 0.51 m/Kg^{1/3}. The dimension of the RC panels is 1 m x 1 m with a thickness of 10 cm.

The seventh, eighth and ninth tests are conducted to test the blast resistant capacity of the proposed (RHR-16) sandwich panel with sixteen helical springs located in the interlayer under a different scaled distance of 1, 0.58 and 0.46 m/Kg^{1/3}. Table 3.1 shows the test matrix for this experimental work. The dimension of the RC panels is 1 m x 1 m with a thickness of 10 cm.

Table 3.1 The blast field test matrix

No.	Specimen name	Number of helical springs	Blast weight (Kg TNT)	Standoff distance (m)	Scaled distance (m/Kg^{1/3})
1	Free air blast test	---	1	1	1
2	Plain concrete panel	---	4		0.63
3	RHR-7	7	1		1
4			5		0.58
5			10		0.46
6	RHR-9	9	7.5		0.51
7	RHR-16	16	1		1
8			5		0.58
9			10		0.46

Table 3.2 shows the mechanical properties of the helical springs used in the experimental field tests. Note that the spring index is the relationship between the mean coil diameter and the spring wire diameter. All the helical springs located at the interlayer are identical and have the same specification.

Table 3.2 The Specifications of helical springs used in the blast field tests

Type of spring	Compression
Free spring length	250 mm
Closed spring length	125 mm
Wire diameter	20 mm
Pitch of spring	46.3 mm
Outside spring diameter	150 mm
Mean spring diameter	130 mm
Inside spring diameter	110 mm
Spring index	6.50 ul (unitless)
Spring weight	6.67 Kg

Six reinforced concrete formworks are prepared, as shown in Figure 3.1. The reinforcement of the RC panels is the same. Single mesh (5Ø8/m) is added to each formwork. This minimum reinforcement prevents excessive cracking and deflection under self-weight. In addition, this reinforcement prevents brittle failure under blast loads (UFC 3-340-02, 2008). The clear dimension of each formwork is 1 m by 1 m with 10 cm depth. U-bolts are implemented in the formworks, as shown in Figure 3.1, in order to be used as connectors between the facing RC panels and the seats of the helical springs. The advantage of clamping the helical spring's seats with the RC panels is to increase the force required to buckle the helical spring. Four, three and two U-bolts are used for each interior helical spring, edges helical spring and corner helical spring, respectively. All formworks are then poured with concrete and left for 28 days to take its compressive strength. It

is found that the average value of the compressive strength calculated from testing the standard cubes of concrete mortar is 353 Kg/cm^2 (35 MPa).

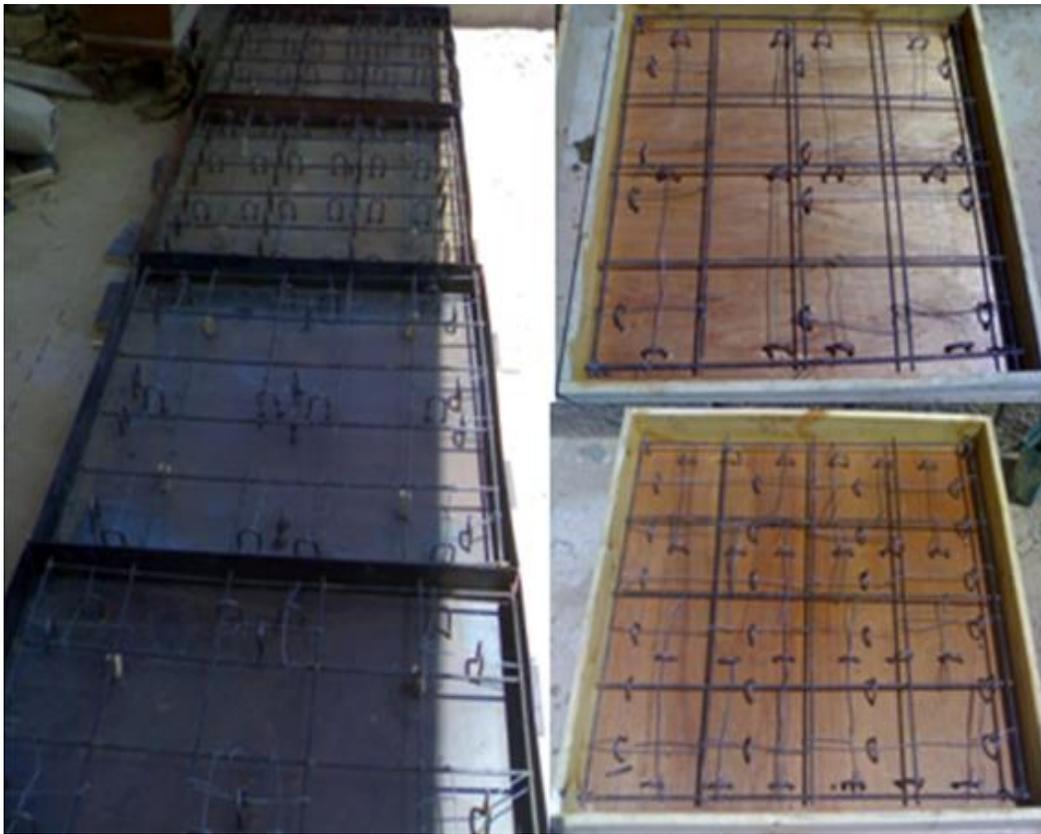
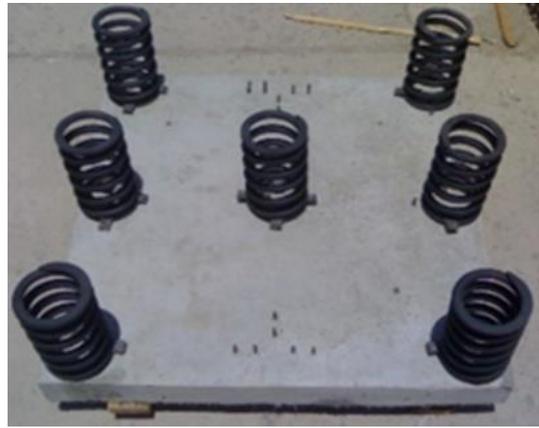


Figure 3.1 Reinforced concrete formworks

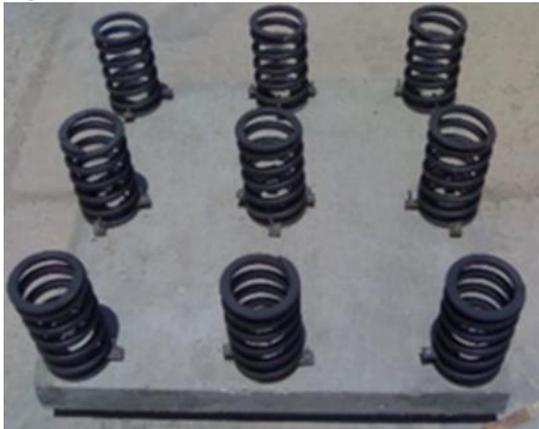
Each two RC panels are then connected by different numbers of helical springs to form the three RHR sandwich panels. The only difference between these RHR sandwich panels is the number and the locations of helical springs in the interlayer. The numbers of helical springs used for the three specimens are 7, 9, and 16 helical springs. Figure 3.2 shows the configurations and the arrangement of the helical springs of the three RHR sandwich panel named RHR-7 using seven helical springs, RHR-9 using nine helical springs and RHR-16 using sixteen helical springs.



RHR-7 (7 helical springs)



RHR-9 (9 helical springs)



RHR-16 (16 helical springs)



Figure 3.2 Configurations of the three RHR sandwich panels and the location of the helical springs in each interlayer

3.2 Test setup

A field test rig is manufactured specially to support the tested sandwich panel in which the back reinforced concrete (RC) panel is simply supported at its four edges, as shown in Figure 3.3. The test rig is designed to withstand the studied range of the blast loads without being damaged. The dimension of the field test rig is 1 m x 1 m and its height from the ground is 0.3 m to avoid the effect of the reflected waves induced from the ground. The RHR sandwich panels are subjected to different blast charges at a standoff distance (SoD) of 1 m above the center of the front RC panel of each specimen. Figure 3.3 shows the test setup of the RHR-7 sandwich panel under a blast load of 1 Kg TNT at a SoD of 1 m.

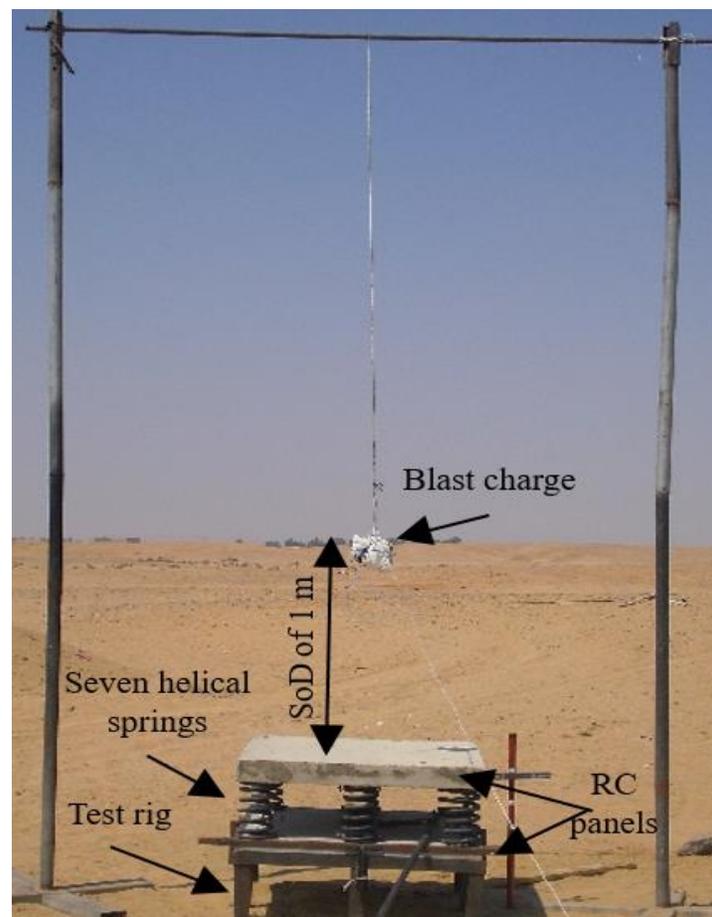


Figure 3.3 Test setup of the RHR-7 under 1 Kg TNT at SoD of 1 m

In this field test, Piezotronics pressure smart sensors PicoCoulomB (PCB) are used to receive the incident pressure resulting from any blast shot, as shown in Figure 3.4. This pressure sensor is inserted into a steel unit, which mainly fabricated to protect it from explosion effects. Besides, steel tubes are used to protect the pressure sensor cables from being damaged. The working methodology of this instrument is that the pressure sensor receives the applied pressure, resulting from an explosion, as voltage signals. After that, these signals are amplified and then transferred to a data acquisition system to read and analyze the pressure time history. Finally, the pressure time history is calibrated by individual calibration sheets, as shown in Figure 3.6, to convert it from voltage reading to pressure time history. Figure 3.5 shows the amplifier, which is used to enlarge the volt signals received from the pressure sensor to the transducer (PCD-320A). This transducer is a voltage-measuring instrument, which is used to receive the amplified voltage signals induced by the blast loads.

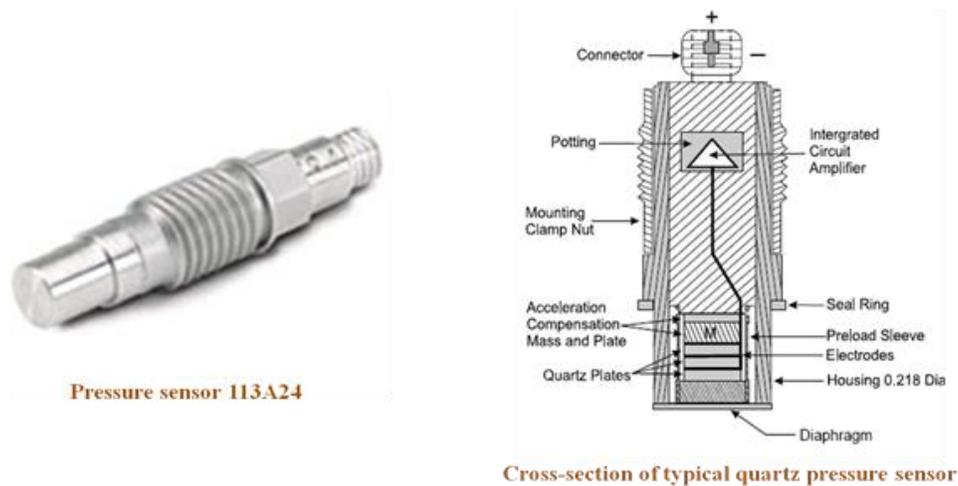
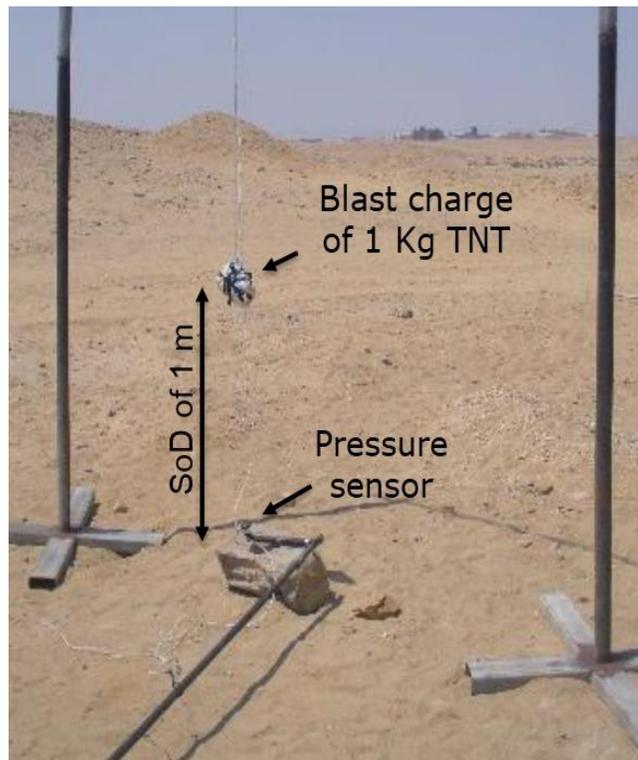


Figure 3.4 Piezotronics (PCB) pressure smart sensor

Kg TNT is detonated in free air and the pressure time history is measured by using pressure sensor located at a SoD of 1 m from the blast charge, as shown in Figure 3.7. After verifying the blast load, the PC panel is located on the test rig to be tested under a free air blast load. Figure 3.8 shows the test setup of the PC panel test. Consequently, the three RHR specimens are tested under different scaled distance. The blast charges are hanged over the center of the front RC panel of the tested RHR sandwich panel at a standoff distance of 1 m, as shown in Figure 3.8.



**Figure 3.7 Experimental test setup of the free air explosion test of 1Kg TNT
at a SoD of 1 m**

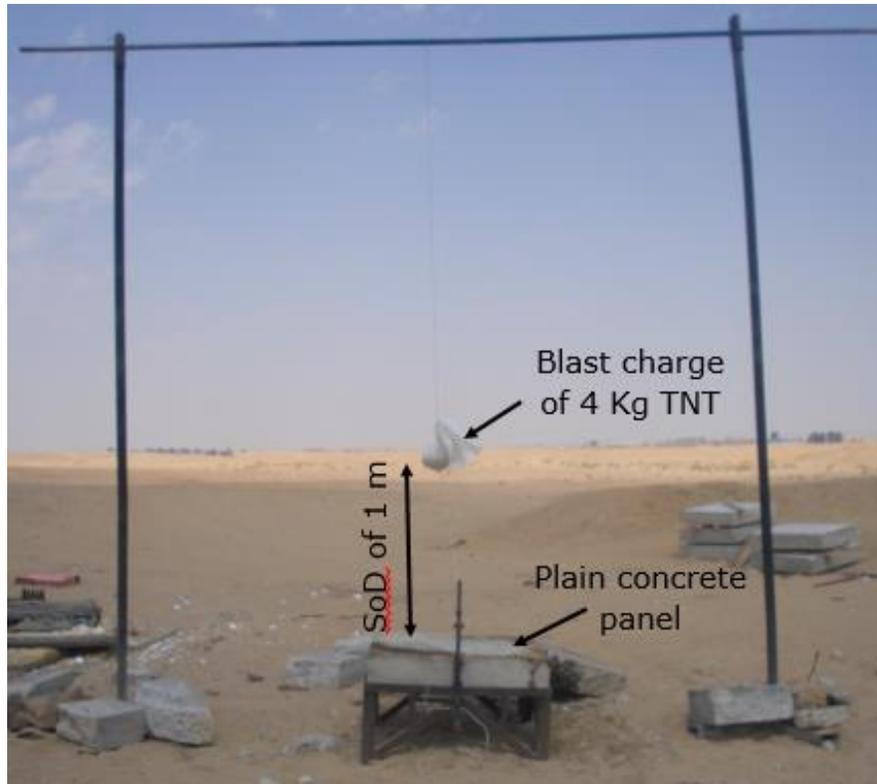


Figure 3.8 Testing set up of PC panel test

3.4 Discussion and results

3.4.1 Free air detonation of 1 Kg TNT

After detonating the free air blast charge, the recorded pressure time history is compared with the CONWEP program (CONWEP, 1990). CONWEP is a simple program in which the effect of conventional weapons can be represented by using equations and curves, which based on a stream of experimental data done by the U.S. Army. Figures 3.9(a and b) shows the voltage-time history recorded from the field and the pressure time history obtained from the CONWEP program. The result shows that the pressure-time history obtained from the CONWEP program agrees well with that recorded in the field blast tests. The maximum voltage value obtained from the recorded voltage time history is 3.3 Volts, which is equivalent to 9.65 bars after using the calibration sheet,

shown in Figure 3.6. The difference between the peak overpressure recorded in the field and that obtained from the CONWEP program is 3 %, which is accepted.

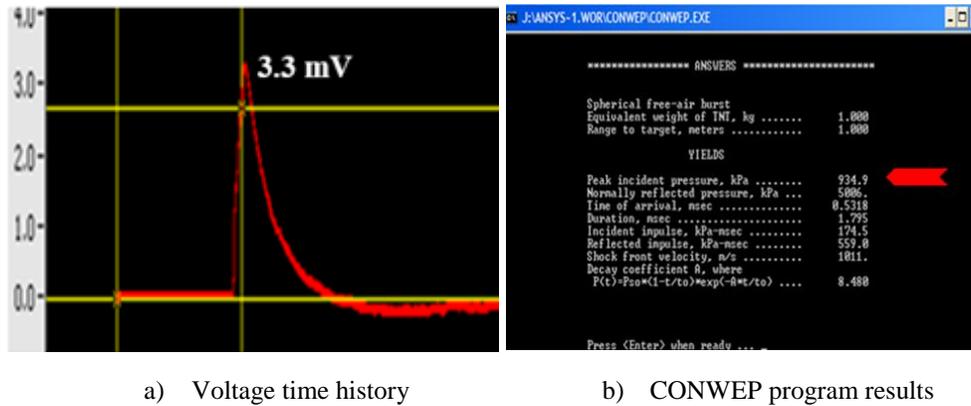


Figure 3.9 Field reading and the CONWEP results of detonating of 1 Kg TNT at a SoD of 1 m

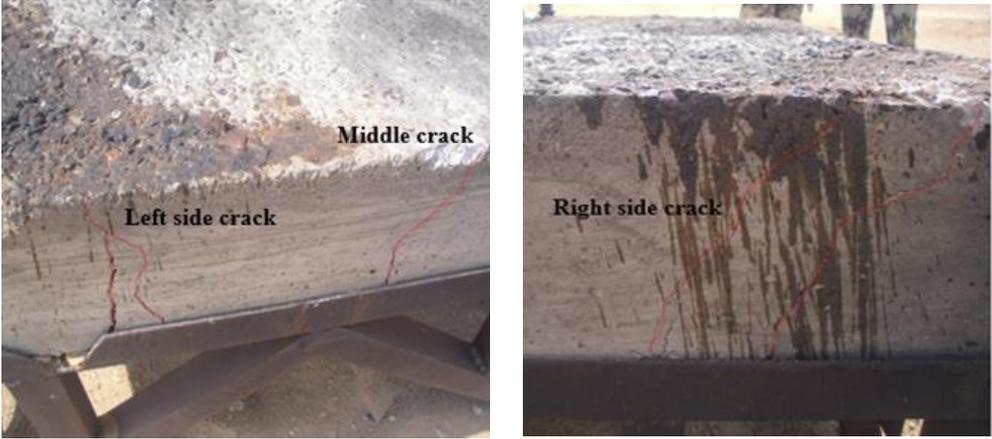
3.4.2 Free blast test of the plain concrete panel

After verifying the pressure measuring instruments, a free air blast test is applied on a simply supported plain concrete panel. The incident peak overpressure of detonating 4 Kg TNT is recorded by a pressure sensor located in the free air at a distance of 1 m from the blast charge. The recorded peak overpressure value is 24.52 bars. The damage pattern and the crack trajectory are observed. Figure 3.10 shows the crack trajectories that occurred on the front, back face and sides of the PC panel. It is observed that the PC panel is totally damaged and cracks occurred on the front face, sides and back face. However, the PC panel still coherent without being fragmented into pieces. For the front face (i.e., compression side), the main crack occurs through the entire length of the PC panel, as shown in Figure 3.10(a). Three cracks are observed through the depth of the PC panel, as shown in figure 3.10(b). One crack in the middle and one crack at each side. As for the back face of the PC panel, diagonal cracks with wide opening are observed. The damage

pattern that occurred on the back face is more than that observed on the front face due to the weakness of concrete in tension.



a) Front face and side cracks



b) Side cracks



c) Back face cracks

Figure 3.10 Damage pattern of the PC panel after the explosion process

3.4.3 Free blast tests on the RHR sandwich panel

In this section, the performance of the RHR sandwich panels with different interlayer stiffness is investigated under different scaled distance. In general, the recorded peak overpressure values of the incident pressure, generated from detonating 1, 5, 7.5 and 10 Kg TNT at a SoD of 1 m, are 9.7, 27.1, 35.3 and 39.6 bars.

3.4.3.1 RHR-7

In this section, the RHR sandwich panel with seven helical springs in the interlayer, named RHR-7, is subjected to three blast loads of 1Kg, 5 Kg and 10 Kg TNT at a SoD of 1 m. For 1 Kg TNT, it is observed that there are no cracks on the front and back RC panels. Figure 3.11 shows images of the RHR-7 specimen during the explosion process recorded by a high-speed camera, which can capture 20,000 frames/sec. The spreading of the fireball, the front shock wave (compressed air

layer) and its reflection with the specimen surface and the ground surface are observed, as shown in Figure 3.11. For 5 Kg TNT, it is observed that there are some cracks on the bottom face of the front RC panel (but retains in its coherent form) and there is no damage occurs on the helical springs and the back panel. For 10 Kg TNT, it is observed that the front RC panel is damaged and fragmented into two pieces. There are some hairline cracks on the front face of the back RC panel. There is no damage occurs on the helical springs. In addition, it is observed that the main crack of the front RC panel occurred in the axis where there are no springs except the middle spring.

Figure 3.12 shows the experimental observations on the RHR-7 under the three different blast loads considered. Table 3.3 shows the maximum displacement values recorded for the front RC panel RHR-7 under 1 and 5 Kg TNT at a SoD of 1 m. In the case of 10 Kg TNT, the front RC panel is totally damaged and fragmented into pieces.

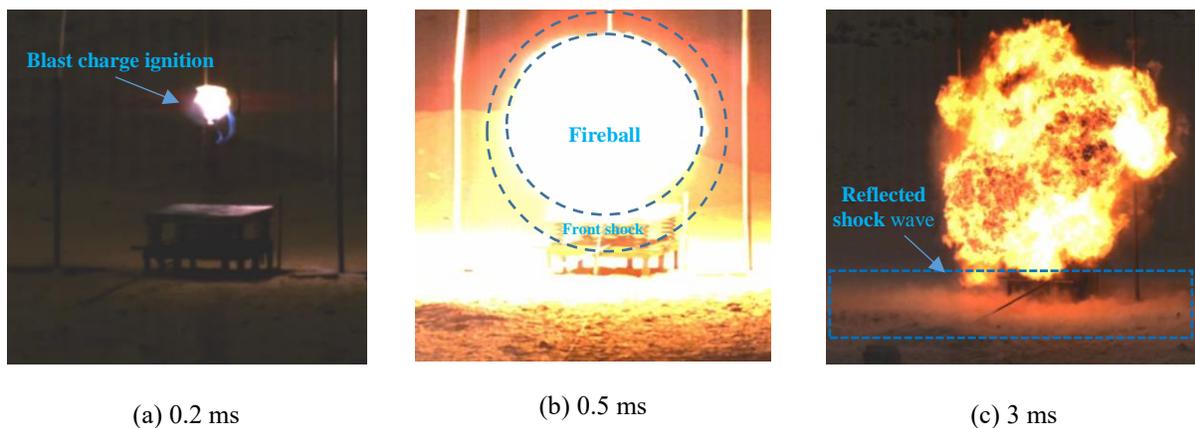


Figure 3.11 Free air explosion process scenes of RHR-7 under 1 kg TNT at a SoD of 1 m



The fireball of the 1 Kg TNT



No cracks on the front RC panel

RHR-7 under 1 Kg TNT



Cracks on the back face of the front RC panel



No crack on the back RC panel

RHR-7 under 5 Kg TNT



The front RC is totally damaged



Hairline cracks occur on the front face of the back RC panel

RHR-7 under 10 Kg TNT

Figure 3.12 Experimental observation on the RHR-7 after applying different blast loads

Table 3.3 Maximum displacement of RHR-7 under different blast loads

TNT weight (Kg)	1	5	10
Maximum displacement (mm)	20	62	Totally damaged

3.4.3.2 RHR-9

In this section, the RHR sandwich panel with nine helical springs in the interlayer, named RHR-9, is subjected to a blast load of 7.5 Kg TNT at a SoD of 1 m. The result shows that there are considerable cracks appear on the front face of the front RC panel and its sides (but still coherent without being fragmented). There is no damage occur on the helical springs and the back RC panel.

Figure 3.13 shows the experimental observation of the blast tests on the RHR-9. The maximum displacement recorded for the front RC panel of the RHR-9 under blast loads detonated from 7.5 Kg TNT at a SoD of 1m is 66 mm.



Cracks on the front RC panel



Cracks on the front RC Panel side



No cracks on the back RC panel

Figure 3.13 Experimental observation on the RHR-9 under 7.5 Kg TNT at SoD of 1 m

3.4.3.3 RHR-16

In this section, the RHR sandwich panel with sixteen helical springs in the interlayer, named RHR-16, is subjected to three blast loads of 1Kg, 5 Kg and 10 Kg TNT at a SoD of 1 m. For 1 Kg TNT. It is observed that there are no cracks appear on the front face of the front RC panel and there is no damage occur on the helical springs and the back RC panel. For 5 Kg TNT, it is observed that there are considerable cracks on the front face of the front RC panel and its sides (totally damaged but still coherent) and there is no damage occurs on the helical springs and the back RC panel. For 10 Kg TNT, it is observed that the front RC panel is damaged and fragmented into pieces. Cracks

occurred on the front face of the back RC panel. However, it is still in a coherent status. There is no damage occur on the helical springs.

Figure 3.14 shows the experimental observation of the three blast tests on the RHR-16. Table 3.4 shows the maximum displacement values recorded for the front RC panel RHR-16 under 1 and 5 Kg TNT at a SoD of 1 m. In the case of 10 Kg TNT, the front RC panel is totally damaged and fragmented into pieces.



No cracks on the front RC panel



No cracks on the back RC panel

RHR-16 under 1 Kg TNT



Cracks on the front face of the front RC panel



Cracks on the side of the front RC panel



No crack on the back RC panel
RHR-16 under 5 Kg TNT



The front RC is totally damaged



Hairline cracks occur on the front face of the back RC panel

RHR-16 under 10 Kg TNT

Figure 3.14 Experimental observation on the RHR-16

Table 3.4 Maximum displacement of the RHR-16 under different blast loads

TNT weight (Kg)	1	5	10
Maximum displacement (mm)	9	37	Totally damaged

3.5 Summary

It is hard and time-consuming to accurately simulate the performance of the RHR sandwich panel under repetitive blast load. In order to show the realistic performance of the RHR sandwich panel,

experimental blast tests should be conducted and then its results should be used to validate the developed finite element model. In this Chapter, a new protective sandwich panel, named the RHR sandwich panel, is examined and evaluated experimentally under different levels of free air blast loads. These RHR sandwich panels are subjected to repetitive free air blast loads. A parametric study is applied by changing the helical springs interlayer stiffness and the range of the blast load. The observation results show that the RHR sandwich panel can withstand repetitive blast loads within the studied range. The location of the helical springs in the interlayer affects the damage pattern of the front and back RC panels of the RHR sandwich panel. Besides, changing the stiffness of the helical springs interlayer affects the displacement of the front RC panel. For the blast loads of 1 and 5 Kg TNT, the displacement of the front RC panel decreases as the stiffness of the helical springs interlayer increases. For the blast load 10 Kg TNT, the damage pattern of the front RC panel changes with changing the location and the number of helical springs. In the RHR-7, the front RC panel is mainly fragmented into two parts in the axis where no supported springs occur except the middle spring. Whereas, in the case of RHR-16, the front RC panel is fragmented into pieces due to the uniform distribution of the supported helical springs.

Chapter 4: Analytical modeling of concrete material under hyperdynamic load

Due to the porosity and heterogeneity nature of the concrete material, it is difficult to simulate the nonlinear behavior and the damage pattern of concrete structures when subjected to blast loads with a simple constitutive model. In this thesis, before conducting the numerical investigation on the RHR sandwich panel, a 3D nonlinear numerical study is conducted to examine the behavior of concrete material under various loading conditions using Riedel-Hiermaier-Thoma (RHT) model. Based on the material level testing, detailed calibration is conducted to identify the optimal parameters for the RHT model to better simulate the behavior of a single concrete element. For the component level testing, the calibrated RHT parameters are used to simulate the failure behavior of plain concrete (PC) panel under free air blast load. The response is compared with an available experimental result.

4.1 Literature review

Concrete material has a sophisticated nonlinear behavior under the normal loading conditions in which its behavior cannot be simulated accurately using a simple constitutive model. Furthermore, when concrete material subjected to high dynamic load, large deformation occurs and a complicated stress-strain curve is produced due to the strain rate effects (Riedel et al., 2009; Zhou and Hao, 2008). The nonlinear behavior of concrete structures can be modeled using mesoscale and macro-scale approaches (Gebbeken and Ruppert, 2000; Govindjee S, Gregory JK, 1995; Hentz et al., 2004; Malvar et al., 1997). Mesoscale modeling is more advanced but more complicated and time-consuming. Usually, the macro model is computationally more efficient, but not able to accurately predict the localized damage of the concrete structure. In this Chapter, a robust 3D macro model, based on the RHT model (Riedel W, Thoma K, 1999; Riedel, 2009, 2000; Riedel et

al., 2008), is proposed to simulate the nonlinear dynamic response of concrete panel under blast loading using AUTODYN program. Detailed geometric and material nonlinearities are considered. AUTODYN program is an explicit dynamic software, which is commonly used to predict a reliable nonlinear dynamic performance of structures under hyperdynamic loads such as blast loads and high velocity bullet penetration. This hydrocode uses an explicit numerical algorithm in which the coupled momentum and energy conservation with materials descriptions (equation of state (EOS) and constitutive model) are solved simultaneously. Hydrocodes are computer programs, which can be used to numerically simulate the behavior of hyperdynamic loads such as shock, high impact, and blast loads (Anderson, 1987). More details about hydrocodes numerical algorithms and methods can be found in Anderson, (1987); Benson, (1992, 1990) and Zukas, (2004).

In this study, modification of effective parameters is proposed to yield the strain softening range to a more realistic descending process, for both tension and compression loading conditions, in order to demonstrate an accurate crack pattern simulation. In the past, a series of modified RHT models have been used to simulate the nonlinear response of different concrete structures (Codina et al., 2016; Hu et al., 2016; Nyström and Gylltoft, 2011a, 2009; Tu and Lu, 2010, 2009; Wang et al., 2013). The simulation results of these studies show that the modified RHT models can better predict the dynamic behavior of concrete against blast loads. Tu and Lu (2010 and 2009) examined and evaluated the nonlinear dynamic behavior of concrete using the RHT model with the default parameters implemented in (ANSYS-AUTODYN, 2005) (referred to hereinafter as the default RHT model). It was found that the default RHT model gives poor behavior under blast loads. Accordingly, Tu and Lu (2010 and 2009) modified the default parameters to improve the accuracy of the numerical model to simulate the nonlinear behavior of a one-way reinforced concrete (RC)

panel fixed from its two short sides and subjected to confined blast load. The result shows that the proposed modified parameters can simulate the crack patterns observed in the physical test better than the default parameters.

Similarly, Hu et al. (2016) proposed another modified RHT model to simulate better the blast behavior of a plain concrete (PC) panel fixed to the ground using four anchors at its four corners. The PC panel was subjected to a close-in blast load at a standoff distance (SoD) of 170 mm above the center of the specimen. It was found that the default RHT model underestimates the crack pattern and crater diameter. Whereas, the proposed RHT model decreases the ductility of the model to estimate better the crack pattern and crater diameter observed during the experimental test.

Wang et al. (2013) used the modified RHT model proposed by Tu and Lu (2010 and 2009) with a slight change in the reference density and failure strain to simulate the blast behavior of a one-way RC panel subjected to close-in blast load. By comparing the numerical results with the corresponding experimental observations, it was found that the modified RHT model can model the crack patterns well but slightly overestimates the concrete spalling.

Similarly, Codina et al. (2016) modified some of the RHT parameters and used them to simulate the behavior of a RC column against blast loads located at a short distance for the column. In addition, they compared their proposed parameter with the modified RHT parameters proposed by Tu and Lu (2010 and 2009). It was found that the default and the proposed RHT parameters by Tu and Lu show more significant damage contours than those observed on the physical tests. In contrast, the modified parameters developed by Codina et al. (2016) were able to provide a more

accurate prediction of the damage pattern and maximum displacement. Similarly, Nyström and Gylltoft (2009) proposed another set of modified RHT parameters to simulate the blast behavior of a simply supported RC wall subjected to blast loads.

In general, all the aforementioned modified RHT parameters can be used to model the response of concrete structures under different loading conditions. However, the accuracy of the model varied significantly with the specimen dimensions, loading conditions, boundary and initial conditions. Based on the numerical investigation presented in this study, the aforementioned RHT parameters cannot accurately model the nonlinear behavior of simply supported PC panels under a free blast load. Hence, in this study, a new set of RHT parameters are proposed to accurately simulate the damage pattern and the crack trajectory of a simply supported PC panel subjected to free air blast load. The newly proposed RHT parameters are used to simulate the nonlinear behavior of the concrete at the material level by applying unconfined uniaxial, equal biaxial and triaxial tension and compression tests on a single finite element of concrete. The stress-strain curves show that the newly proposed RHT model is able to simulate the strain softening behavior of the concrete material more accurately than the default RHT model.

Besides, on the component level, an experimental and numerical application is conducted on a simply supported PC panel under a free blast load. The crack trajectory and damage pattern observed from the experimental test and the nonlinear numerical simulation are compared. The result shows that by using the newly proposed parameters, the RHT model can accurately simulate the blast behavior of a PC panel under free air blast loads.

4.2 Theory of RHT model

RHT model is one of the most well known numerical models, which commonly used to simulate the brittle material like concrete. The RHT material model employs three strength surfaces to define the elastic limit surface (or initial surface), failure surface and residual surface (or post-failure surface) as shown in Figure 4.1 (Riedel W, Thoma K, 1999; Riedel, 2000; Riedel et al., 2008).

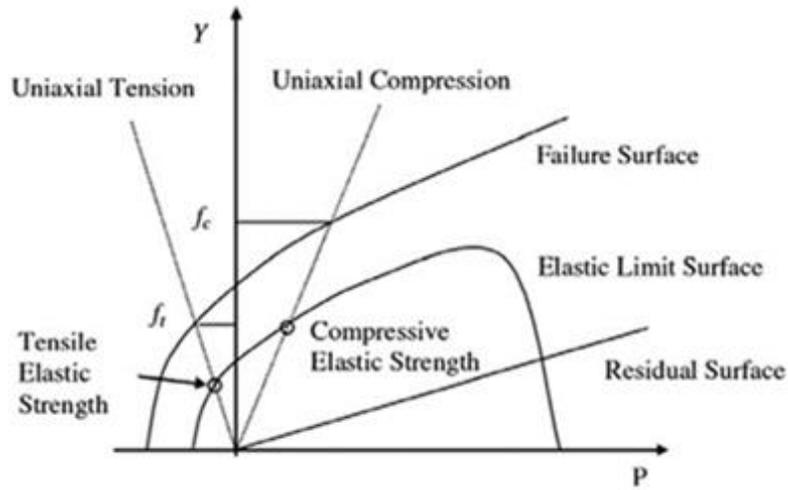


Figure 4.1 Three strength surfaces of the RHT model (Riedel *et al.* 1999)

The three surfaces can be expressed using the following equations 4.1 - 4.3:

$$Y_{\text{elastic}} = Y_{\text{failure}} \times F_{\text{elastic}} \times F_{\text{cap}} \quad (4.1)$$

$$Y_{\text{failure}} = Y_{\text{TXC}}(p) \times R_3(\theta) \times F_{\text{rate}}(\dot{\epsilon}) \quad (4.2)$$

$$Y_{\text{residual}} = f_c \times B \times \left(\frac{p}{f_c}\right)^M \quad (4.3)$$

Where Y_{elastic} is the elastic limit surface; Y_{failure} is the failure surface; F_{elastic} the ratio of the elastic strength to failure strength along a radial path; F_{cap} is a parabolic function; $Y_{\text{TXC}}(p)$ is the compressive meridian which is a function of hydrostatic pressure (p); $R_3(\theta)$ is a reduction factor

of the failure surface $Y_{failure}$, which is a function of the Lode angle (θ), which represent the rotation about the hydrostatic axis; $F_{rate}(\dot{\epsilon})$ is the dynamic amplification factor (DIF) as a function of strain rate $\dot{\epsilon}$; $Y_{residual}$ is the residual surface; f_c is the uniaxial compressive strength; B is the fractured strength constant and M is the fractured strength exponent.

In this Chapter, a modification has been applied to RHT strength and failure model parameters (B , M , D_1 , D_2 and e_{min}^{fail}), where B and M control the residual and affect the post-failure surfaces, as illustrated in equation 4.3. While D_1 , D_2 and e_{min}^{fail} , as illustrated in equations 4.4 to 4.6, control the concrete post-softening behavior.

$$D = \int_0^{\epsilon_p} \left(\frac{\Delta \epsilon_p}{D_1 (p^* - f_t/f_c)^{D_2}} \right) \quad \text{for } D_1 (p^* - f_t/f_c)^{D_2} > e_{min}^{fail} \quad (4.4)$$

$$D = \int_0^{\epsilon_p} \left(\frac{\Delta \epsilon_p}{e_{min}^{fail}} \right) \quad \text{for } D_1 (p^* - f_t/f_c)^{D_2} < e_{min}^{fail} \quad (4.5)$$

$$e_{min}^{fail} = \frac{2 \times G_f}{\sigma_t \times L_{eq}} \quad (4.6)$$

Where D is the damage parameter; $\Delta \epsilon_p$ is the plastic strain increment; D_1 and D_2 are the shape parameters; $p^* = p/f_c$ is the normalized pressure variable; G_f is the fracture energy; σ_t is the tensile failure stress; L_{eq} is the characteristic length of the element (the diameter of a sphere having the same volume of the 3D element (ANSYS-AUTODYN, 2005)).

Based on the comparative numerical tests on the material level and the experimental and numerical application conducted on the component level, a new set of the RHT parameters is proposed. These modified parameters are defined to ensure a more realistic strain softening range, for both tension and compression loading conditions. Table 4.1 shows the main effective parameters of the default and the newly proposed RHT models in this study.

Table 4.1 The main effective parameters of the default and newly proposed RHT models in this study

Parameters	Default RHT model	Proposed RHT model
Fractured Strength Constant B	1.6	0.9
Fractured Strength Exponent M	0.61	0.9
Damage Constant D_1	0.04	0.02
Minimum Strain to Failure e_{min}^{fail}	0.01	0.002

4.3 Numerical analyses on a single concrete finite element

To evaluate the newly proposed RHT parameters, a single concrete element, with a size of 10 mm, is simulated using the default and proposed RHT models and subjected to different loading conditions. The tested loading conditions are unconfined uniaxial compression and tension loading condition, equal biaxial compression and tension loading condition, triaxial tension loading condition and triaxial compression loading condition with different levels of confinement (1 MPa, 5 MPa, 10 MPa and 20 MPa). The single concrete element is modeled as a Lagrangian element (ANSYS-AUTODYN, 2005). The loads are applied by moving the four nodes perpendicular to the element surface with a constant velocity. To avoid the influence of the strain rate effect, a suitable velocity should be applied to the single element, which is able to simulate the effect of the

normal loading cases. After applying some trials on the unconfined uniaxial test, a nodal velocity of value 10^{-5} m/s is nominated, which can achieve the desired yield strength value. It should be noted that a smaller nodal velocity can be used, but it will significantly increase the computational time. The boundary conditions are constrained such that the element can only deform under the direction of the load without any shear stresses. Figure 4.2 shows the finite element model developed for this study. Finally, the results are expressed in the form of an axial stress-strain curve for each load condition. These stress-strain curves show the capability of the default and proposed RHT models in representing the realistic strain softening behavior.

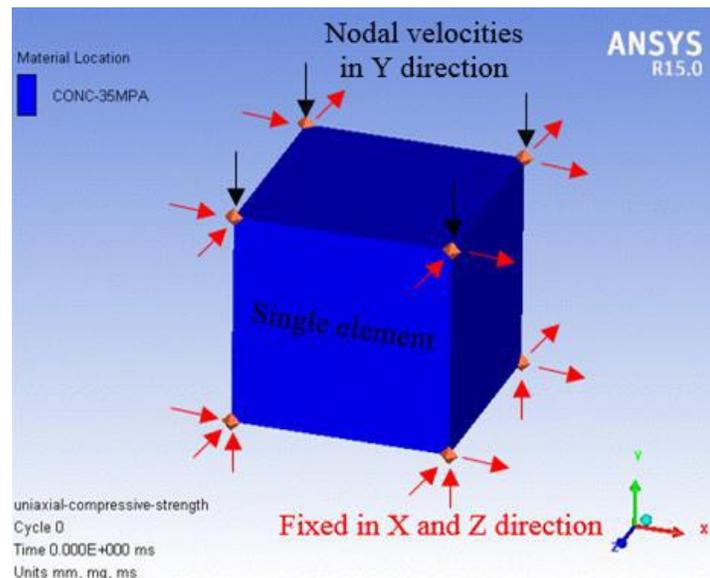
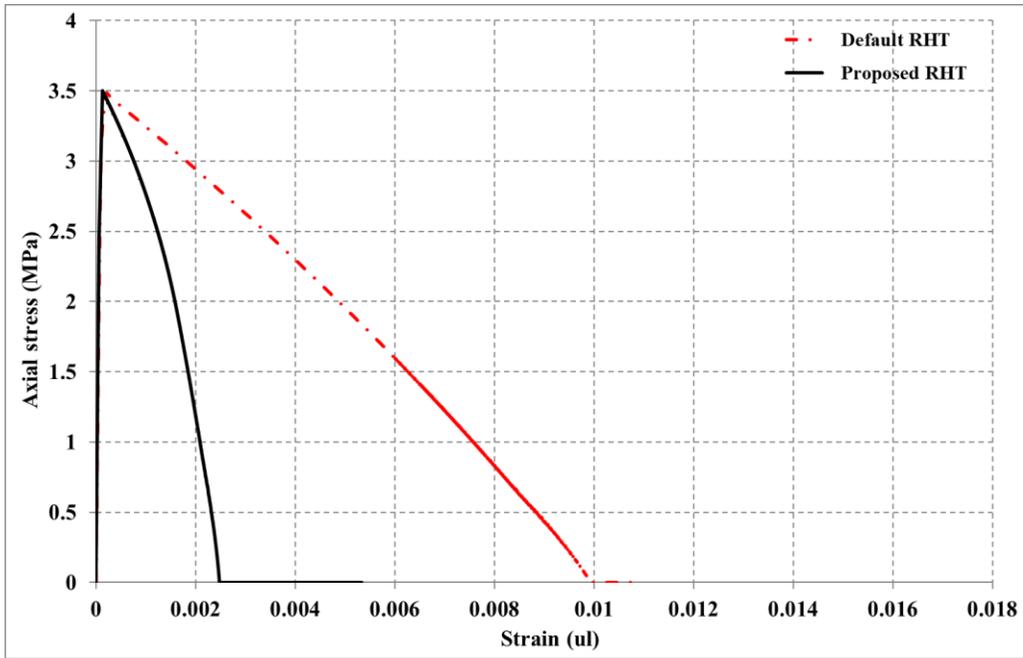


Figure 4.2 Uniaxial numerical compression test on a single concrete finite element

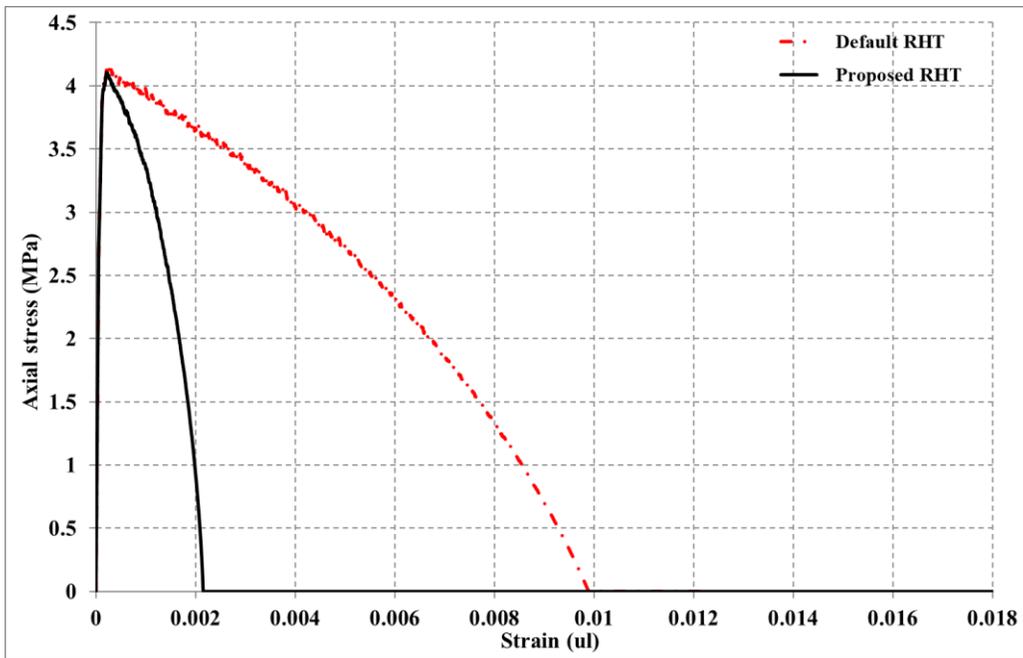
4.4 Numerical results and discussion

Figures 4.3 and 4.4 show the comparison between the axial stress-strain curves of the concrete material using the default RHT model and newly proposed RHT models under different loading cases. The results show that the default RHT model overestimates the strain softening range for

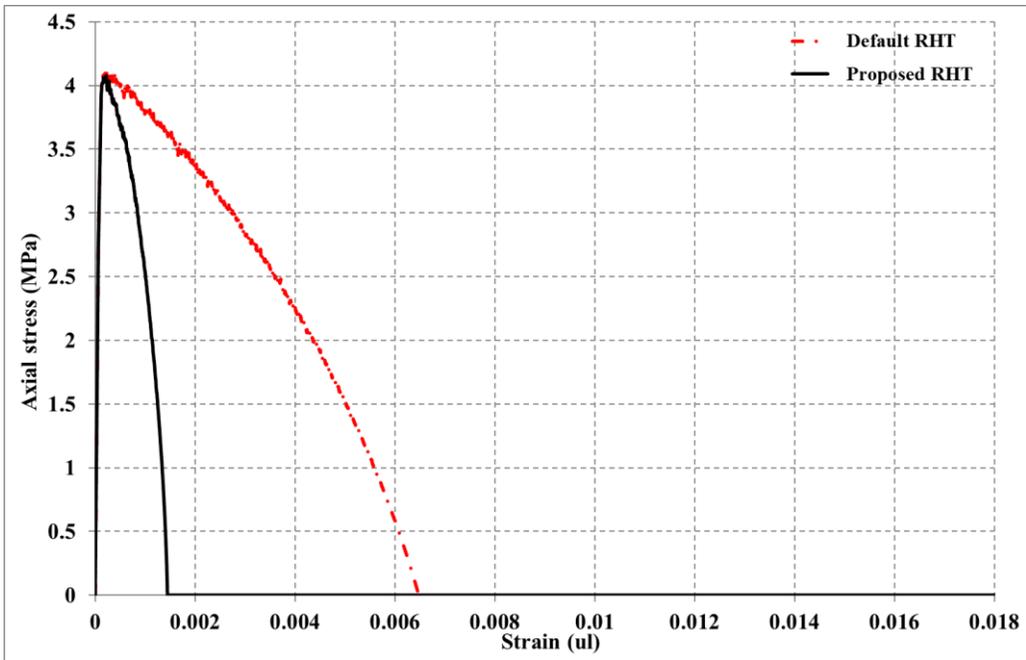
both the tension and compression tests based on the common experimental results (Chen, 1982; Malvar et al., 1997; Tu and Lu, 2009; Zhang et al., 2007).



(a) Unconfined uniaxial

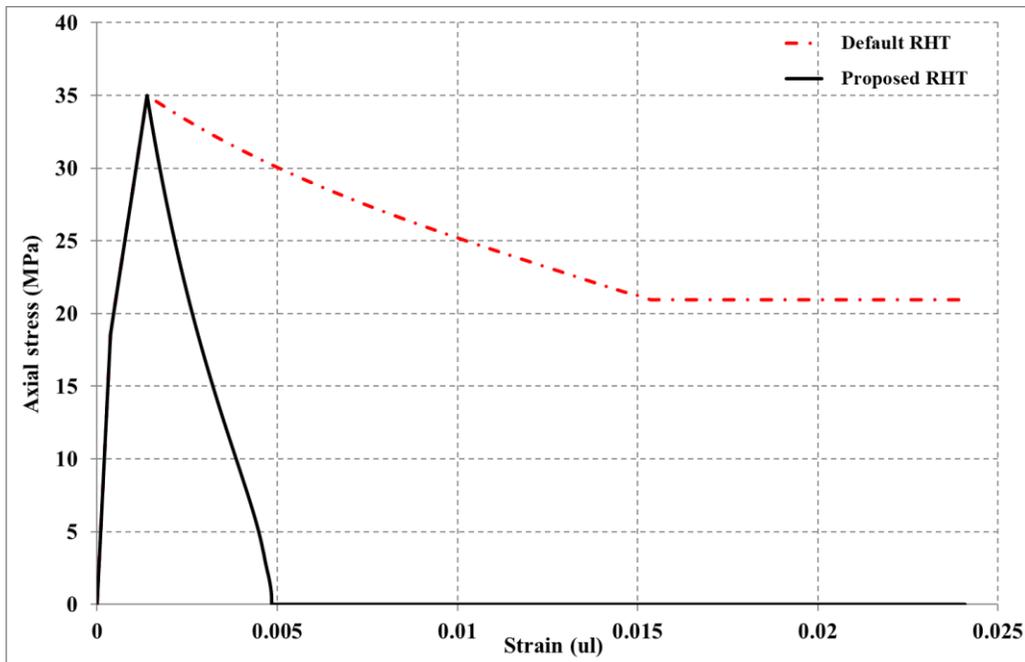


(b) Equal biaxial

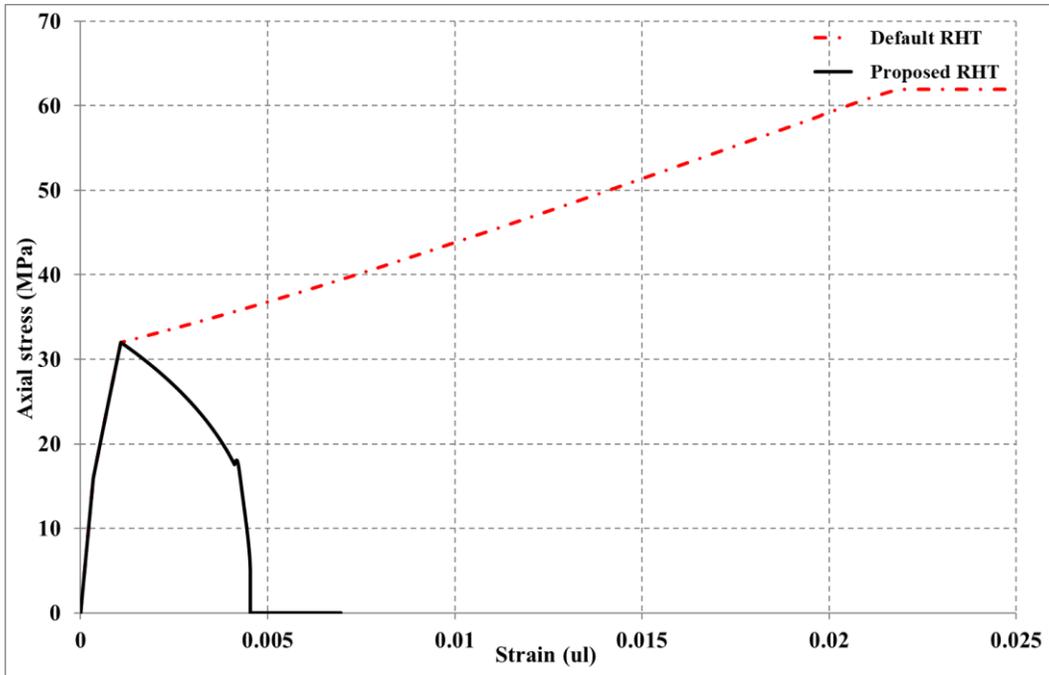


(c) Hydrostatic triaxial

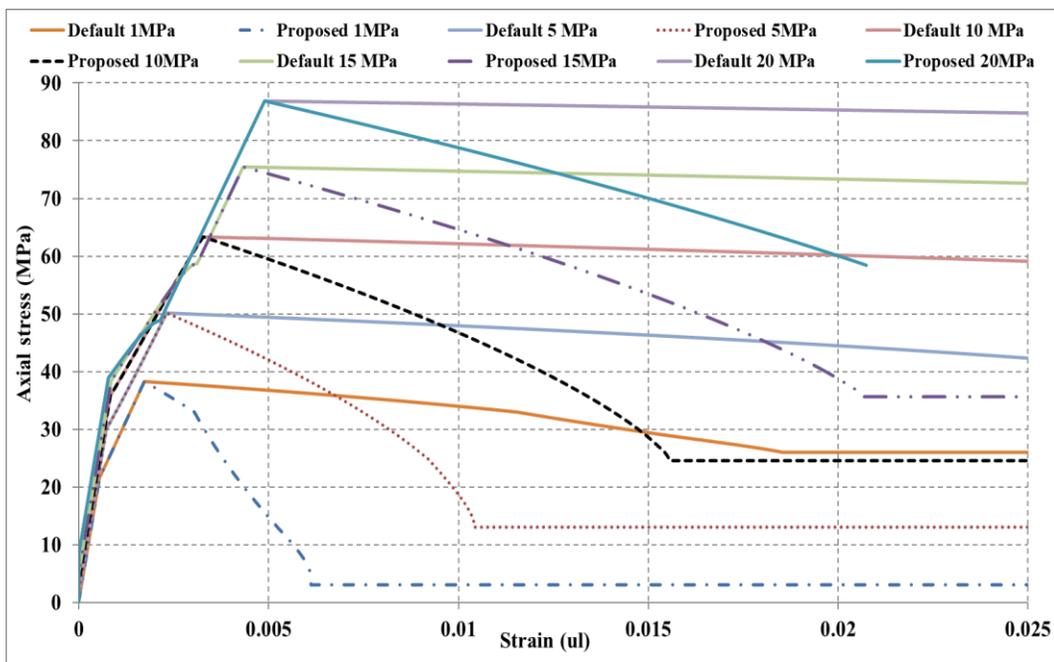
Figure 4.3 Axial stress-strain curves of the default and proposed RHT models for tension



(a) Unconfined uniaxial



(b) Equal biaxial



(c) Triaxial with levels of confinement

Figure 4.4 Axial stress-strain curves of the default and proposed RHT models for compression

It is found that the proposed RHT parameters yield the post failure behavior of the stress-strain curves under the different compression and tension loading patterns to a reasonable value. Under the tension case, the strain softening behavior is enhanced and the minimum failure strain e_{min}^{fail} is decreased to a reasonable value, which showed a more accurate failure pattern when compared with the corresponding experimental results (Chen, 1982; Malvar et al., 1997). For compression tests, the default RHT model shows unrealistic high residual strength after reaching the failure strength, as shown in Figure 4.4. This high residual strength is attributed to the simplification of the residual strength surface in the default RHT model, which exhibits a circular deviatoric cross-section plane in the principal stress space. This inaccurate strain softening behavior is significantly modified by changing the value of the Fractured Strength constant (B) and Fractured Strength Exponent (M), which control the final residual strength. Accordingly, a considerable reduction occurred on the final residual strength and the compression failure strain, as shown in Figure 4.4, which became more acceptable compared with the corresponding laboratory tests (Zhang et al., 2007). In addition, the damage Constant (D_1) is decreased to better simulate the degrading portion of the concrete material. For the triaxial compression test, it can be noted that with the increasing of the confining level, the maximum compression strength increases, which agrees with the common experimental results. In addition, based on similar experimental results (Lu and Hsu, 2007; Malvar et al., 1997), an enhancement occurred in the post softening curve and the residual strength for each confinement level compared with that obtained by using the default RHT model.

4.5 Experimental and numerical application on a PC panel against a free air blast load

4.5.1 Experimental test

As mentioned in Chapter 3, in order to examine and evaluate the default and proposed RHT model parameters, an experimental test, on a simply supported PC panel subjected to free air blast load, is conducted, as shown in Figures 3.5. The dimension of the specimen is 1 m x 1 m with a thickness of 20 cm. In this test, the PC panel is subjected to 4 Kg TNT detonated at a SoD of 1 m from the center of the specimen. A field test rig, as shown in Figure 4.5, is used to simulate the simply supported boundary conditions of the PC panel at four edges. After verifying the pressure time history as mentioned in the previous Chapter, the PC panel is tested under 4 Kg TNT at a SoD of 1 m. Figure 4.5 shows some of the crack trajectories that occurred after applying the blast load.



Figure 4.5 Damage pattern of the PC panel after applying the blast load

4.5.2 Numerical analysis

To simulate the nonlinear behavior of the PC panel against blast load, a numerical model, as shown in Figure 4.6, is developed. Due to the dual axis of symmetry, only a quarter numerical model is

developed. More than 2.3 million elements are used for this numerical model. Consistent boundary conditions are applied to simulate a similar environment as in the arena test. Flow out boundary condition is applied to the outer faces of the air block except for the symmetric faces. In this study, a fluid-structure coupling algorithm is used to apply the blast load on the PC panel. The methodology of this algorithm is that the air and explosion environment are modeled by the Eulerian process, which can represent large deformation through fixed meshes. These Eulerian meshes exert a pressure boundary condition on the Lagrangian meshes, which represent the PC panel. Accordingly, Lagrangian elements experience deformation through the fixed Eulerian meshes and exert a velocity boundary condition to the Eulerian material flow. Finally, the response of the PC panel against explosion loads can be analyzed in a single numerical model using the coupled Lagrangian-Eulerian algorithm (ANSYS-AUTODYN, 2005; Benson, 1992).

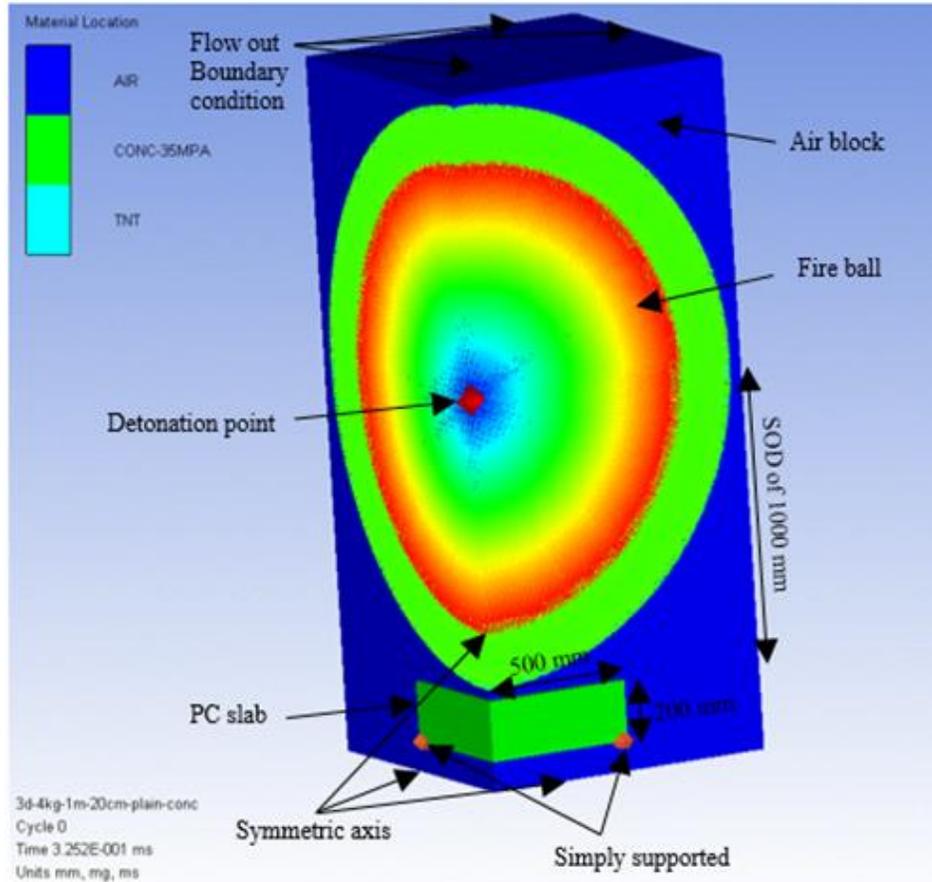


Figure 4.6 A quarter numerical model of the PC panel subjected to free air blast load

4.5.2.1 Numerical modeling of the explosion process

To accurately simulate the TNT explosion process, a numerical analysis is performed to model a free air blast test where a 1 Kg TNT detonated at a SoD of 1 m. The numerical result is then compared with that measured in the field and that calculated by empirical equations provided by TM5 (TM5-1300, 1990), implemented in the CONWEP program. In this model, the air is modeled using the Hydro (ideal gas) equation of state (EOS), as it represents no strength and can be written in the form of equation 4.7 (ANSYS, 2007). TNT is modeled using the Jone Wilkins-Lee (JWL) model (ANSYS, 2007), which can be written in the form of equation 4.8. JWL model is used

because it can simulate the rapid expansion of TNT when detonated. After the TNT is detonated, the pressure created by the TNT detonation is modeled using ideal gas EOS (equation of state). Ideal gas EOS is widely used due to its simplicity and yet it can simulate the pressure created by the explosion very well (ANSYS, 2007). Table 4.2 shows the property of the air and TNT used in this study.

$$P_{EOS} = (\gamma - 1)\rho e \quad (4.7)$$

$$P_{EOS} = A \left(1 - \frac{w}{R_1 V}\right) e^{-R_1 V} + B \left(1 - \frac{w}{R_2 V}\right) e^{-R_2 V} + w \frac{E}{V} \quad (4.8)$$

Where P_{EOS} is the pressure; γ is a constant; ρ is air density; e is the specific internal energy; A , B , R_1 , R_2 , and w are the JWL parameters, presented in Table 4.3, that are used to model the air and TNT material; $V = \frac{\rho_{SOL}}{\rho}$, where ρ and ρ_{SOL} are the current and solid density of the explosive, respectively; $E = \rho_{SOL} e_{int}$ = the internal energy per unit volume of the explosive, where e_{int} is the current internal energy per unit mass.

Table 4.2 Material data of the air and TNT used in modeling (ANSYS-AUTODYN, 2005)

Material	Air	TNT	TNT (Ideal)
Equation of State	Ideal Gas	JWL	Ideal Gas
Initial Conduction	$\rho = 1.225 \times 10^{-3} \text{ g/cm}^3$	Default	From Detonation
Density	$1.225 \times 10^{-3} \text{ g/cm}^3$	Library Data	$1.0 \times 10^{-3} \text{ g/cm}^3$
Ideal Gas Constant	$\gamma = 1.4$	Standard	$\gamma = 1.35$
Reference Energy	$2.068 \times 10^5 \text{ } \mu\text{J/mg}$		Model/remap data

Table 4.3 Summary of the JWL parameters used to model TNT

JWL Parameter	TNT
A (GPa)	373.75
B (GPa)	3.747
R ₁	4.15
R ₂	0.90
w	0.35

Once the 1D pressure has been simulated, the pressure is then remapped into a 3D finite element model, as shown in Figure 4.7. This procedure is commonly used by blast engineers to decrease the computational effort, which is needed to simulate the explosion process in a 3D finite element model. In the 3D model, Euler-FCT (Flux corrected Transport) formulation is used to solve the nonlinear dynamic response of the air. Euler-FCT is generally designed to solve gas dynamic problems, which including large deformations and/or fluid flow. Euler-FCT can model air block, where there is no grid distortion in this element. Accordingly, there is no change in the size and shape of the element during analysis. In this case, the time step (Δt) controlled by this element type will be constant throughout the analysis. The boundary condition of the surrounding air is chosen as flow out at the six faces of the air block.

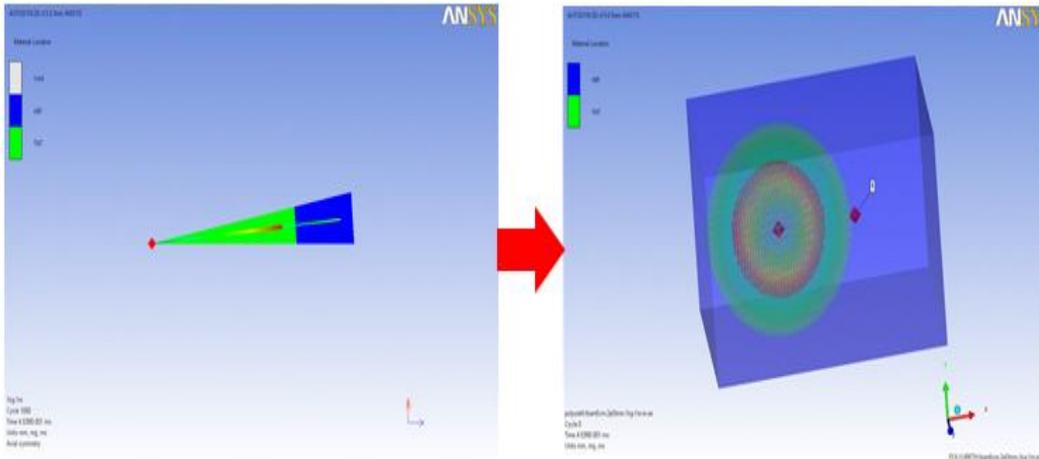


Figure 4.7 Remapping of the air and TNT charge from 1D to 3D

The pressure time history generated from the finite element model is then compared with the experimental result and empirical value, which presented in the TM5 code (TM5-1300, 1990). Figure 4.8 shows the comparison of the pressure-time history obtained from the numerical simulation, empirical calculation, and experimental data. The result shows excellent matching between the experimental and finite element modeling results. Besides, the peak overpressure is compared with the CONWEP program. Figure 4.9 shows the comparison of the peak overpressure values. The numerical result overestimated the measured peak overpressure value by 2.6 % and the empirical equations, implemented in CONWEP, underestimated it by 3 %. The results show that the trend of the numerical pressure time history is similar to that calculated by the CONWEP program.

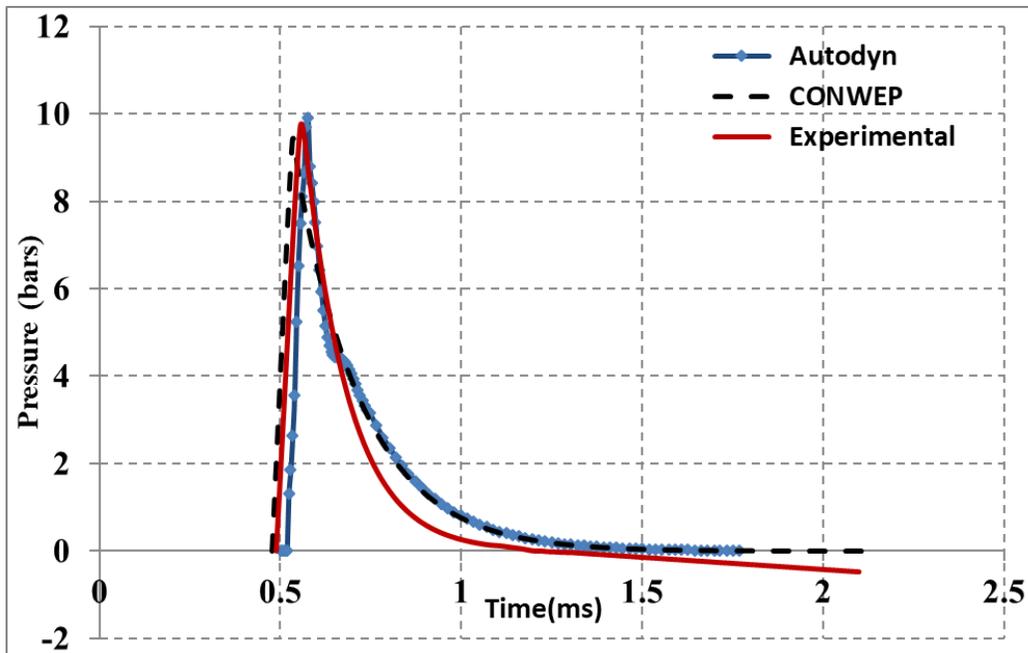


Figure 4.8 Pressure time histories of 1 kg TNT detonated at a SoD of 1 m

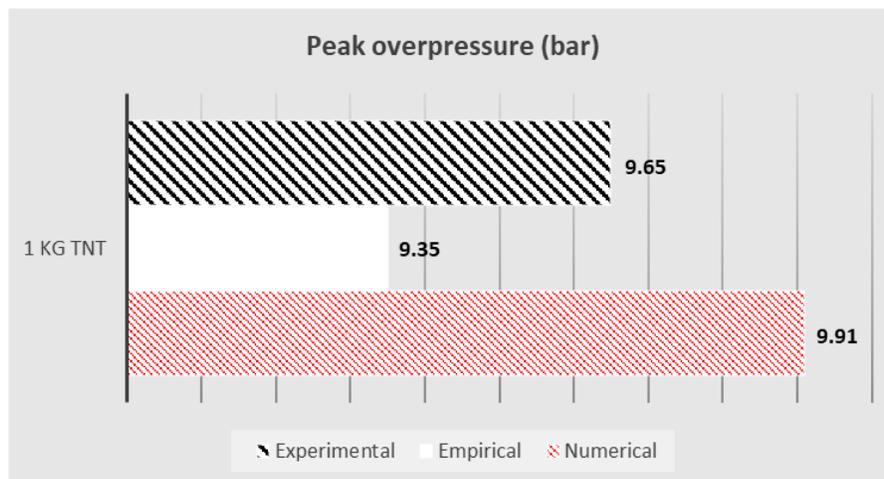


Figure 4.9 Peak overpressure value of a spherical charge of 1 Kg TNT detonated at a SoD of 1 m

4.5.2.2 Numerical modeling of the PC panel

In this study, concrete is modeled using both the porosity EOS and the polynomial solid EOS which can be written in the form of equations 4.9 and 4.10, respectively. This model is capable of

simulating the thermodynamic and compaction behavior of concrete at different levels of pressure (Herrmann, 1969). Figure 4.10 shows the p - α relationship, which represents the porosity EOS and p - ρ relationship, which represents the solid EOS, respectively.

$$\alpha = 1 + (\alpha_p - 1) \left[\frac{p_s - p}{p_s - p_e} \right]^n, \alpha = \frac{v}{v_s} \quad (4.9)$$

Where α_p is porosity corresponding to the initial plastic yield; p is current pressure, n is the compaction exponent; v is the specific volume of the porous material and v_s is the specific volume of concrete in the solid state at the same pressure and temperature. v_s is equal to $1/\rho_s$ at zero pressure, and ρ_s is solid density, which is the density at zero pressure of a fully compacted solid.

$$\begin{aligned} p &= A_1\mu + A_2\mu^2 + A_3\mu^3 + (B_0 + B_1\mu)\rho_0 e, \quad \mu \geq 0 \text{ (compression)} \\ p &= T_1\mu + T_2\mu^2 + B_0 \rho_0 e, \quad \mu < 0 \text{ (tension)} \end{aligned} \quad (4.10)$$

Where p is the pressure; $\mu = \rho/\rho_0 - 1$ where ρ is the density of concrete at any instant, and ρ_0 is full compaction density of concrete at zero pressure; e is the internal energy per unit mass and $A_1, A_2, A_3, B_0, B_1, T_1, T_2$ are material constants.

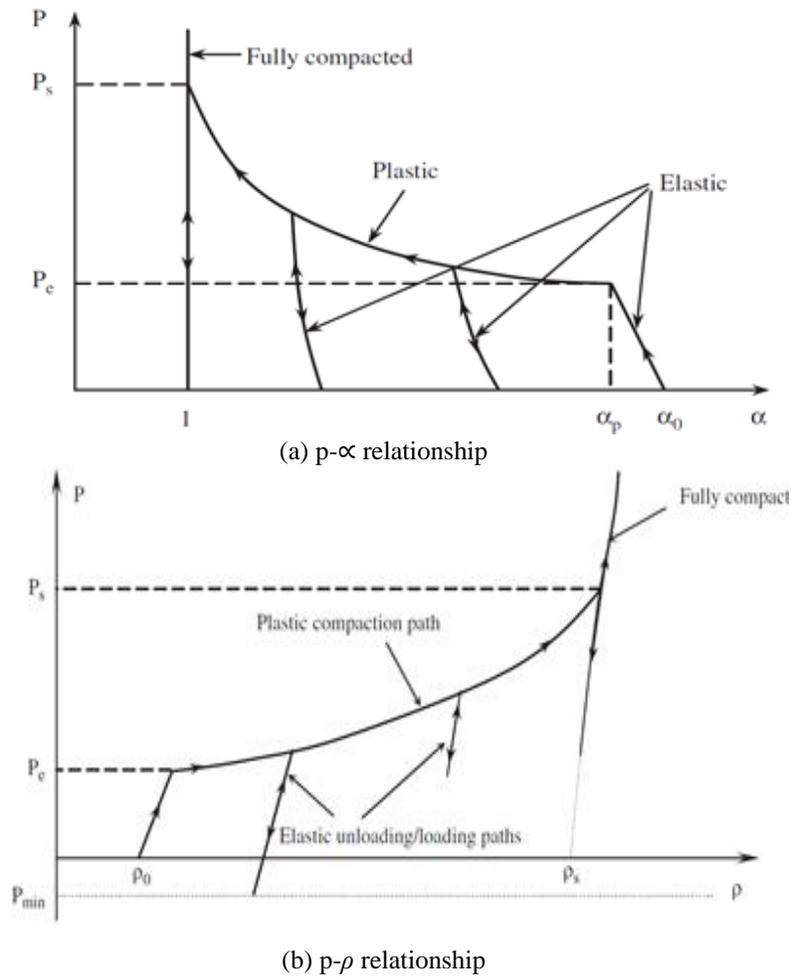


Figure 4.10 Concrete equation of state (Herrmann 1969)

For the concrete strength model and failure model, the RHT model is selected for modeling concrete as mentioned above. Table 4.4 shows the properties of the concrete material used in this numerical study after modifying some effective RHT parameters based on the numerical results obtained from the compression and tension tests, as illustrated in section 4.4. Note that the modified RHT parameters are marked with a blue color.

Table 4.4 Material data of concrete used in this study (ANSYS-AUTODYN, 2005)

Equation of state	P alpha	Shear Strength (f_s/f_c)	0.18
Reference Density (g/cm^3)	2.75	Intact failure surface constant A	1.6
Porous density (g/cm^3)	2.314	Intact failure surface exponent N	0.61
Porous sound speed (m/s)	2.92×10^3	Tens. /Comp. meridian ratio (Q)	0.6805
Initial compaction pressure (KPa)	2.33×10^4	Brittle to ductile transition	0.0105
Solid compaction pressure (KPa)	6×10^6	G (elastic)/(elastic-plastic)	2
Compaction exponent	3	Elastic strength f_t	0.7
Solid EOS	Polynomial	Elastic strength f_c	0.53
Bulk modulus A1 (KPa)	3.527×10^7	Fractured Strength Constant B	0.9
Parameter A2 (KPa)	3.958×10^7	Fractured Strength Exponent M	0.9
Parameter A3 (KPa)	9.04×10^6	Compressive strain-rate exponent α	0.032
Parameter B0	1.22	Tensile strain-rate exponent δ	0.036
Parameter B1	1.22	Max. fracture strength ratio	-----
Parameter T1 (KPa)	3.527×10^7	Use CAP on elastic surface	Yes
Parameter T2 (KPa)	0	Failure	RHT concrete
Reference temperature (K)	300	Damage Constant D_1	0.02
Specific heat (J/kgK)	654	Damage Constant D_2	1

Thermal conductivity (J/mKs)	0	Minimum Strain to Failure e_{min}^{fail}	0.002
Compaction curve	Standard	Residual Shear Modulus Fraction	0.13
Strength	RHT concrete	Tensile Failure	Hydro (P_{min})
Shear modulus G (KPa)	1.67×10^7	Erosion	Geometric strain
Compressive strength f_c (KPa)	3.5×10^4	Erosion strain	2
Tensile strength (f_t/f_c)	0.1	Type of geometric strain	Instantaneous

4.5.2.3 Mesh sensitivity analysis

One of the main factors, which affect the accuracy of numerical results, is selecting a proper element size. A series of convergence numerical simulation is applied to evaluate mesh sensitivity and ensure numerical model accuracy. For the 1D explosion wedge modeling, it is found that choosing an element size of 1 mm for simulating 4 Kg TNT gives maximum peak overpressures that agree well with that calculated from CONWEP with an acceptable error of 6.6 %. After mapping the blast wedge from 1D to 3D, an air block is created with consistent dimensions to cover the entire PC panel and the blast fireball.

For the 3D modeling, different element sizes of 1, 2, 4, 6, 8, 10, 15 and 20 mm are used. It is found that the smaller the mesh size, the more accurate the result. It is noted that when the mesh size is less than 10 mm, the program gives a memory allocation error (ANSYS-AUTODYN, 2005). For

mesh sizes 10, 15 and 20 mm, the errors are 3.9 %, 6.1 % and 11.1 %, respectively when compared with the peak overpressure obtained from the CONWEP program. Accordingly, an element size of 10 mm is used for modeling the air block. In this study, more than 2.3 million elements are used to model the air block. Figure 4.11 shows the mesh sensitivity analysis applied for simulating the explosion environment of 4 Kg TNT at a SoD of 1 m. The red dash line refers to the recorded peak overpressure value in the field, which was 24.52 bars, from the experimental results presented in Chapter 3. The nominated element size gives a peak overpressure of 23.95 bars, where the error between the recorded and numerical results is 2.3 % only, which can be accepted. Decreasing the element size more than the selected value creates too much computational time and memory allocation error (ANSYS-AUTODYN, 2009).

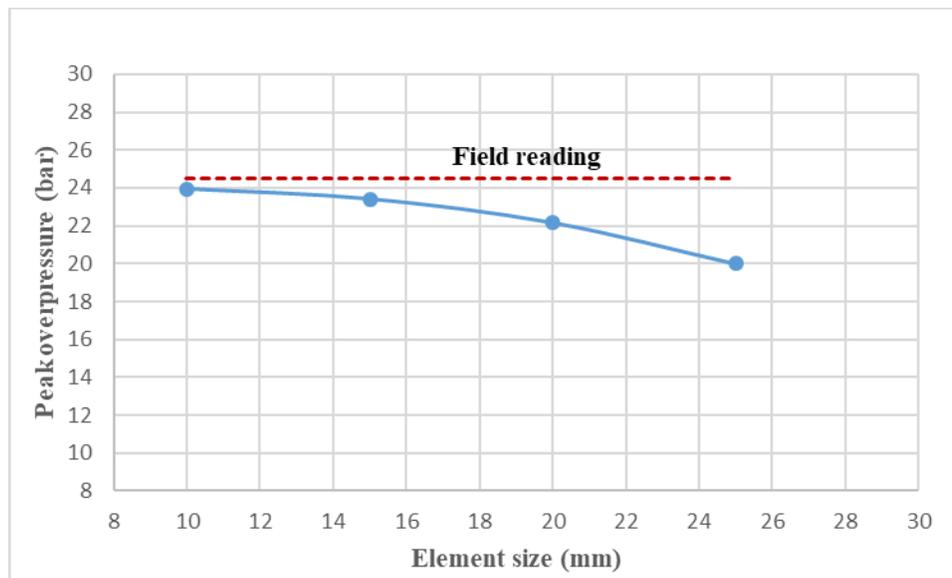


Figure 4.11 Effect of changing air element size on the peak overpressure value of detonating 4 Kg TNT at a SoD of 1 m

The element size of the donor boundary environment (i.e., the air block and the TNT) should be equal or smaller than that of the acceptor body (i.e., RC panel) in order to get a more realistic

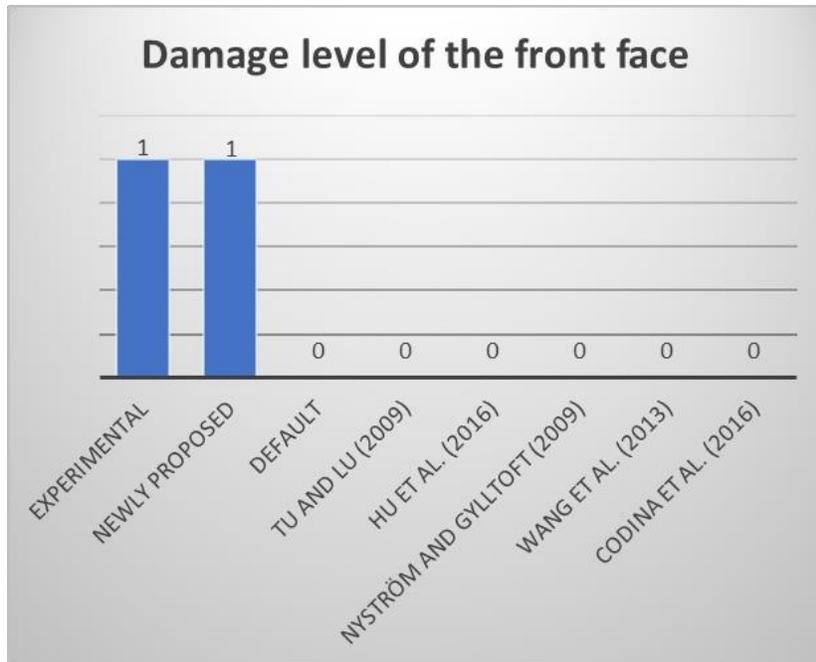
behavior as in the physical tests (ANSYS-AUTODYN, 2005). Accordingly, for the concrete panel, a mesh size of 10 mm is adapted to be consistent with the selected element size for the air block and TNT. In addition, based on similar numerical models (Li et al., 2016; Luccioni B, Araoz G, 2013; Wang et al., 2013), it is found that a mesh of 10 mm gives enough accuracy. In this study, 54,621 elements are used to model the PC panel.

4.5.3 Comparison between the experimental and numerical results

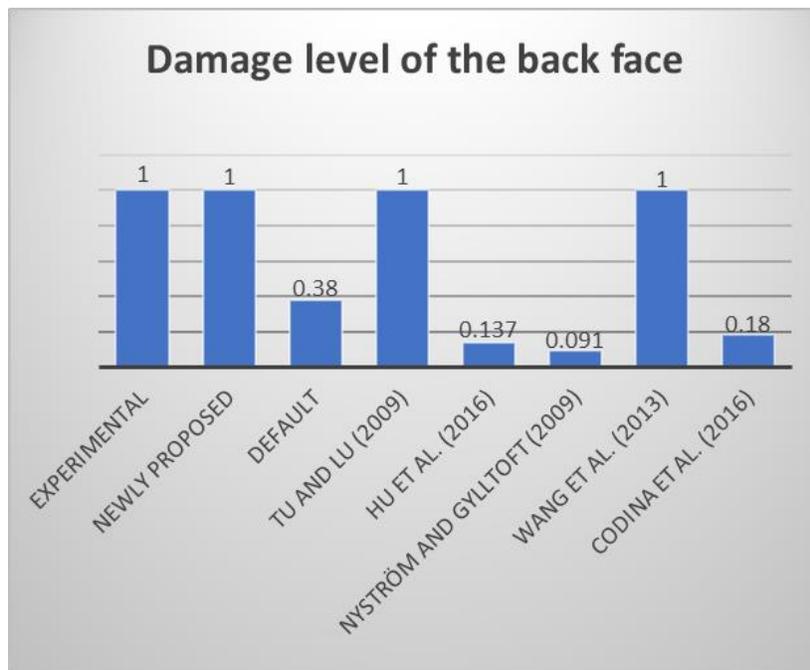
Figure 4.12 shows the damage level (DL) of the PC panel at the midpoint of the front and back faces, which observed during the field test and numerical simulation. The DL, as expressed in equations 4.4 and 4.5, are categorized into four levels according to Li et al., (2014); Xu and Lu, (2006) and Zhou et al., (2008). The four levels are (1) no damage ($DL = 0$ to 0.1), where the RC panel is still in the intact state with small damage area (spots) on the surface; (2) slight damage ($DL = 0.1$ to 0.3), where the panels experienced small (hairline) cracks; (3) medium damage ($DL = 0.4$ to 0.7), where the panel suffers significant cracks but still in the coherent state; (4) severe damage ($DL = 0.8$ to 1.0), where the panel is totally damaged and fragmented. Notice that the red color indicates that the level of damage is 1, where the panel is totally damaged.

When comparing the physical damage level with the numerical result using the default RHT parameters, it is noticed that the DL simulated for the front and back faces of the PC panel were 0 and 0.38, respectively. This result shows that the default RHT model cannot accurately model the DL at the midpoint of the front and back faces of the simply supported PC panel. In the case of using the previous modified RHT models, only the modified RHT models proposed by Tu and Lu (2010 and 2009) and Wang et al. (2013) can accurately simulate the DL at the midpoint of the

back face of the PC panel. In addition, none of them can simulate the physical DL for the front face well. On the other hand, the newly proposed RHT model accurately simulates the DL at the midpoints of the front and back faces of the PC panel well. This result shows that the newly proposed RHT model can be used effectively to simulate the DL for the simply supported PC panel under free air blast load. For the PC panel with the proposed parameters, both the front and the back faces experienced a full compression and tensile failure, respectively. In addition, the tensile failure occurred before the compression failure, as shown in Figure 4.13(b). Accordingly, based on the experimental observation, the numerical results indicate that the proposed RHT model is able to simulate a more realistic behavior of the PC panel under free air blast load than the default RHT model.

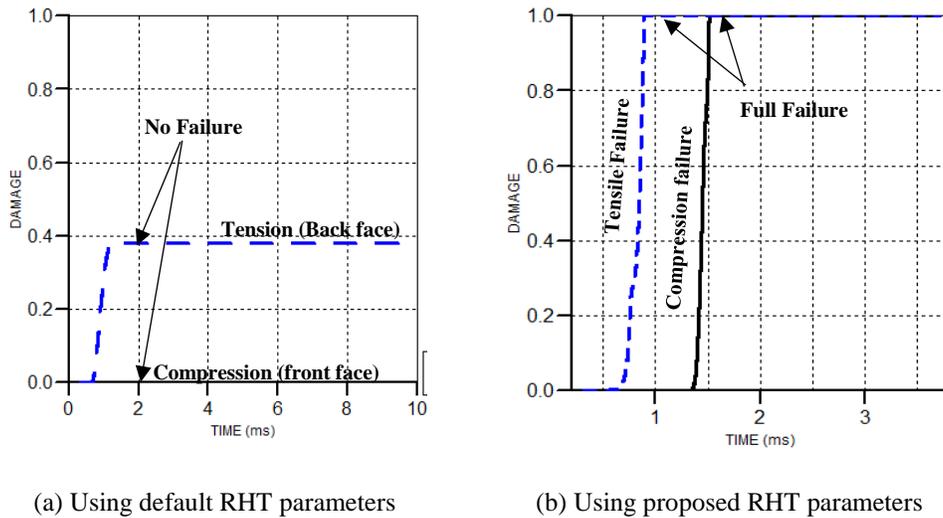


(a) Front face



(b) Back face

Figure 4.12 Damage levels at the midpoint of the front and back faces of the PC panel of the experimental test and that observed from the numerical simulations using the default, newly proposed and previously proposed RHT models



(a) Using default RHT parameters (b) Using proposed RHT parameters

Figure 4.13 Damage level time history at the midpoint of the front and back faces of PC panel using the default RHT parameters and proposed RHT parameters

In addition to the DL study, the crack trajectory and the overall damage pattern, which recorded from the experimental test, are compared to the numerical simulation using the newly proposed RHT model and the other previously modified RHT models (Codina et al., 2016; Hu et al., 2016; Nyström and Gylltoft, 2011, 2009; Tu and Lu, 2010, 2009; Wang et al., 2013). Table 4.5 shows the default and the different RHT parameters used in this numerical study. Figure 4.14 shows the overall damage pattern observed from the experimental and numerical simulations. The damage level scale is shown on the left of Figure 4.14.

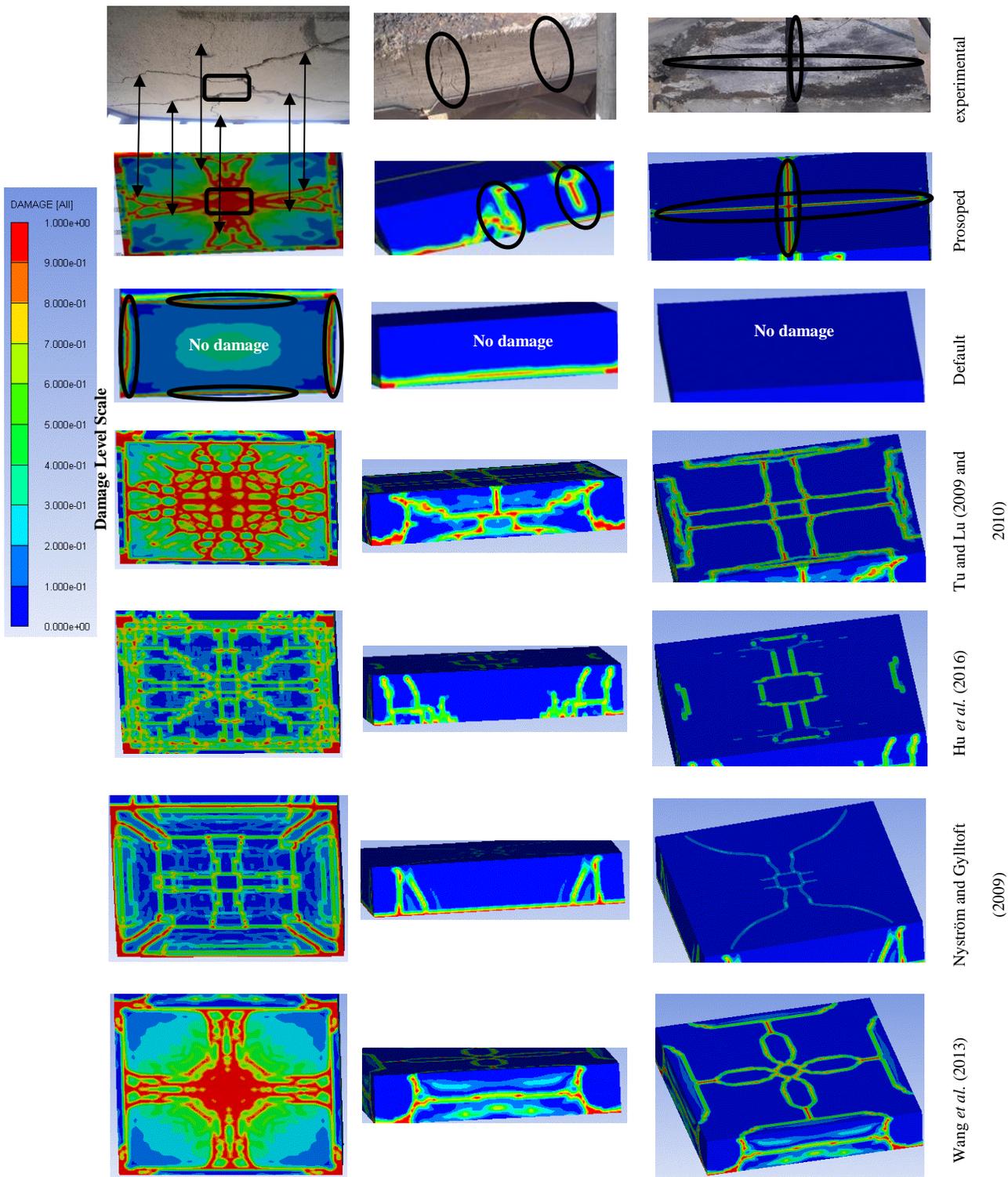
The results show that the newly proposed RHT model can simulate the behavior of simply supported PC panel under free blast loads more accurately than the previously modified RHT models. The RHT model proposed by Tu and Lu (2010 and 2009) overestimates the overall damage pattern and crack trajectory on the front face, back faces and the side of the PC panel. The

RHT model proposed by Hu et al. (2016) underestimates the damage pattern on the front and back faces and no cracks observed on the sides. The RHT model proposed by Nyström and Gylltoft (2009) gives totally different crack patterns in the front and back faces. Similarly, the RHT model proposed by Wang et al. (2013) overestimates the damage pattern and crack trajectory on the back face of the PC panel and the crack pattern on the front face is different from that observed in the experimental test. The RHT model proposed by Codina et al. (2016) appears to be too strong as it makes the behavior of concrete more ductile, where it does not predict any damage in either front or back faces.

Table 4.5 The default, the previous and the newly proposed RHT parameters used in this numerical study

Parameters	Default RHT model	Tu and Lu (2010 and 2009)	Hu et al. (2016)	Nyström and Gylltoft (2009)	Wang et al. (2013)	Codina et al. (2016)	Proposed RHT model
Reference Density (g/cm³)	2.75	2.75	2.75	2.75	2.55	2.55	2.75
Compressive strength, f_c (kPa)	3.5×10^4	3.95×10^4	4.0×10^4	3.5×10^4	3.95×10^4	3.0×10^4	3.5×10^4
Shear modulus, G (kPa)	1.67×10^7	2.8×10^7	1.67×10^7	1.67×10^7	2.8×10^7	1.67×10^7	1.67×10^7
Fractured Strength constant, B	1.6	0.7	1.1	1.6	0.7	0.35	0.9
Fractured Strength Exponent, M	0.61	0.8	0.9	0.61	0.8	0.55	0.9
Damage Constant, D_1	0.04	0.015	0.02	0.04	0.015	0.08	0.02

Minimum Strain to Failure e_{min}^{fail}	0.01	8×10^{-4}	0.001	0.01	8×10^{-4}	0.03	0.002
Tensile Failure	Hydro (Pmin)	Hydro (Pmin)	Principal stress	Principal stress	Hydro (Pmin)	Hydro (Pmin)	Hydro (Pmin)
Tensile Failure Stress (kPa)	-----	-----	4×10^3	3.5×10^3	-----	-----	-----
Fracture Energy (j/m²)	-----	-----	80	120	-----	-----	-----
Crack Softening	-----	-----	yes	yes	-----	-----	-----



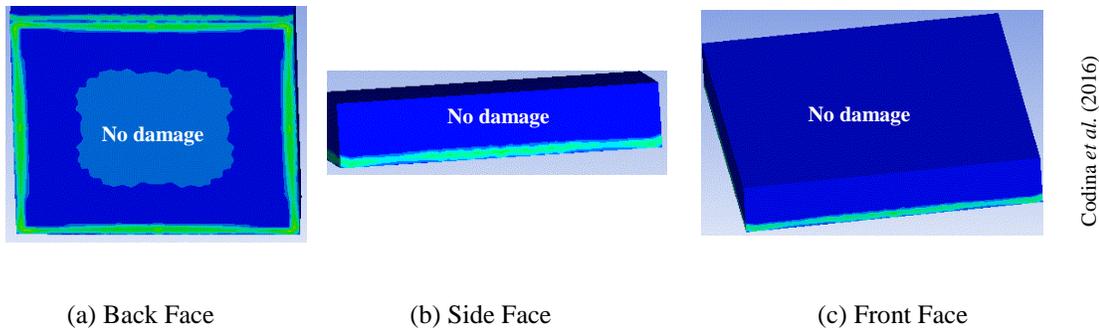


Figure 4.14 Experimental and numerical damage pattern and crack trajectory observations on the PC panel

4.6 Summary

Concrete structures are one of the most used structural material for blast resistant design. Due to the heterogeneity nature of the concrete material, it is difficult to simulate the behavior and crack trajectory of the concrete structure under blast loads. In the past, multiple modified RHT models have been proposed. These models have been well calibrated to various concrete structures subjected to different loading and boundary conditions. In this Chapter, a new set of RHT parameter was proposed to simulate the simply supported PC panel under different loading conditions. The result shows that the newly proposed RHT model can improve the strain softening behavior of the stress-strain curves under three different loading patterns for compression and tension cases and accurately simulate the failure mode and crack trajectory when subjected to free air blast load, based on the experimental results. As for the previously defined RHT models, the result shows that the aforementioned proposed RHT models cannot accurately model the nonlinear behavior of simply supported PC panel under free blast load. In contrast, the newly proposed set of RHT parameters can be used to accurately simulate the damage pattern and the crack trajectory of simply supported PC panel subjected to free air blast loads.

Chapter 5: Numerical investigation of the performance of the RHR under free air blast load

In this Chapter, a detailed 3D nonlinear numerical analysis is proposed using the nonlinear finite element software, AUTODYN. The modified RHT concrete model, which is proposed in the previous Chapter, is used to accurately simulate the behavior of concrete material under free blast loads. The proposed finite element model of the blast load, which presented in Chapter 4, is used. The accuracy of the blast load and RHR Sandwich panel modeling are validated using available experimental results, which are presented in Chapter 3.

5.1 Literature review

Underground structure is one of the most critical infrastructures for military operations. These structures are expensive to build and require robust protective layers to resist repeated blast loads. In the literature, protective layers are used as sacrificial components, which need to be replaced after strong blast load (Mazek, 2014; Mazek and Mostafa, 2013; Nurick et al., 2009; Rashad, 2013; Vinson, 2001; Wahab and Mazek, 2016; Xia et al., 2016; Zhu, 2008). A sand layer is a common protective layer used for covering the underground structures. It has some disadvantages: 1) it is very heavy, which adds significant loads to the underground structure. This makes the design of the underground structure uneconomical; 2) The sand layer cannot withstand repeated blast loads, after the first impact, the sand will be compacted and the entire protective layers will need to be replaced and; 3) It is difficult and expensive to control the sand density due to the self compaction and water drainage issues (TM5-1300, 1990; UFC 3-340-02, 2008).

To improve the blast resistant performance of the underground military structure, lightweight and high strength blast protective layers are proposed. These lightweight protective layers offer many advantages: including 1) add minimum load to the existing structure; 2) can withstand repeated blast loads and 3) can be replaced easily. One of such innovative lightweight protective layers is the RHR sandwich panel. RHR has a high strength to weight ratio and high energy dissipation capacity under large and repeated blast loads. RHR sandwich panel can be economically constructed and efficiently repaired after a strong blast load without significantly affecting the design of the underground structure.

The idea of the RHR sandwich panel was first introduced by Rashad, (2013), where a numerical study was conducted to examine the blast resistant response of the RHR sandwich panel. The concept of RHR was further used by Wahab and Mazek (2016), where experimental and numerical studies were presented. In these previous studies, the concrete panels were modeled using solid elements and the helical springs were modeled using shell elements, as shown in Figure 5.1(a). The shortcoming of those previous studies is that the approach of using shell elements for helical springs cannot accurately simulate the physical behavior of the helical springs. The reason is that the shell elements cannot accurately simulate the physical interaction between two successive spring coils and between the spring seats and the adjacent face of the panel during large blast loads. In addition, the use of the shell element will automatically assume the element has a virtual rectangular thickness, which cannot accurately simulate the stress distribution of the circular wire. It is found that these factors have significant effects on the numerical results of the proposed sandwich panel.

In this study, a modified solid element model is proposed for the helical spring, as shown in Figure 5.1(b). A detailed numerical study is conducted to effectively examine the performance of the RHR sandwich under free air blast loads using this developed finite element model. The results are verified using available experimental data conducted by the fortification team in the Egyptian army. The results will show the ability of the proposed numerical model to simulate the blast resistant behavior of the RHR sandwich panel under free air blast load. In addition, the simulation results will evaluate the RHR sandwich panel as an efficient protective layer against significant and repeated cycles of explosion loads.

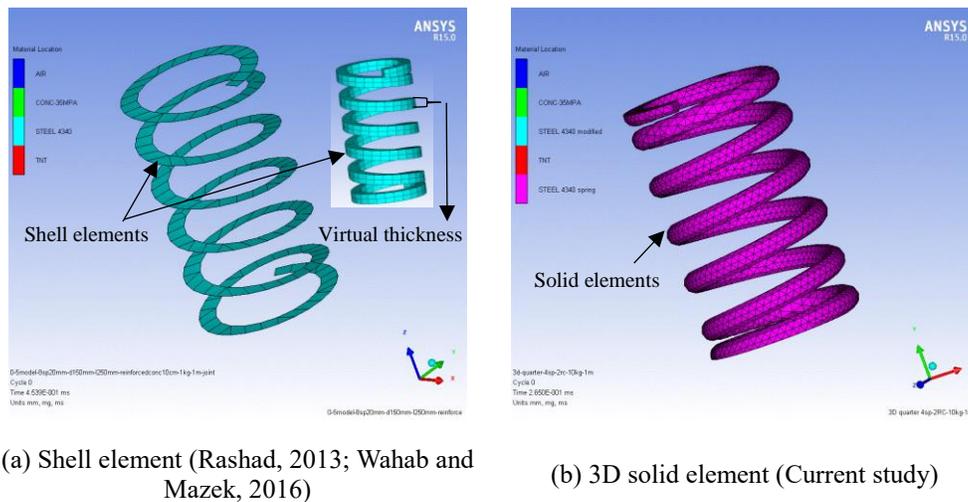


Figure 5.1 Helical spring modeling methods

5.2 Material modeling of the RHR sandwich panel

The RHR sandwich panel, as shown in Figure 5.2, consists of two facing RC panels and a number of compression helical springs, as an interlayer. In this section, the modeling of each component of the RHR sandwich panel is validated individually before applying the numerical study on the entire sandwich panel.

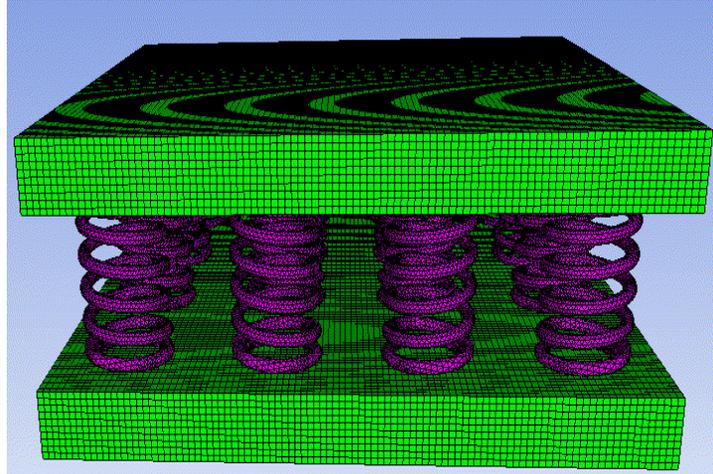


Figure 5.2 A FE model of the RHR sandwich panel with 16 helical springs

5.2.1 RC panels modeling

In this study, concrete is modeled using both the porosity EOS and the polynomial solid EOS, which can simulate the thermodynamic and the compaction behavior of concrete material at different levels of pressure (Herrmann, 1969). RHT model is used as the concrete strength model. Due to the limitation of the default RHT model in simulating the proper dynamic behavior of concrete, a proposed modified RHT model is used to simulate the concrete dynamic behavior better, as discussed before in Chapter 4.

5.2.2 Helical spring and rebar modeling

Due to the difficulty of direct simulating of irregular geometry such as helical springs in AUTODYN, a comparative study is applied to select a proper modeling approach to accurately simulate helical spring's behavior against blast load, considering the interaction between its coils and that between the seats and adjacent surfaces.

There are different ways to model helical springs, i.e., 2D beam elements with a virtual helical path (available in AUTODYN), 3D shell elements on a helical path, 3D beam elements on a helical path and 3D solid elements on a helical path. Figure 5.3 shows the different modeling approaches for the helical spring. After a detailed parametric study, it is found that the 3D solid element model gives more realistic behavior than the beam element, shell element modeling and the 2D beam element, respectively.

In the case of using shell element, it is found that the virtual cross-section of the numerical spring wire is not circular as in reality. In addition, the interaction and the stress distribution between the successive coils and that between the seats and the adjacent surfaces are not accurately simulated. Accordingly, the shell element gives undesirable behavior of the helical spring.

3D beam element modeling can be used for obtaining preliminary results that are limited to the displacements and the forces occur in the axial direction of the beam element, ignoring the cross section and the lateral stress distribution on the wire (Prawoto et al., 2008; Shimozaki, 1997). Besides, the realistic behavior between the seats and the adjacent surfaces and that between the successive coils cannot be monitored accurately.

As for the 2D beam element, which is the only one implemented directly in AUTODYN to simulate the helical spring, it is found that it gives unrealistic behavior of the helical spring as it considers the helical spring as a 2D beam element with a virtual helical path. Accordingly, this modeling approach considers only the stiffness of the spring and ignore the helical geometry. Accordingly, stress distribution and interaction of the spring coils cannot be obtained.

In this study, helical springs are modeled using 3D solid element, as shown in Figure 5.3(d), to study the actual behavior of the spring coils. The entire geometry of the helical spring is created in the Inventor program (Autodesk Inventor, 2010) then imported to the ANSYS workbench (ANSYS, 2007) for the meshing process and then finally imported to AUTODYN program as a 3D solid part. The only disadvantage of the 3D solid element is the long computation time needed due to the size and the number of elements. The rebar is modeled by using beam elements. For the helical springs and the rebar, the steel elastic response range is modeled using a linear EOS, as expressed in equation 5.1. This EOS is selected due to the approximated proportional relationship between steel compression and pressure level. The steel plastic behavior is modeled using the Johnson and Cook strength model (Johnson and Cook, 1983), as presented in equation 5.2. Johnson and Cook strength model is a strain rate dependent model, which is useful for modeling the strength response of steel subjected to large deformation, high strain rates, and high temperature. Table 5.1 shows the properties of steel, which are used for modeling helical springs and rebar in this research, respectively (ANSYS-AUTODYN, 2005).

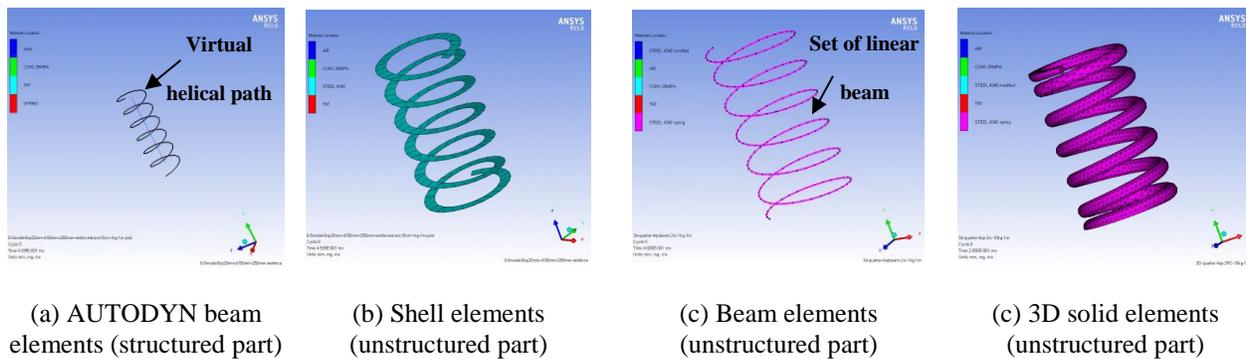


Figure 5.3 Kinds of helical spring simulation

$$P = K \mu \quad (5.1)$$

$$Y = [A + B\varepsilon_p^n][1 + C \ln \dot{\varepsilon}_p][1 - T_H^w] \quad (5.2)$$

Where P is the pressure; K is the bulk modulus of the steel material; $\mu = (\rho/\rho_0 - 1)$ is the compression ratio; ρ_0 is the initial material density; Y is the yield strength; A is the yield stress at low strains; B is the strain hardening constant; ε_p is the effective plastic strain; n is the strain hardening exponent; C is the strain rate constant; $\dot{\varepsilon}_p$ is the normalized effective plastic strain rate; T_H is the homologous temperature given by $T_H = (T - T_{room})/(T_{melt} - T_{room})$; w is the thermal softening exponent.

For equation 5.2, the first set of brackets gives the yield stress as a function of strain at room temperature and a strain rate of 1 s^{-1} , which is the default reference strain rate, accounting for the effect of strain hardening. The second set of brackets modifies the yield stress based on the strain rate. The third bracket accounts for thermal softening, which causes the yield stress to become zero when the temperature reaches the melting point.

Table 5.1 Material data of helical springs and rebar used in this research (ANSYS-AUTODYN, 2005)

Equation of state	Linear	Strain rate constant (c)	0.014 / 0.022
Reference Density (g/cm ³)	7.83	Thermal softening exponent	1.03 / 1.00
Bulk modulus (kPa)	1.59×10^8	Melting temperature (k)	$1.793 \times 10^3 / 1.811 \times 10^3$
Reference temperature (k)	300	Ref. strain rate (/s)	1
Specific heat (J/kgK)	477	Failure	Johnson Cook / None
Strength	Johnson Cook	Damage constant D ₁	0.05
Shear modulus (kPa)	8.18×10^7	Damage constant D ₂	3.44
Yield stress (kPa)	7.92×10^5 / 3.5×10^5	Damage constant D ₃	-2.12
Hardening constant (kPa)	5.10×10^5 / 2.75×10^5	Damage constant D ₄	0.002
Hardening exponent	0.26 / 0.36	Damage constant D ₅	0.61

5.3 Mesh sensitivity analysis

One of the most critical factors, which affect the accuracy and convergence of the numerical modeling, is selecting a proper element size. Accordingly, in this study, a detailed mesh sensitivity

analysis is conducted on the components of the RHR sandwich panel to evaluate the accuracy and reliability of the numerical simulation.

5.3.1 Air block

For the 2D explosion modeling, it is found that using an element size of 1 mm is adequate to simulate the 1 Kg TNT denotation at a SoD of 1 m, and 2mm for the 5 Kg and 10 Kg TNT denotation at a SoD of 1 m. The results give accurate maximum peak overpressure values when compared with the calculated results from CONWEP software with accepted errors of 3.4 %, 5.4 %, and 5.9 %, respectively.

For the 3D explosion modeling, mesh sizes of 1, 2, 4, 6, 8, 10, 15 and 20 mm are studied and evaluated. It is found that element size with thickness less than 10 mm usually creates too much computational time and memory allocation error (ANSYS-AUTODYN, 2009). For element sizes of 10 mm, the peak overpressure values for 1, 5 and 10 Kg TNT agree well with that calculated from CONWEP with accepted errors of 8.8 %, 2.7 %, and 5.6 %, respectively. Figure 5.4 shows a comparison of the pear overpressure values calculated from the CONWEP and that simulated with the proposed mesh sizes in the 2D model and the 3D model.

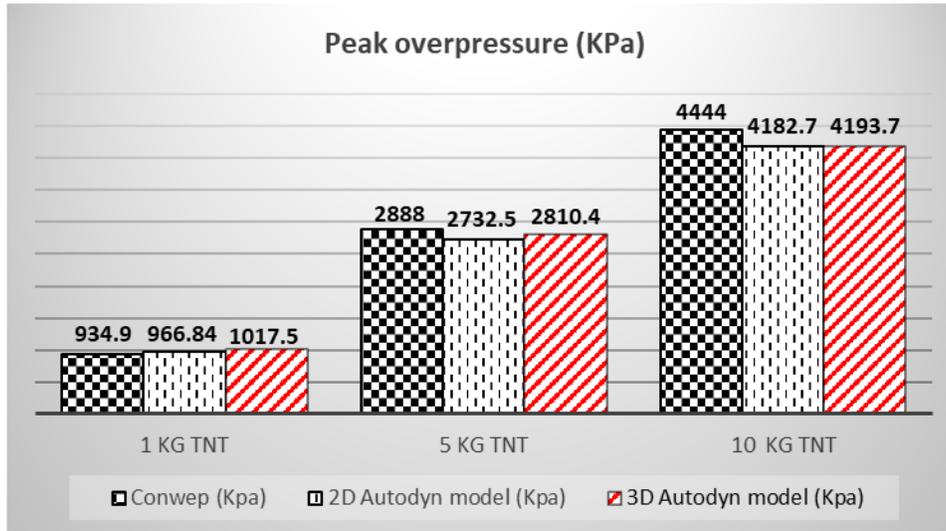


Figure 5.4 Comparison of peak overpressure values

In addition, the peak overpressure values for 1, 5 and 10 Kg TNT using the nominated element size of 10 mm agree well with that recorded in the field tests with accepted errors of 2.7 %, 1.8 %, and 2.3 %, respectively. Figures 5.5, 5.6 and 5.7 show the mesh sensitivity analysis applied on the three different blast loads. The red dash line refers to the field reading of the peak overpressure for each blast load. Good conformity is observed between the recorded peak overpressure and that obtained from the numerical simulation using the nominated element size, for the three different blast loads. Accordingly, the 10 mm mesh size is used for the 3D air block modeling. Using a mesh size of 10 mm creates more than 2.5 million elements to simulate the physical blast load observed in the experimental tests.

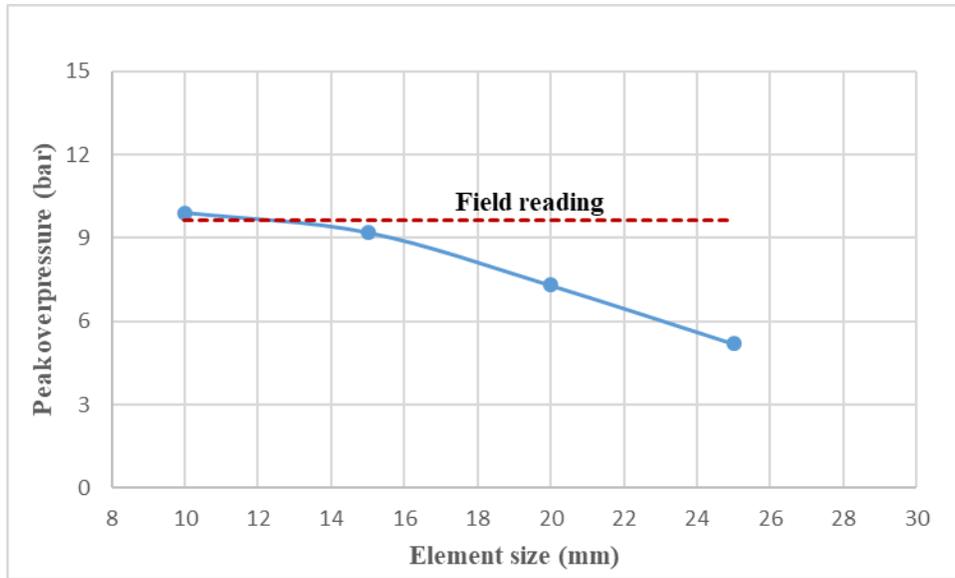


Figure 5.5 Effect of changing the element size on the peak overpressure value for detonating 1 Kg TNT at a SoD of 1 m

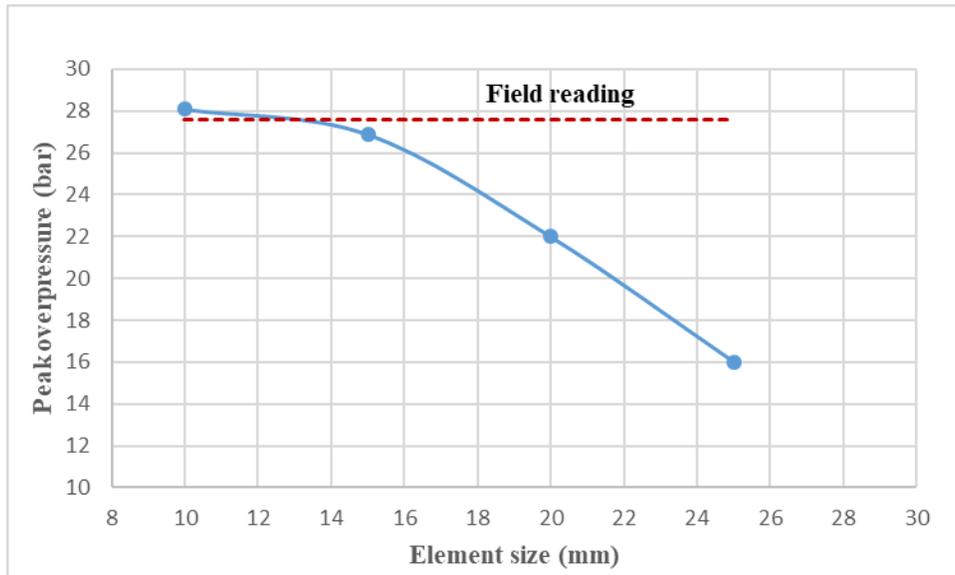


Figure 5.6 Effect of changing the element size on the peak overpressure value for detonating 5 Kg TNT at a SoD of 1 m

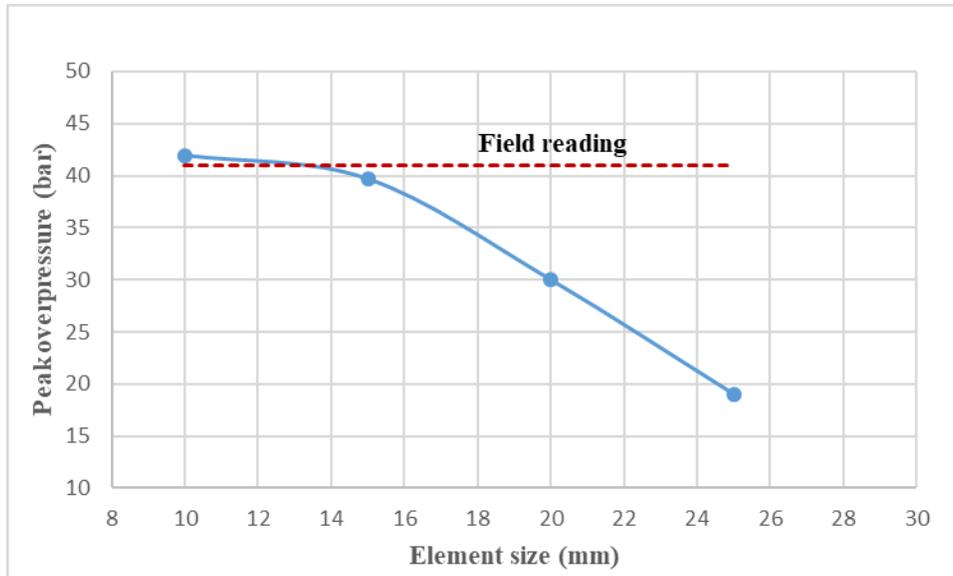


Figure 5.7 Effect of changing the element size on the peak overpressure value for detonating 10 Kg TNT at a SoD of 1 m

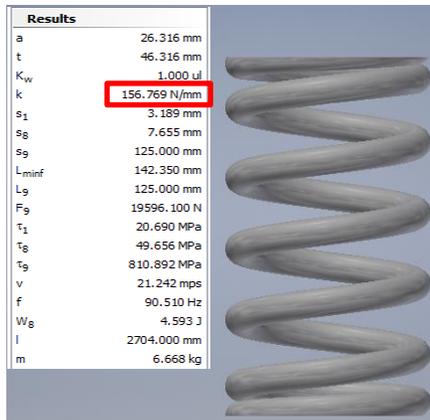
5.3.2 RC panels

As discussed before in the previous Chapter, an element size of 10 mm is adopted for the concrete panel to be consistent with the air block. It is noted that the mesh size of 10 mm has enough accuracy for similar problems (Codina et al., 2016; Li et al., 2016; Luccioni B, Araoz G, 2013). In addition, the element size of the donor boundary environment (i.e. applied load) should be equal or smaller than that of the acceptor body (i.e. RC panel) to obtain an accurate performance (AUTODYN 2005). Accordingly, 25,000 elements are used to model the RC panel. A suitable number of beam elements is chosen for each rebar to be consistent with the RC panel nodes and to ensure that each steel bar has sufficient connected nodes with the adjacent nodes of the concrete panel.

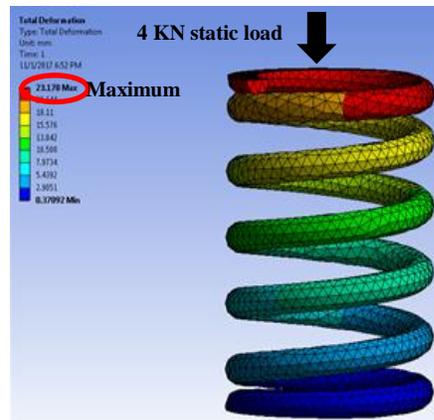
5.3.3 Helical springs

Two static analyses are conducted to calculate the numerical helical spring stiffness and compare it with that measured from the compression machine test in the factory. The first static analysis is performed using the Inventor program, as shown in Figure 5.8(a). The result shows that the spring stiffness obtained from the static analysis, which is equal to 157 N/mm, agrees well with that measured in the factory, which is equal to 161 N/mm, with an acceptable error of 2.6 %. The second static analysis is created on the Ansys workbench, as shown in Figure 5.8(b). Some trials are applied using different element sizes until reaching good conformity between the factory stiffness and the numerical stiffness, which is equal to 173 N/mm, with an acceptable error of 6.7 %.

Figure 5.9 shows the mesh sensitivity analysis conducted on the helical spring. Decreasing the element size more than the chosen value leads to an increase in the computational time needed. Table 5.2 shows the error percentage between the helical spring stiffness measured in the factory and that obtained from the inventor and Ansys workbench static analyses. The number of elements used to model the helical springs in this study is 16,645 solid elements. The result shows that such a mesh size can simulate the behavior of the helical spring accurately.



(a) Inventor program



(b) Ansys workbench

Figure 5.8 Helical spring stiffness obtained from the static numerical analyses

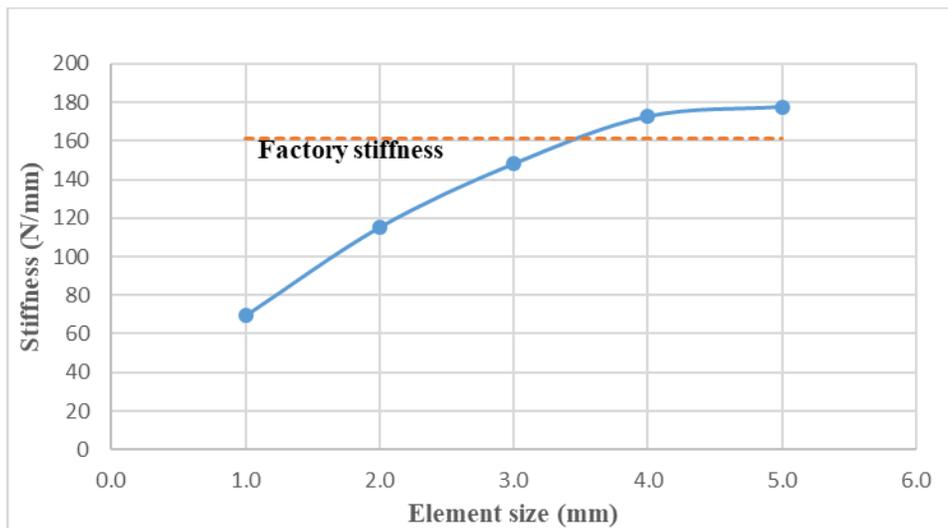


Figure 5.9 Helical spring stiffness for different element sizes

Table 5.2 The difference between the helical spring stiffness measured in the factory and that obtained from static analyses

Name of the test	Factory compression test	Inventor static analysis	Ansys static analysis
Helical spring stiffness (N/mm)	161	157	173
Error (%)	0	2.6	6.7

5.3.4 Rebar

For rebar modeling, beam elements are used to model rebar, as mentioned above. Each steel bar consists of a number of beam elements. Each beam element should be not less than double the diameter of the steel bar to avoid small aspect ratio error (ANSYS-AUTODYN, 2005). In this study, the diameter of the steel bars is 8 mm thus an element size of 20 mm is chosen which is suitable for creating node connections between the concrete and rebar elements and to avoid the small aspect ratio error. The number of beam elements for each steel bar is 72 elements.

5.4 Numerical study of the RHR sandwich panels

After validation of each component of the studied sandwich panel and the explosion process modeling, the same modeling approach is then used to model the response of the entire proposed RHR sandwich panel. Consistent boundary conditions are applied to simulate a similar environment as in the arena test. In this numerical study, full numerical models are created to investigate the accurate performance of the RHR sandwich panel. Fully coupled Euler Lagrange interaction is adapted between the blast environment and specimen. Trajectory interaction is adapted between the RC panels and the helical springs. This interaction is used for unstructured parts (which are created outside the AUTODYN program) considering no external gap size between the Lagrange bodies even if the facing nodes of the adjacent bodies do not coincide. Fixed and movable gauges are created at different locations to record the pressure time histories, displacement time histories and internal energy time histories. Note that the displacement time histories and energy time histories are monitored until reaching the maximum displacement value of the front RC panel.

In this study, the behavior of the RHR sandwich panel with sixteen helical springs is studied under three different scaled distance. The numerical results are compared with the corresponding experimental results. In this research, the first peak of the displacement time history is studied. The damping effect is neglected as it has no considerable effect on the first peak of the displacement time history (Hao et al., 1998; Wu et al., 1999). Besides, the damage level for each component is observed to investigate the capability of the proposed sandwich panel in protecting the back panel from being damaged. In addition, energy analysis is applied to evaluate the total energy dissipated by each component of the RHR sandwich panel. Figure 5.10 shows the description and boundary conditions of a quarter model of the RHR sandwich panel.

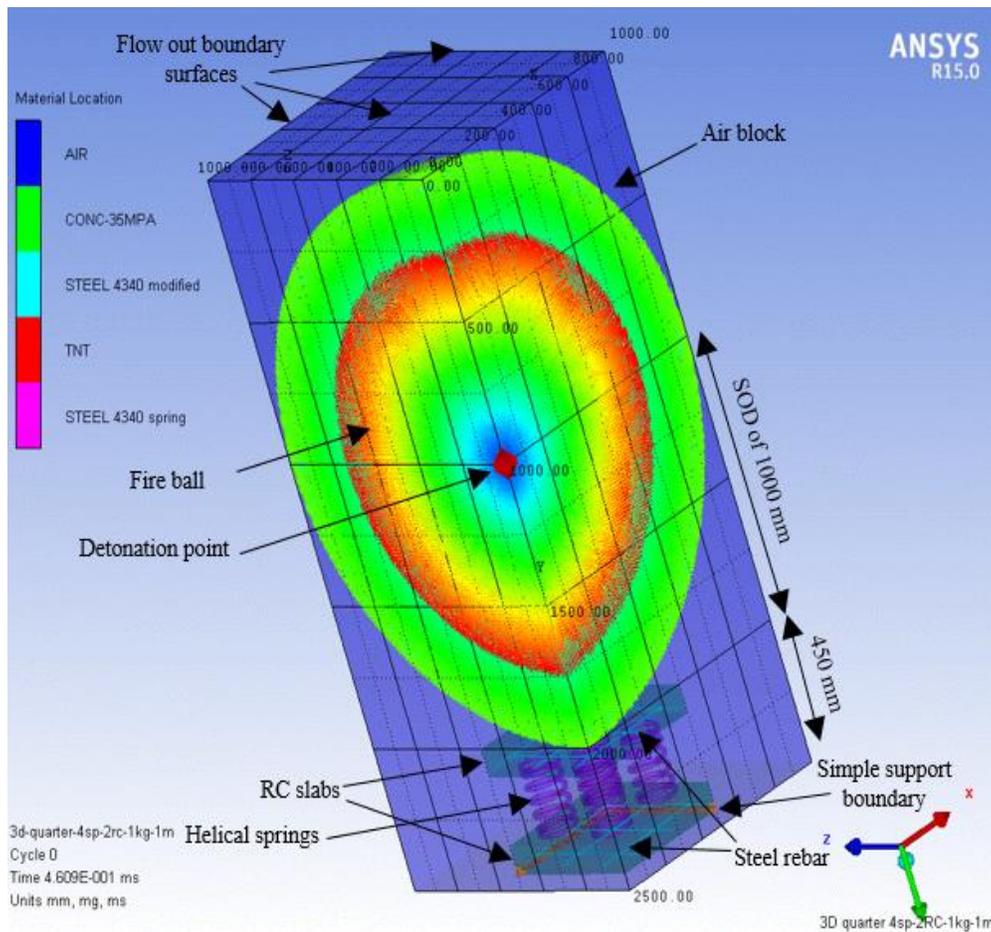


Figure 5.10 A quarter model of RHR sandwich panel

5.5 Discussion of the results

Figure 5.11 shows a comparison of the peak overpressure values at three different locations for the three levels of blast loads. The results show that there are considerable reductions between the peak overpressure values at the front face of the front RC panel, midpoint of the RHR sandwich panel and back face of the back RC panel under the three different blast loads. The reduction percentages between the first and last values for 1, 5 and 10 Kg TNT detonated at a SoD of 1 m are 93 %, 96 %, and 97 %, respectively. These results indicate an excellent capability of the RHR sandwich panel of attenuating the effective pressure applied on the sandwich panel.

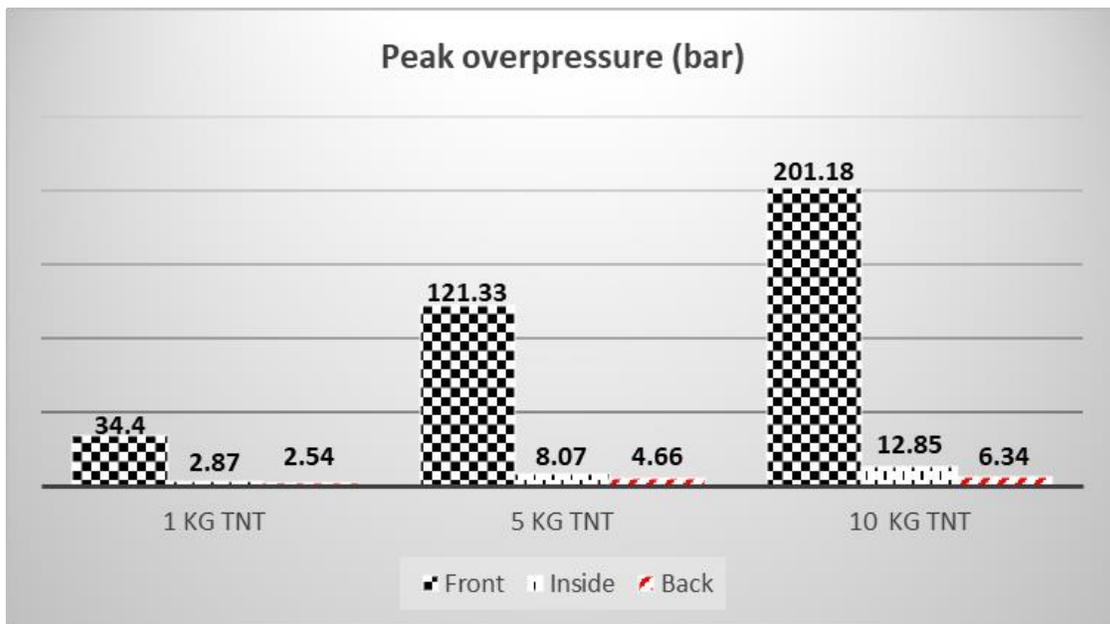


Figure 5.11 Comparison of peak overpressure values at the front face of the front RC panel, midpoint of the RHR sandwich panel and back face of the back RC panel

The main target of these studies is to protect the back RC panel (i.e., the main body of the underground structure) from being damaged. In order to achieve this goal, the displacement time histories and the damage level of the proposed sandwich panel components are analyzed. Figure

5.12 shows a comparison between the maximum displacement of the front RC panel measured from the field tests and that obtained from the numerical analysis under the three different blast loads. The result shows an excellent matching between the experimental and numerical simulations, where the errors are 15.8 % and 2.8 % for 1 and 5 Kg TNT detonated at a SoD of 1 m, respectively. For the case of 10 Kg TNT, the front RC panel is totally damaged and fragmented into pieces in the field tests and numerical analysis. No considerable displacements are observed for the back panel in the three blast load cases.

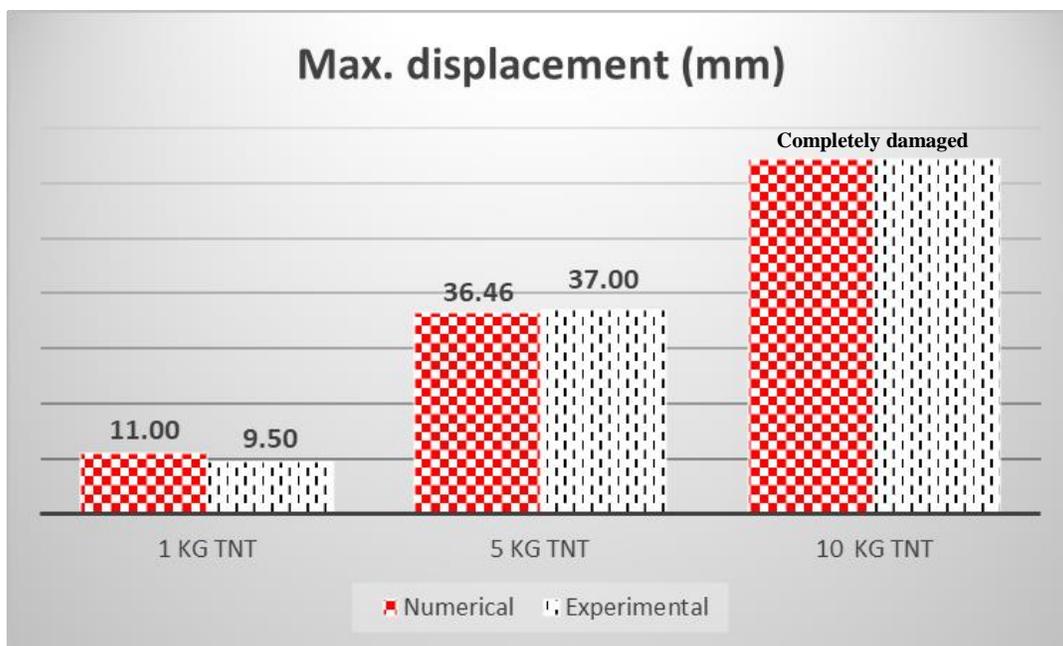
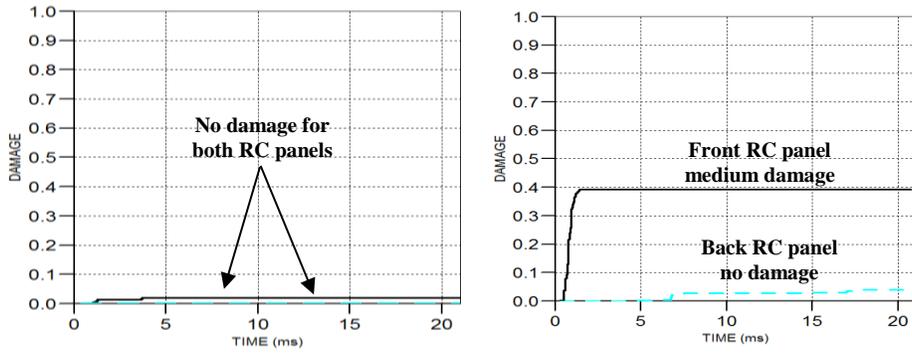


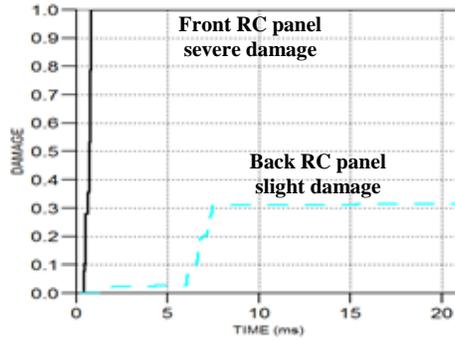
Figure 5.12 Comparison between the maximum displacements of the front RC panel obtained from the numerical analysis and that measured in the field

For damage prediction analysis, Figure 5.13 shows the damage contours of the front and back RC panels under the different blast loads. The damage level (DL) is a unitless scale for the damage that occurred and it can be categorized into four levels as described in Chapter 4.



(a) 1 Kg TNT

(b) 5 Kg TNT



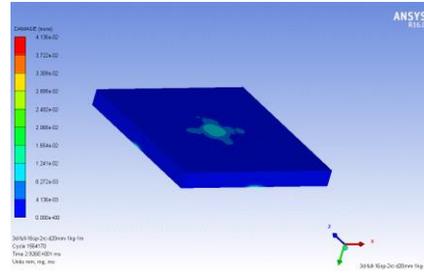
(c) 10 Kg TNT

Figure 5.14 Damage level-time histories at the midpoint of the front and back RC panels of the RHR sandwich panel under different free air blast loads

By visually comparing the numerical damage pattern of the RC panels with that observed in the field tests, it can be observed that there is good conformity between the observed crack trajectories and the damage pattern and simulated results under the three different blast loads. Figure 5.15 shows a comparison between the experimental and numerical crack trajectories for the front RC panel of the RHR sandwich panel under the three different blast loads.



No cracks

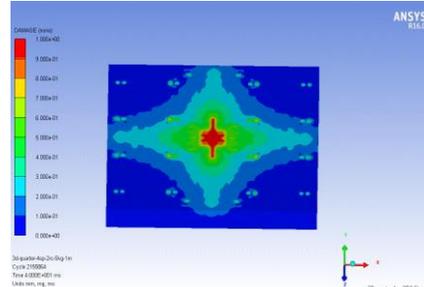


No damage

Under 1 Kg TNT



Diagonal cracks

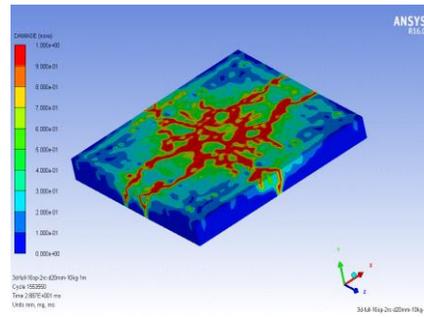


Diagonal damage pattern

Under 5 Kg TNT



Fully damaged and fragmented into pieces



Fully damaged

Under 10 Kg TNT

Figure 5.15 Experimental and numerical damage observation of the front RC panel of the RHR sandwich panel under three different blast loads of 1, 5 and 10 Kg TNT at a SoD of 1 m

In this study, the applied explosion energy is dissipated by two main mechanisms. First, the applied energy is reflected by the front face of the front RC panel. Second, the front RC panel and helical springs absorb a considerable portion of the applied energy in the form of internal and kinetic energy. The function of the helical springs interlayer is to absorb a portion of the applied blast

energy by applying a compression movement. Accordingly, extension forces are induced and act mostly upward, which consequently extrudes the front RC panel to its original position after doing some oscillation. This vibration diminishing is occurred due to the natural damping of the compression helical springs and its natural self-restoring (UFC 3-340-02, 2008).

Internal energy is one of the best evaluations for each component of the proposed sandwich panel. The goal of the proposed RHR sandwich panel is to minimize the total energy absorbed by the back panel (i.e., the main structure body). Figure 5.16 shows the internal energy time histories experienced by the front RC panel and back RC panel under the three different blast loads. Figure 5.17 shows the internal energy time history of the helical springs interlayer under the three different blast loads.

Figure 5.16 shows that the front and back RC panels tend to have permanent plastic energy dissipation. The result shows that the maximum plastic internal energy absorbed by the back RC panel for the three different blast loads of 1, 5 and 10 Kg TNT is 37.5 %, 20 % and 40 %, respectively, of that absorbed by the front RC panel. In contrast, the internal energy stored by the helical spring is released after experiencing the maximum displacement. Besides, the maximum energy absorbed by the front RC panel for the three different blast loads of 1, 5 and 10 Kg TNT is 10.5 %, 13% and 11 %, respectively, of the maximum internal energy stored in the helical springs interlayer. These results show the significant role of the helical springs interlayer in storing a considerable portion of the applied energy as elastic internal energy in which the helical spring released it back and accordingly, reduces the energy transmitted to the back RC panel. These

results indicate that the first two layers work in harmony to significantly reduce the imparted energy to the back panel.

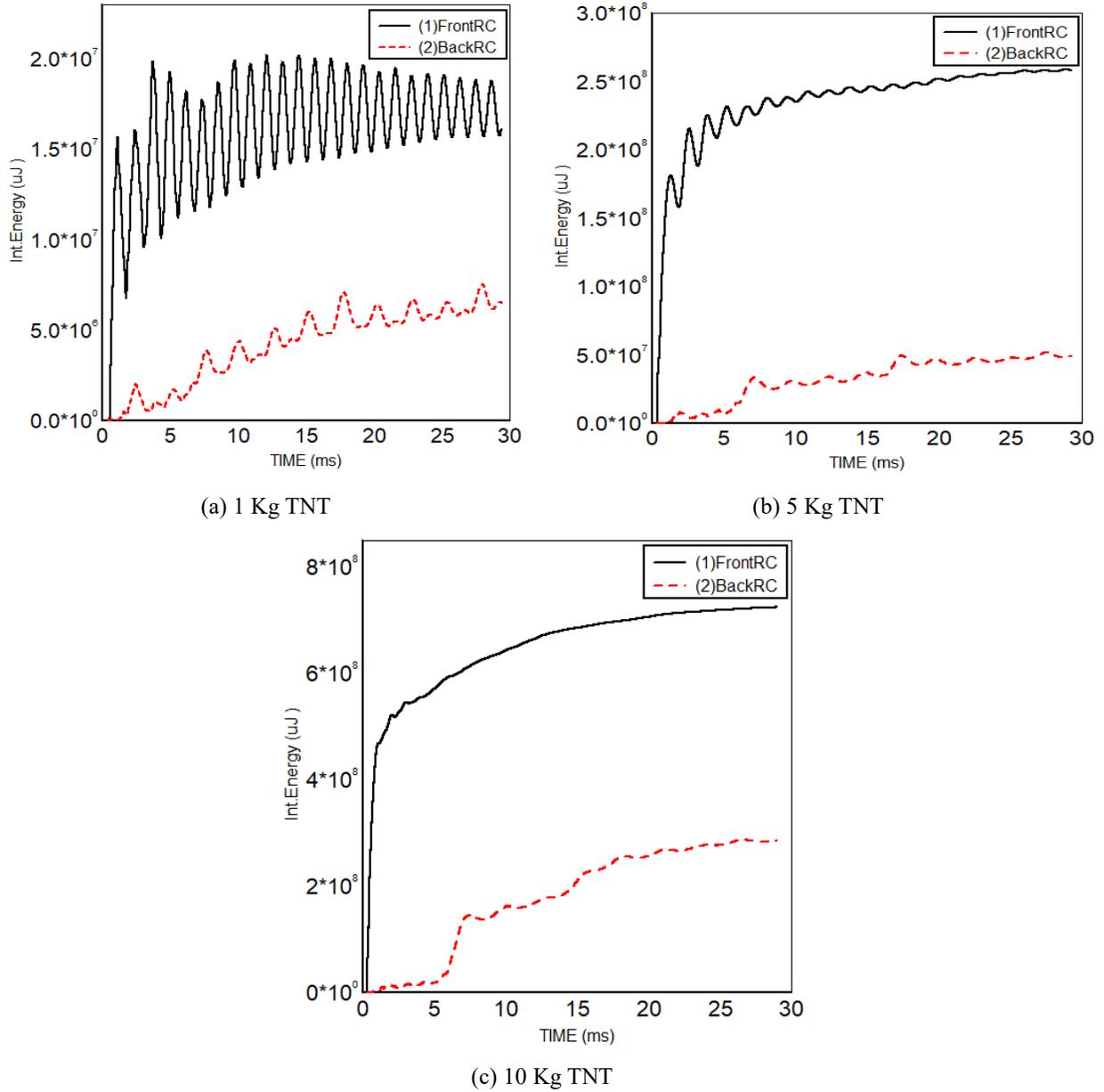


Figure 5.16 Internal energy time histories of the front and back RC panel under the three blast loads

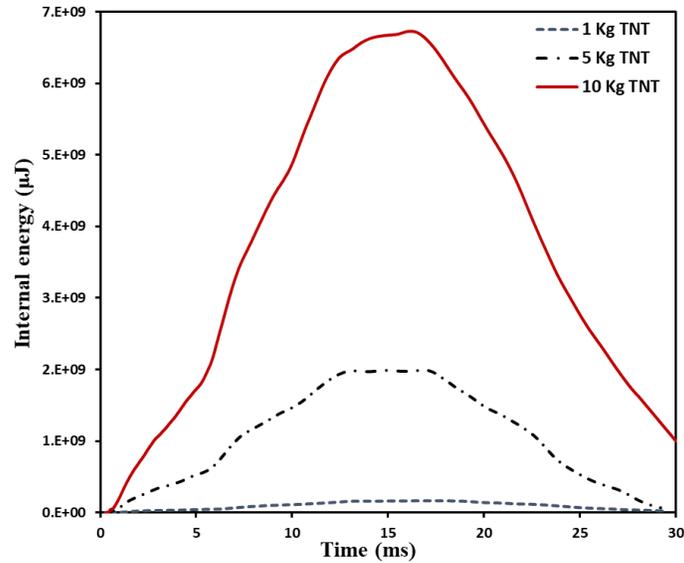
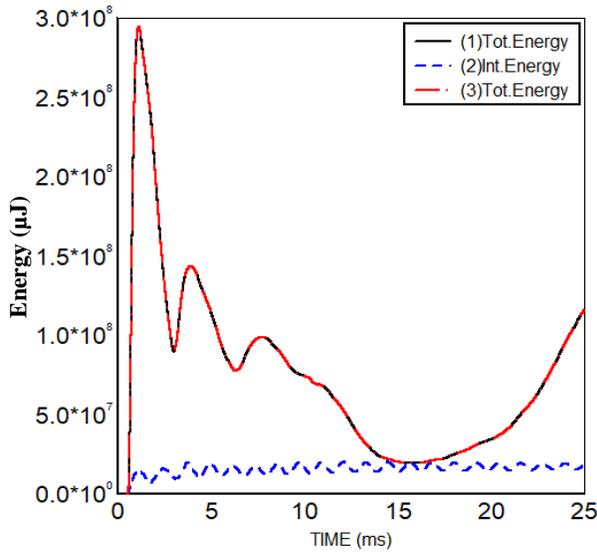


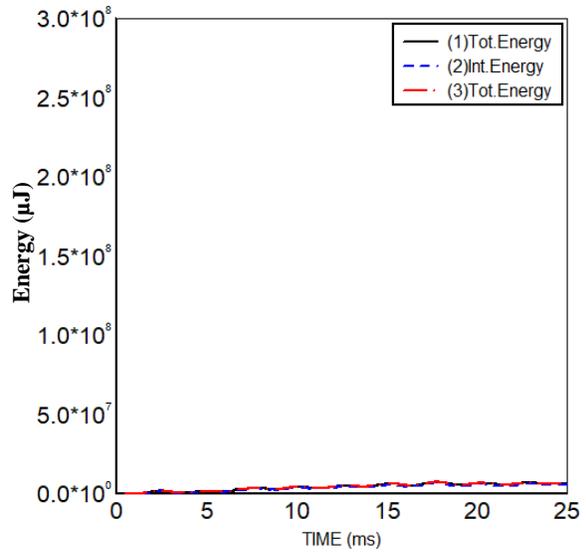
Figure 5.17 Internal energy time histories of the helical springs interlayer under the three blast loads

Figures 5.18, 5.19 and 5.20 show the total energy, internal energy and kinetic energy time histories for the three main components of the RHR sandwich panel under the three blast loads of 1, 5 and 10 Kg TNT at a SoD of 1 m, respectively. In this study, the total energy is the summation of internal energy and kinetic energy. It should be noted that due to the existence of the flexible supports (i.e., helical springs interlayer), the front RC panel dissipates a considerable amount of the applied blast energy in the form of kinetic energy as shown in Figures 5.18(a), 5.19(a) and 5.20(a). The kinetic energy absorbed by the front RC panel is higher than that absorbed by the helical springs, as shown in Figures 5.18(a and c), 5.19(a and c) and 5.20(a and c). In contrast, the internal energy stored by helical springs is higher than that stored by the front RC panels due to the resilience of the helical springs. As a result of the considerable amount of the applied energy dissipated by the front RC panel and the helical springs interlayer, the remaining energy imparted to the back RC panel is small and relatively absorbed in the form of internal energy, as shown in Figures 5.18(b), 5.19(b) and 5.20(b).

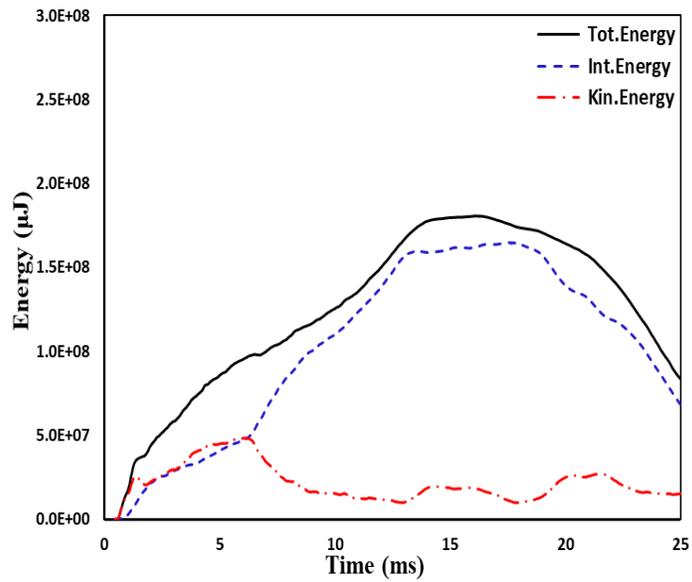
In general, the existence of helical springs interlayer has considerable influence on enforcing the front RC panel to absorb a considerable portion of the applied energy in the form of kinetic energy and a small portion as internal energy. This performance leads to postpone the full failure of the front RC panel and raise the value of the failure load. For helical springs interlayer, most of the imparted energy is dissipated by the helical springs in the form of elastic internal energy, which released after the helical springs interlayer reaches its maximum displacement.



Front RC panel

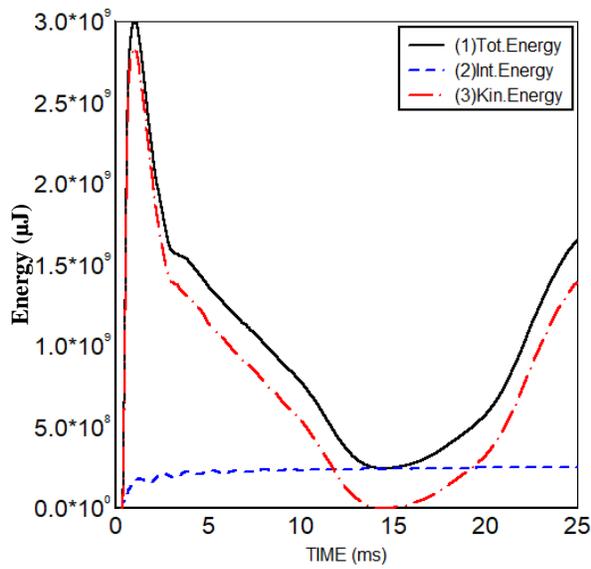


Back RC panel

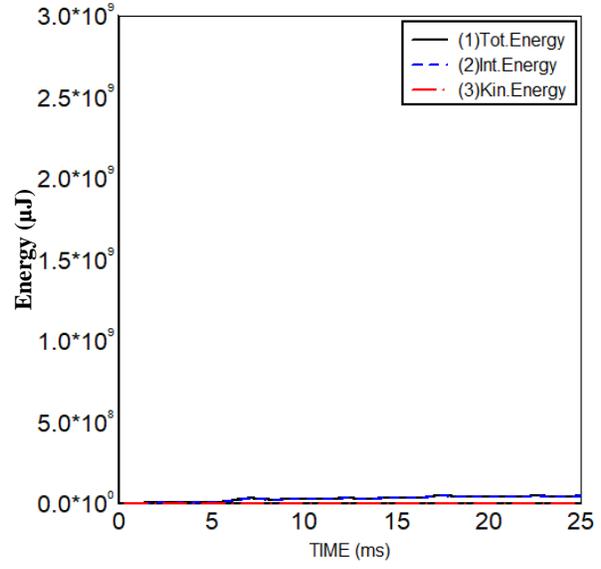


Helical springs interlayer

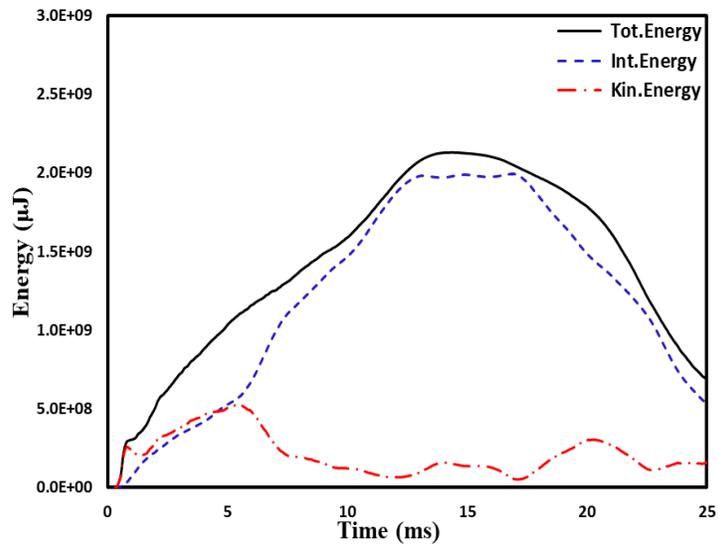
Figure 5.18 Total energy, internal energy and kinetic energy time histories of the front RC panel, helical springs interlayer and back RC panel in the case of 1 Kg TNT at a SoD of 1 m



Front RC panel

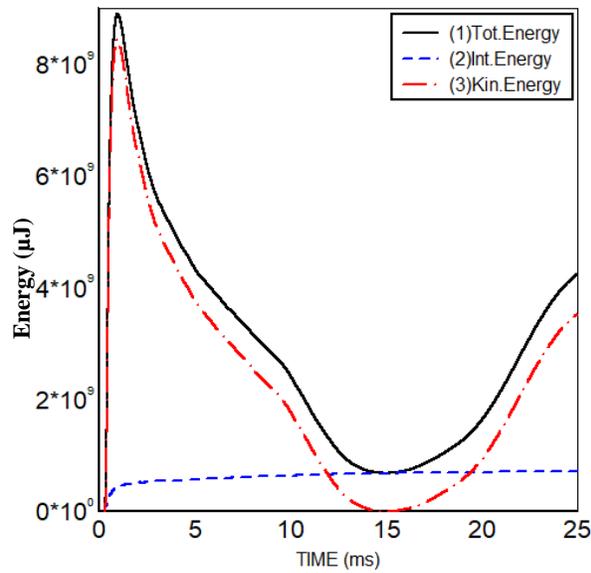


Back RC panel

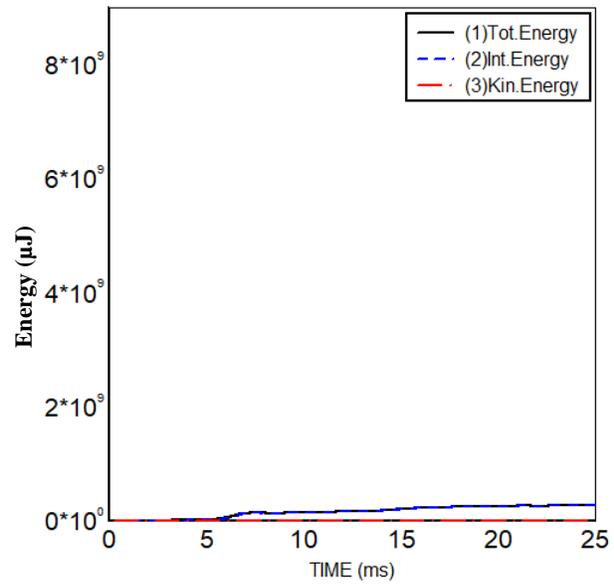


Helical springs interlayer

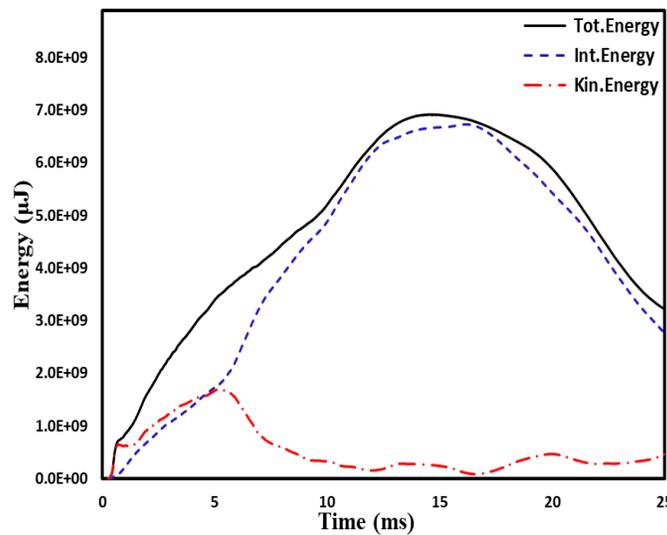
Figure 5.19 Total energy, internal energy and kinetic energy time histories of the front RC panel, helical springs interlayer and back RC panel in the case of 5 Kg TNT at a SoD of 1 m



Front RC panel



Back RC panel



Helical springs interlayer

Figure 5.20 Total energy, internal energy and kinetic energy time histories of the front RC panel, helical springs interlayer and back RC panel in the case of 10 Kg TNT at a SoD of 1 m

The methodology of this behavior can be explained as when the shock wave reached the front RC panel; an instantaneous high velocity is experienced by the front RC panel where most of the applied energy is dissipated into a form of kinetic energy and absorbs a small portion in the form

of internal energy. This is due to the existence of the helical springs layer, which acts as elastic supports to the front RC panel. Therefore, the helical springs layer decreased the amount of internal energy stored by the front RC panel.

On the other side, the second layer (i.e., helical springs interlayer) starts gradually to absorb most of the imparted energy in the form of internal energy and small portion as kinetic energy. Subsequently, the helical spring layer has two tasks to do. Firstly, it will transmit a small portion of energy to the third layer (i.e., the back RC Panel) which accordingly, will be absorbed in the form of internal energy and negligible kinetic energy. Secondly, at the moment of reaching the maximum displacement, the potential energy stored in the helical springs layer will reverse the motion upward to enforce the first layer to return to its original position. This oscillation will be diminished by the natural self-restoring ability of the helical springs (UFC 3-340-02, 2008).

In addition to the energy analysis, the plastic work done by the front and back RC panels under each blast load is analyzed. The results emphasize that the proposed system has a significant influence in attenuating the imparted energy reached the back RC panel. Figure 5.19 shows a bar chart for the maximum plastic work done by each of the front and back RC panels. It is observed that the difference between the maximum plastic work of the front and back RC panels, based on the three blast load cases of 1, 5 and 10 Kg TNT, are 94.6 %, 94.5 % and 61 %, respectively. It should be noticed that in the case of 10Kg TNT, the front RC panel is entirely damaged, which accordingly allows a considerable amount of energy to be imparted to the back RC panel, which leads to increasing the amount of the plastic work done by back RC panel.

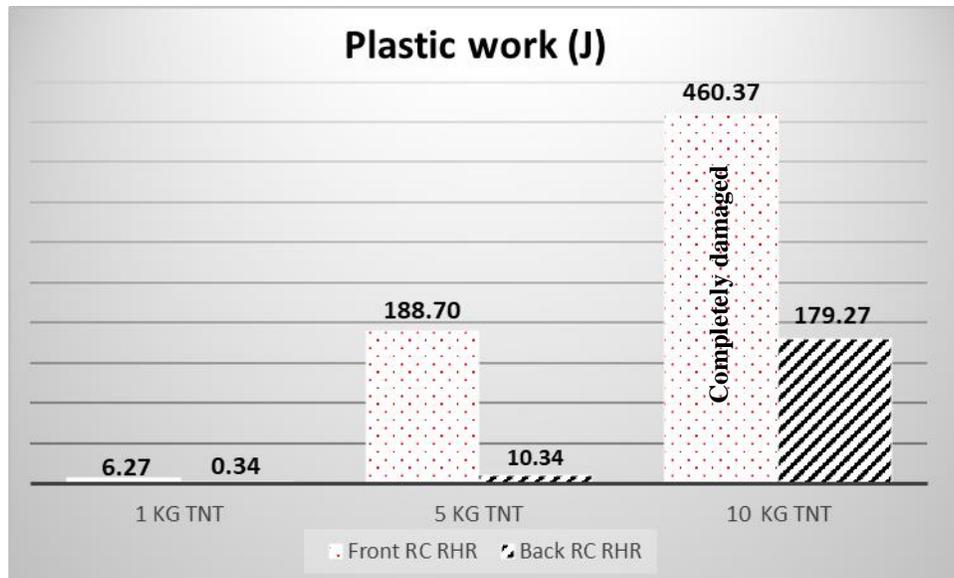
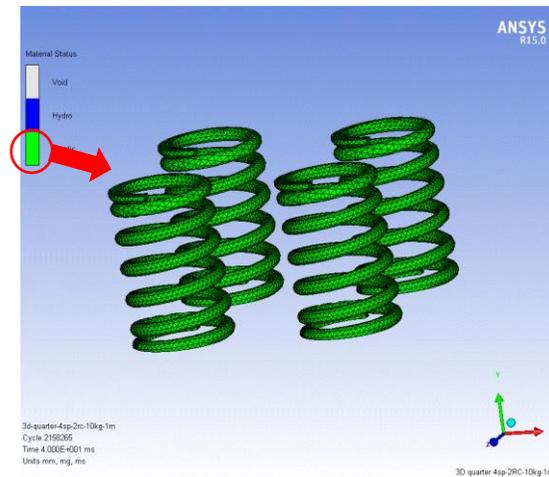
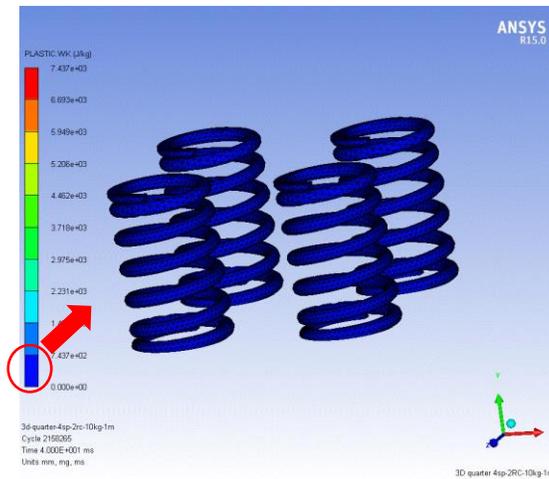


Figure 5.21 Maximum plastic work done for the front and back RC panels under the three blast loads

One of the main advantages of using the RHR sandwich panel is that the helical springs interlayer remains elastic. Hence, the RHR sandwich panel can be used to withstand another blast load, based on the studied range of blast loads up to 10Kg TNT at a standoff distance of 1m. The material status of the helical springs and plastic work done, based on the 10 Kg TNT, are shown in Figures 5.20(a) and (b), respectively. The result shows the helical spring indeed remain elastic under the 10 Kg TNT detonated at a SoD of 1 m.



(a) Material status



(b) Plastic work done

Figure 5.22 The Material status of the helical spring under 10 kg TNT

5.6 Summary

Protective layers are one of the most crucial design components for underground military structures. The new trend of protective layer design focuses on using lightweight materials, which can be used for large and repeated blast loads and can be replaced and repaired efficiently. In this study, a novel protective sandwich panel, named the RHR sandwich panel, is proposed. To properly examine the nonlinear dynamic behavior of the RHR panel, detailed experimental and

numerical studies are conducted. The results show good conformity between the numerical and their corresponding experimental results. In addition, the results show the significant role of the helical springs interlayer in preventing the back RC panel (e.g., main structure) from being damaged. The helical springs interlayer and the front RC panel absorb most of the applied blast energy and impart a negligible portion to the back RC panel. Under the considered scaled distance, the front RC panel and the helical springs interlayer dissipated an average of 98.5 % of the applied blast energy.

Chapter 6: Comparison between the SR, RSR and RHR protective systems

In this Chapter, the novel RHR sandwich panel is evaluated against the traditional SR and RSR protective systems. The RHR sandwich panel is designed to dissipate a large amount of energy during blast loads. After the explosion, the front panel is designed to be replaced efficiently without affecting the helical springs interlayer and back RC panel, which is considered as the roof of a shallow underground structure. To evaluate the performance of the RHR sandwich panel against free blast loads accurately, its performance is compared against the Sand - RC panel (SR) protective system and the RC panel – Sand - RC panel (RSR) sandwich panel. SR protective system is created by replacing the front RC panel and the helical springs interlayer with a dry sand layer. The height of the sand layer is equal to 350 mm, which is the summation of the height of the front RC panel and the helical springs interlayer. In this case, the sand will directly face the blast wave. As for the RSR sandwich panel, it uses the same configuration as the RHR, except the interlayer, in which the helical springs are replaced with normal density dry sand having the same depth.

Detailed 3D finite element models of the RHR, SR and RSR are developed using the software AUTODYN. The behavior of the RHR is verified using available experimental results, while the behavior of the sand layer using in SR and RSR protective system is verified by comparing the numerical blast response of the sand layer with a previous experimental data. A numerical simulation is created for a dry sand layer subjected to blast load and validated using a previous experimental work conducted by Bergeron et al., (1998).

6.1 General

In this Chapter, the performance of the RHR sandwich panel is compared with the SR and RSR protective systems against free air blast loads. In the literature, it is recommended that the thickness of the sand layer should be at least equal to the total thickness of the two RC Panels (TM5-1300, 1990; UFC 3-340-02, 2008; Wu et al., 2004). Accordingly, in this study, the height of the sand layer in the SR and RSR protective systems is 350 mm and 250 mm, respectively, which fulfilled the recommendation mentioned above where the height of the RC panel is 100 mm.

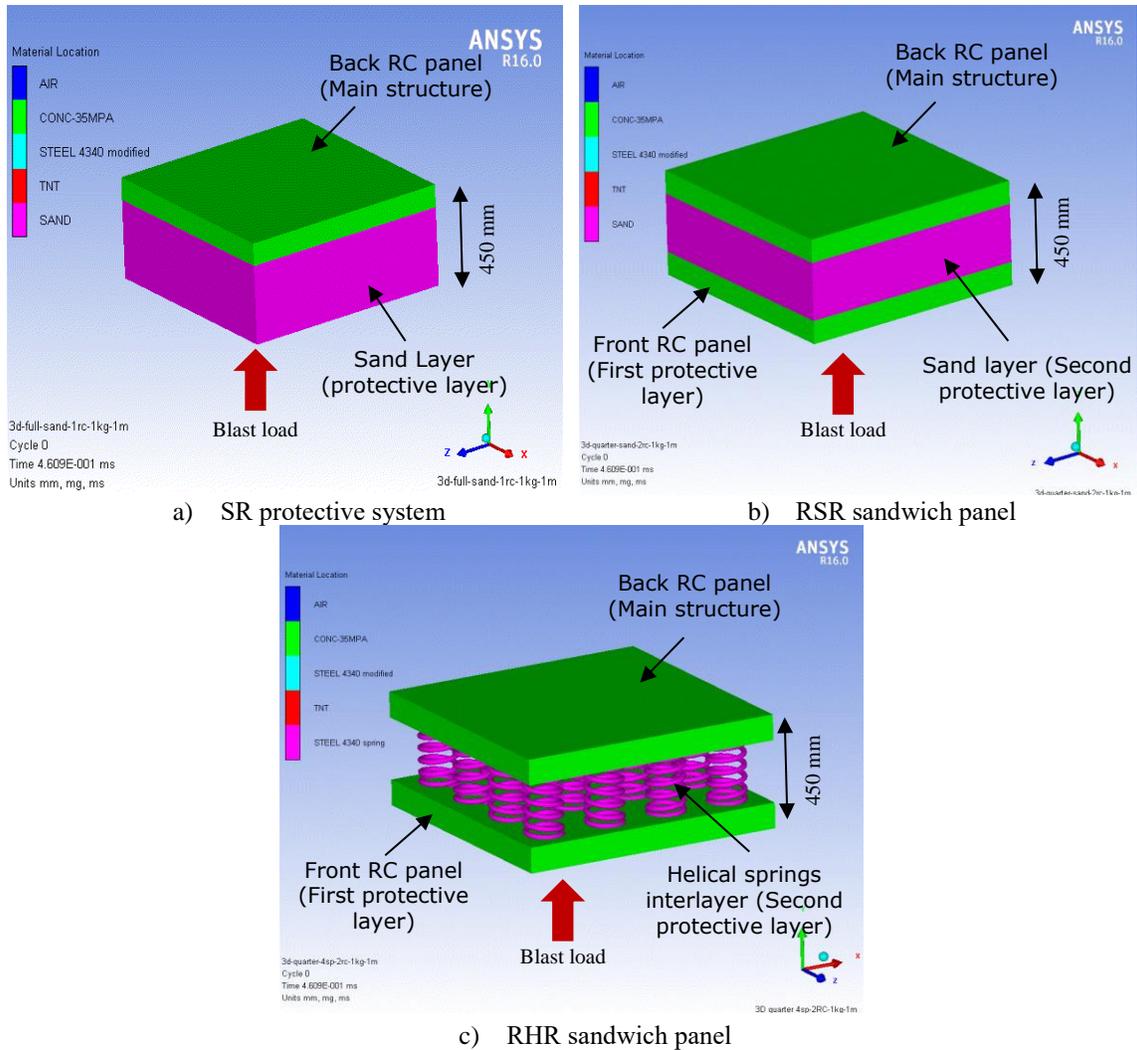
Detailed geometric nonlinearity (large deformation) and material nonlinearity (plasticity, strain hardening, strain softening and failure) are explicitly modeled. The numerical results for the RHR sandwich panel are verified using available experimental results, while the results of the RSR sandwich panel are verified using the same developed finite element model for the RHR sandwich panel. The only difference is that the helical springs interlayer is replaced by nonlinear 3D solid elements with sand properties which validated by previous experimental results.

6.2 Numerical modeling of the traditional (SR and RSR) protective systems under free air blast loads

Figures 6.1(a, b and c) show the 3D rendering of the SR, RSR and RHR protective systems, respectively. In this Chapter, a comprehensive numerical study is conducted on the SR, RSR and RHR protective systems to compare their behavior against different levels of free air blast loads. In this numerical study, 3D full numerical models are created to accurately investigate the different performances of the SR, RSR and RHR systems. A fully coupled Euler-Lagrangian interaction is applied between the explosion environment and the components of the studied structure. These

protective system models are subjected to different free air spherical blast charges of 1, 5 and 10 Kg TNT at a SoD of 1 m. These blast charges are located above the center of the entire system. The dimensions of the RC panels are 1 m by 1 m with a depth of 100 mm. The dimension of the dry sand interlayer is 1 m by 1 m with a depth of 250 mm, which is the same depth as the helical springs interlayer. All the boundary conditions and material properties for the concrete panels of the RHR and RSR models are identical. The back RC panel is simply supported at the four edges at its back face for the three protective systems. As for the SR, a transmit boundary condition is applied to all the outer faces of the sand block except for the upper face which defines the air/sand interface and the lower face which defines the sand/back RC panel interface. As for RSR, the transmit boundary condition is applied to all the outer faces of the sand block except for the upper face which defines the front RC panel/sand interface and the lower face which defines the sand/back RC panel interface. Transmit boundary condition is used to simulate an infinitely large material domain in which the applied pressure can be transmitted across the material boundaries without being reflected (ANSYS-AUTODYN, 2005; Laine and Sandvik, 2001).

On the other hand, when the RSR sandwich panel is compressed vertically, the lateral translational boundary condition at the sides of the sand layer will allow the imparted pressure to propagate across the sides without being reflected. The sand layer is modeled using 3D solid elements. Each sand element size is nominated to be 10 mm to be compatible with the number of elements of the two RC panels as they are physically in contact with each other. The sand layer is discretized into more than 62500 elements for the SR and RSR systems. Figure 6.2 shows a quarter numerical model of the RSR sandwich panel.



a) SR protective system

b) RSR sandwich panel

c) RHR sandwich panel

Figure 6.1 Full numerical configuration of the a) SR, b) RSR and c) RHR protective systems

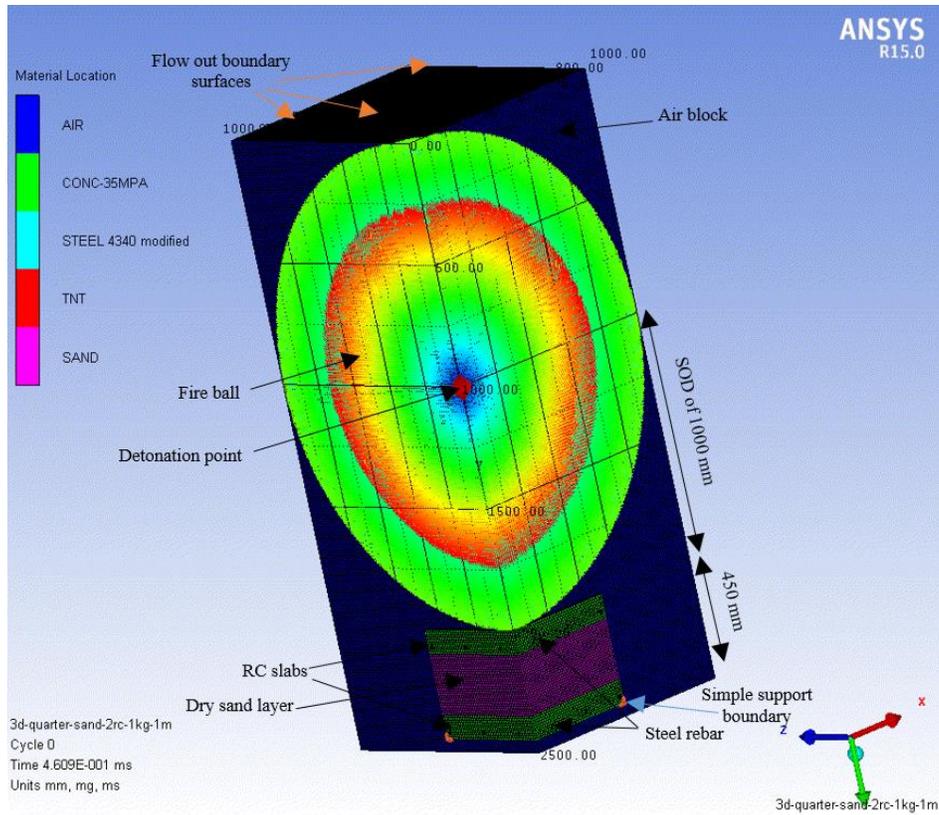


Figure 6.2 A quarter numerical model of the RSR sandwich panel

To accurately model the behavior of the SR, RSR and RHR systems against blast load, each component is experimentally validated with the available blast field tests. For the RHR sandwich panel, the proposed numerical model is validated in the previous Chapter. Accordingly, the validation of the proposed model for SR and RSR system will be discussed here.

6.2.1 Dry sand material modeling

Laine and Sandvik (2001) proposed a numerical sand model based on experimental data measured from triaxial tests. This proposed material model is so-called “porous-material/compaction” model and it was widely used by the blast engineering researchers (Bergeron et al., 1998; Grujicic et al.,

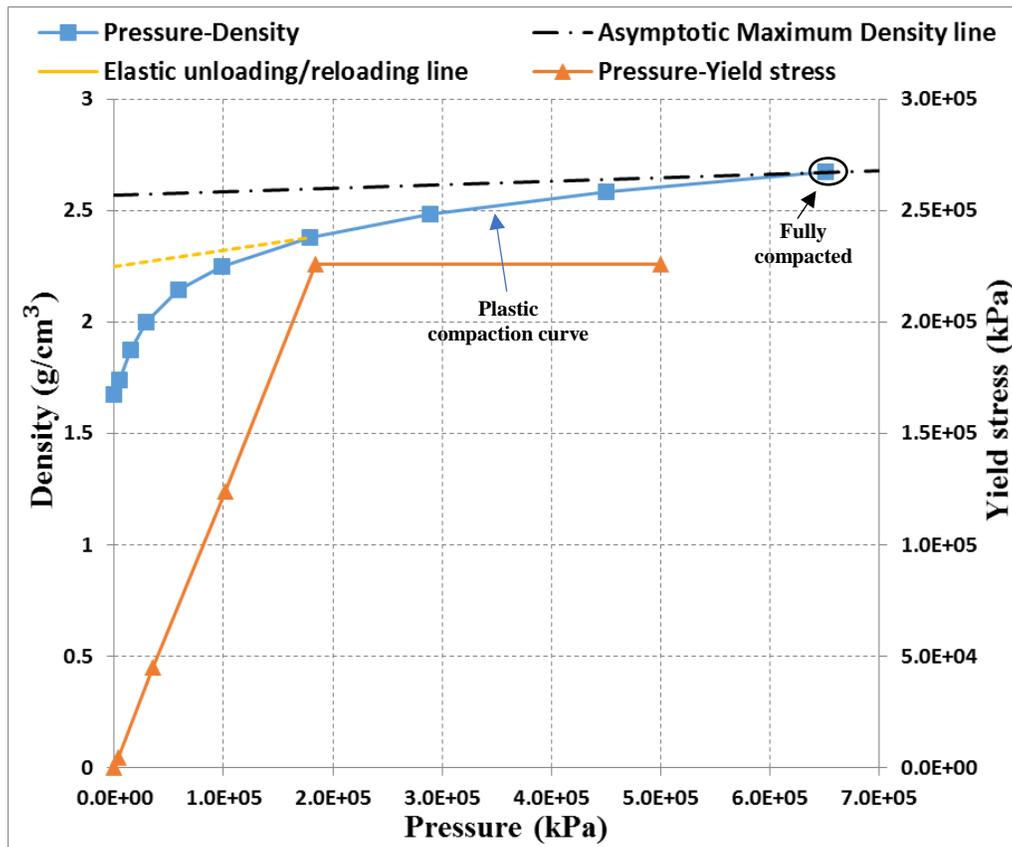
2008, 2007, 2006a, 2006b; Larcher and Gebbeken, 2012; Pickering et al., 2012; Wu et al., 2004). The equation of state (EOS) for sand is so-called the compaction equation and it can be expressed as equation 6.1. This EOS is a piece-wise linear relationship between pressure and density, as shown in Figure 6.3(a). This relationship represents a plastic compaction path until the endpoint, which represents the full compaction of sand particles. Knowing that, when sand experienced full compaction, it converted to a rigid body (Pickering et al., 2012). Any more pressure applied beyond the full compaction state will be controlled by elastic loading linear pressure-density relationship ($P - \rho$) as expressed in equation 6.2. As for the strength equation, MO Granular equation is used (Laine and Sandvik, 2001), in which three piece-wise linear relationships are implemented: (1) Pressure-Yield stress, as shown in Figure 6.3(a), (2) Yield stress-Density, and (3) Density-Shear modulus, as shown in Figure 6.3(b). In this strength model, yield stress $Y(\rho, P)$ has two components; one affected by the pressure $f_2(P)$ and the other by density $f_1(\rho)$. For sand model description, the density dependent part $f_1(\rho)$ is eliminated as expressed in equation 6.3 (Laine and Sandvik, 2001). Where: ρ_i and P_i are the density and pressure ten pairs defining the piece-wise linear relationship. C_s is the sound speed in the fully the compacted sand at zero pressure and ρ_s is the mass density of the fully-compacted sand under zero applied pressure value.

$$P = P_i + \frac{P_{i+1} - P_i}{\rho_{i+1} - \rho_i} \rho \quad , \quad i = 1 \text{ to } 9 \quad (6.1)$$

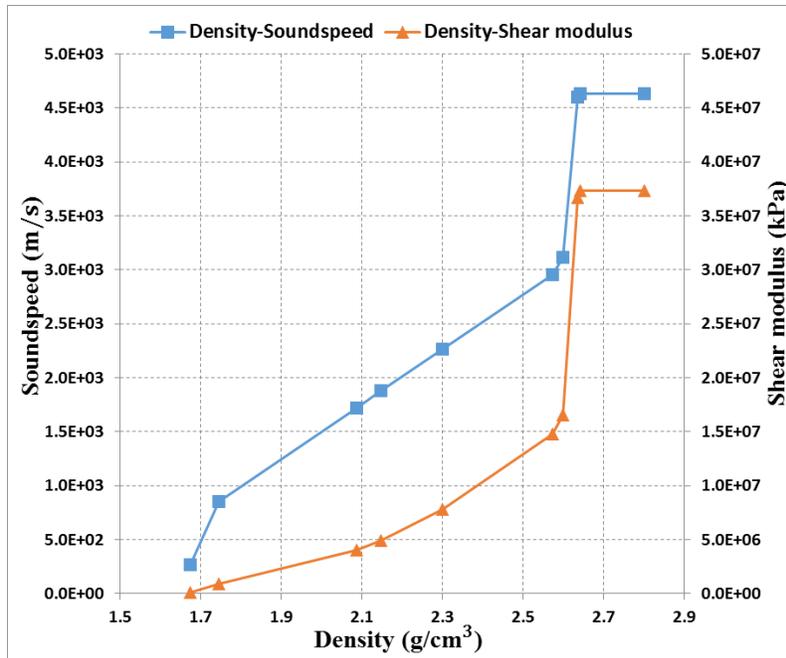
$$P = C_s^2(\rho - \rho_s) \quad (6.2)$$

$$Y(\rho, P) = f_1(\rho) + f_2(P) \quad , \quad f_1(\rho) = 0 \quad (6.3)$$

The unloading/reloading slope is expressed by the shear modulus, which is a function of the level of soil compaction (i.e., density) as shown in Figure 6.3(b). Finally, the failure of sand is dominated by a minimum pressure value of -1 KPa. Failure occurs when the pressure becomes less than the assigned value. This failure is called bulk failure. The rehaul option is used in which the cell rehauls when the failed cell has a positive pressure value. Table 6.1 shows the material data used for dry sand in this numerical study (ANSYS-AUTODYN, 2005).



(a) Pressure-Density and Pressure-Yield stress relationships



(b) Density-Soundspeed and Density-Shear modulus relationships

Figure 6.3 Dry sand material properties as used in the numerical modeling

Table 6.1 Material data of the dry sand used in this study (ANSYS-AUTODYN, 2005)

Reference Density (g/cm³)	2.641
Equation of state	Compaction
Strength	MO Granular
Failure	Hydro (P _{min})
Hydro tensile limit, P_{min} (KPa)	-1.0
Reheal	Yes
Crack Softening	No
Erosion	Geometric strain
Erosion Strain	2
Type of Geometric strain	Instantaneous

6.2.1.1 Validation of the dry sand modeling

In this section, the dry sand model is validated by using previous experimental work, which can be found in the technical report by Bergeron et al., (1998). The experimental test was conducted to examine the behavior of a dry sand layer subjected to surface blast load. The dry sand was located in a bucket to retain its shape. The weight of the blast charge was 100 gm of composition C-4, where C-4 is a kind of plastic explosives. The blast charge was located at the surface of the dry sand layer in a form of a cylindrical shape with a diameter of 64 mm and a thickness of 20 mm. The upper surface of the blast charge is at the same level of the upper surface of the sand layer, where the depth of burial (DOB) is equal to zero. Figure 6.4 shows the test setup of the dry sand experiment (Bergeron et al., 1998). The results were expressed in a form of the sand ejecta and crater diameter, which is created due to the detonation of the blast charge in the sand layer.



Figure 6.4 Test setup of the dry sand experiment (Bergeron et al., 1998)

In this section, a 2D axisymmetric numerical model is created to simulate this experimental test. This numerical model is developed using the multi-material flow (Euler) solver, which is implemented in AUTODYN. The mechanical properties of the sand material used in this simulation are listed in Table 6.1. The air block is modeled as an Ideal gas and the C-4 is described by the JWL equation of state as in the case of TNT modeling which mentioned in Chapter 4. An element size of 1 mm is selected for the Euler mesh. A flow out boundary condition is applied as the outer sides of the air and sand block except for the symmetric axis. A detonation point is located at the center of the C-4 part. Figure 6.5 shows the configuration of a half numerical model, which is developed to simulate the dry sand experiment.

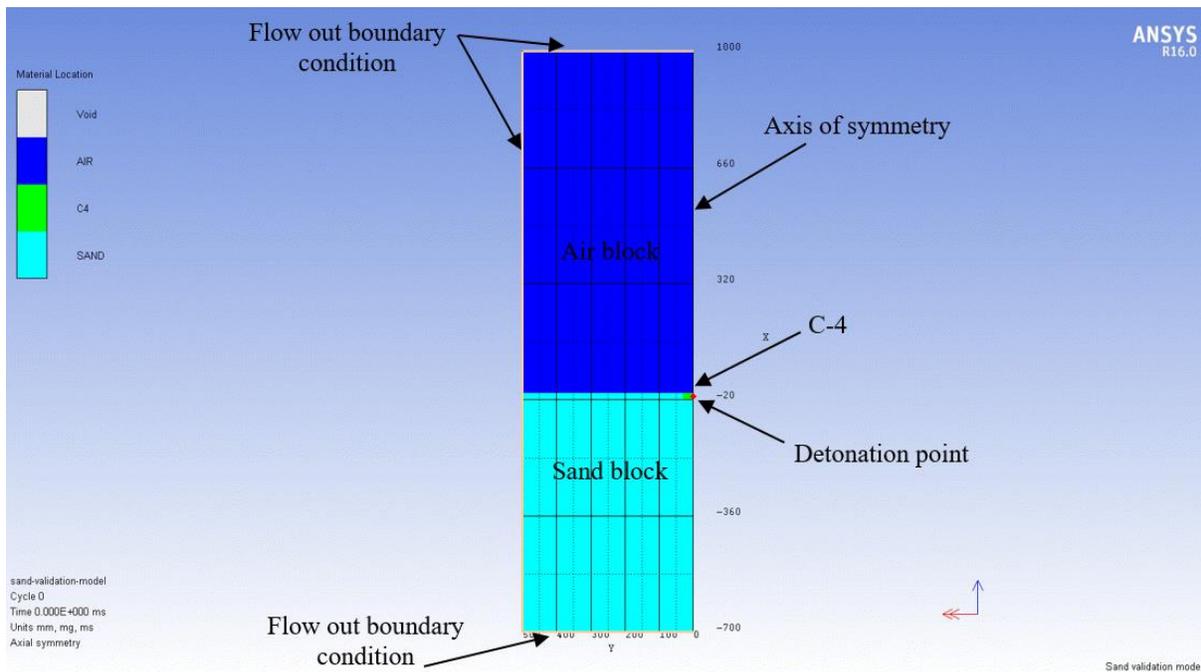


Figure 6.5 A half numerical model developed in this study to simulate the dry sand experimental test

The numerical results are then compared with the previous experimental results. It is observed that the trend of the crater formation for both the experimental test and numerical simulation are

similar, as shown in Figure 6.6. It is observed that the height of the sand ejecta in the numerical simulation at time 0.2 ms reaches a maximum height of 154 mm. whereas, in the experimental test, at the same time, it reached a height of 174 mm. The difference percentage between the two values is 11 %, which can be accepted. Table 6.2 shows a comparison between the measured crater diameter value and that obtained from the numerical analysis. It is noted that the numerical results show a good agreement with its corresponding experimental data and the difference percentage between them is 9 % that can be accepted. Accordingly, this comparison shows the ability of the dry sand model to simulate an accurate behavior of the sand material against blast loads.

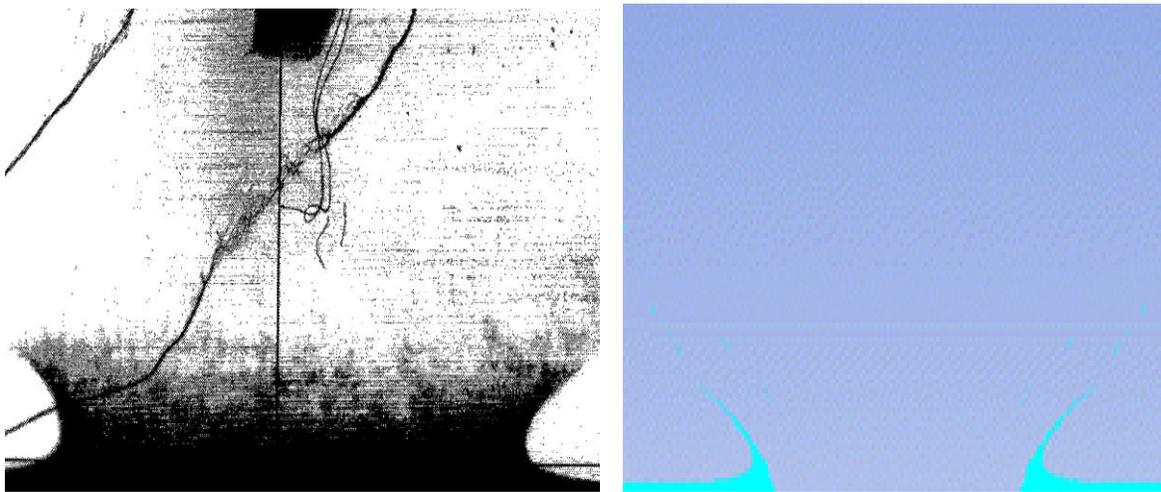


Figure 6.6 The trend of the a) experimental (Bergeron et al., 1998) and b) numerical crater formation of the dry sand test

Table 6.2 The experimental and numerical crater diameter values for the dry sand test

Measured crater diameter (mm)	Numerical crater diameter (mm)	Error (%)
310	282	9

After validating the dry sand numerical modeling, 3D numerical models are created to simulate the SR and RSR protective systems. In these simulations, the dry sand layer is modeled as 3D Lagrangian elements with eight nodes. A fully coupled Lagrangian-Lagrangian interaction is applied between the sand elements and a trajectory interaction between the sand layer and the two adjacent faces of the two RC panels. These interactions enable a more realistic transfer of stresses between the surfaces of the sand layer and the RC panels. In addition, lateral transmit boundary conditions are applied at the lateral surfaces of the sand layer of the SR and RSR protective systems to model the physical infinitely sand domain accurately. A fully coupled Euler-Lagrangian interaction is applied between the explosion environment and the entire SR and RSR protective system components.

6.3 Comparison results and discussion

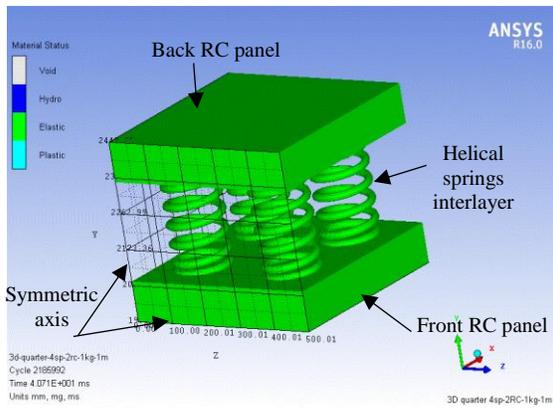
Table 6.3 shows the comparison between the total weight of the front RC panel and the interlayer of the RHR, SR and RSR system. The simple comparison shows that the RHR interlayer is 84 % lighter than that of the RSR and the total weight of the two first layers of the RHR sandwich panel is 58 % and 59 % lighter than the sand layer of the SR and the two first layers of the RSR, respectively. This is a significant advantage of RHR, which can potentially reduce the additional loads, and the design costs of the shallow underground structures. It should be noted that if the sand is saturated or partially saturated, the dead weight will increase, hence making RHR even more advantageous. In addition, when the sand is filled in the core layer, it is usually compacted due to its own weight. Accordingly, the sand ability to withstand the blast loads decreased. This can be explained as the blast attenuation ability of sand depends on the existence of the air pores located between the sand particles. Both of the aforementioned problems are hard to be controlled

and need costly maintenance and monitoring (TM5-1300, 1990; UFC 3-340-02, 2008; Wu et al., 2004).

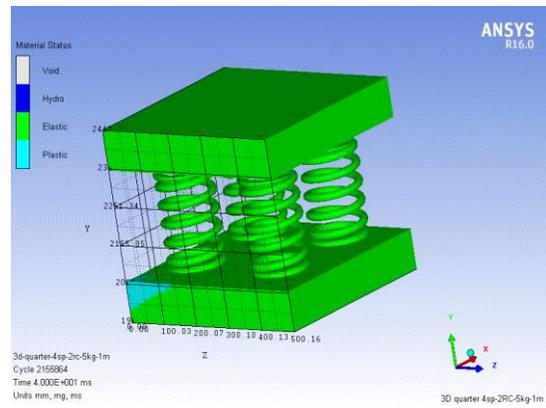
Table 6.3 Comparison between the weight of the front layer and interlayer of the SR, RSR and RHR systems

Sandwich panel name	Front RC panel (Kg)	Interlayer (Kg)	Total weight (Kg)	Total reduction percentage (%)
RSR	278.78	660.25	939.03	0.0
SR	924.35		924.35	1.6
RHR	278.78	106.72	385.50	59

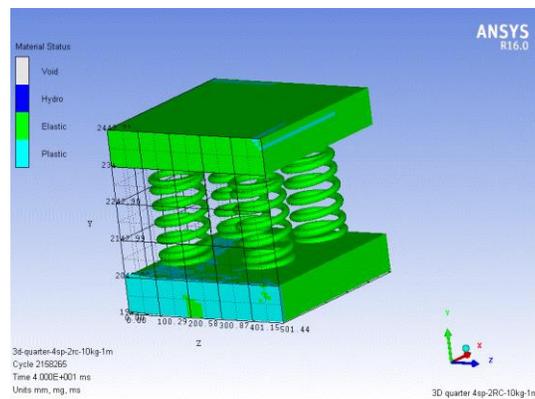
Figures 6.4(a), (b) and (c) show the material status (Elastic or Plastic) of the RHR sandwich panel components under the blast load of 1, 5 and 10 Kg TNT at a SoD of 1 m, respectively. The results show that the back panel suffered no damage in the case of the blast loads of 1 Kg TNT (Figure 6.7(a)) and 5 Kg TNT (Figure 6.7(b)) and suffered minor damage in the case of 10 Kg TNT (Figure 6.7(c)). These numerical results agree well with its corresponding experimental observation, which is discussed in Chapter 3. This shows that the RHR is very effective in protecting the back panel from the designated blast loads.



(a) 1 Kg TNT



(b) 5 Kg TNT

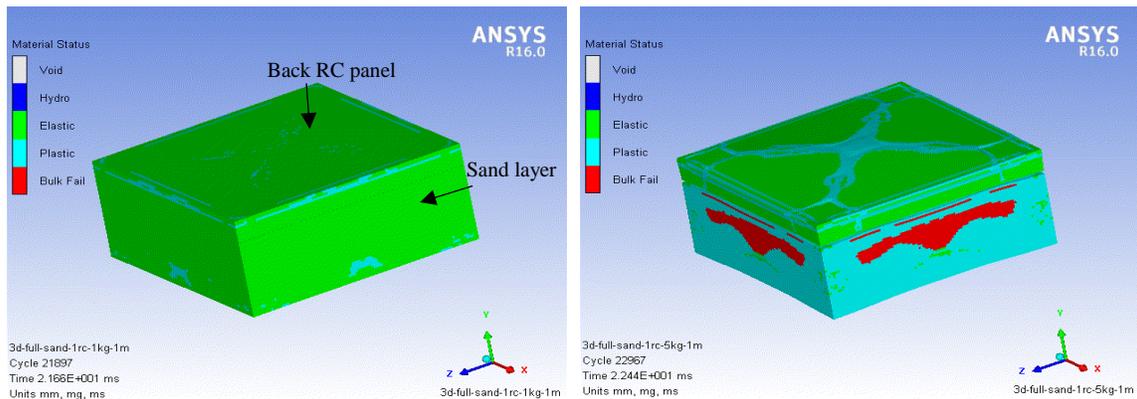


(c) 10 Kg TNT

Figure 6.7 Material status of the components of a quarter model of the RHR sandwich panel after subjecting to three different blast loads

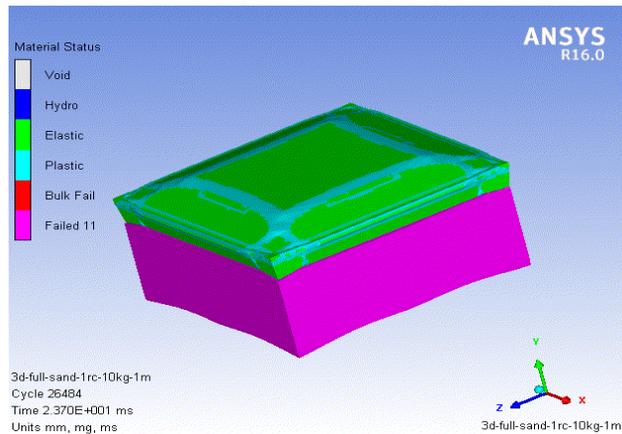
Figure 6.8(a), (b) and (c) show the material status (Elastic, Plastic and Bulk failure) of the SR protective system components after being subjected to different blast loads of 1, 5 and 10 Kg TNT at a SoD of 1 m above the center of the sand layer, respectively. It is observed that as the blast load changes from 1 Kg TNT to 10 kg TNT, the material status of the sand changes from elastic to plastic to bulk failure to failed status. Once the sand layer changed its material status from elastic to plastic or bulk failure, as shown in Figures 6.8(a and b), the sand layer is compacted and imparts any additional loads to the back RC panel. It can be observed that plastic zones occurred at the

edges of the back RC panel in the case of 1 Kg TNT that can be considered as severe damage, as shown in Figure 6.8(a). As for the 5 Kg loading case, many plastic zones occurred in the back panel, which can be considered as severe damage, as shown in Figure 6.8(b). As for the 10 Kg TNT loading case, the entire sand layer is failed and is not able to experience any more compaction as it is totally damaged. Accordingly, a considerable amount of blast load imparted to the back panel causing severe damage, as shown in Figure 6.8(c).



(a) 1 Kg TNT

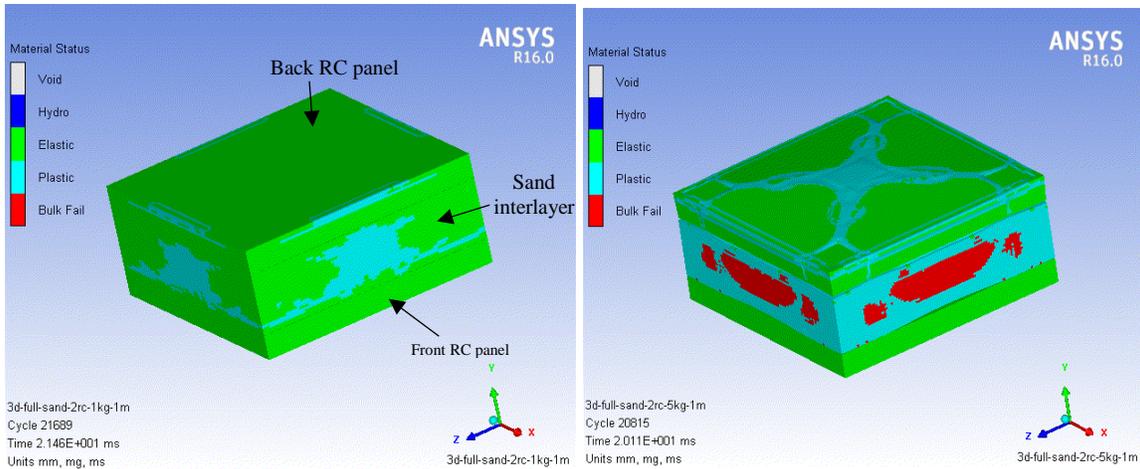
(b) 5 Kg TNT



(c) 10 Kg TNT

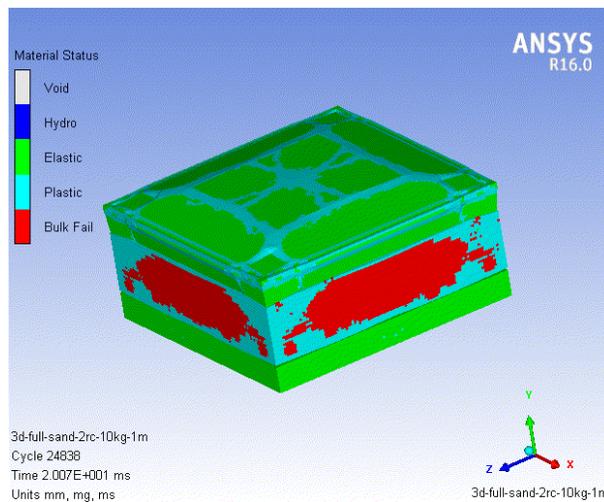
Figure 6.8 Material status of the sand layer and back RC panel after applying three different blast loads on the SR protective system

Figure 6.9(a), (b) and (c) show the material status (Elastic, Plastic and Bulk failure) of the RSR sandwich panel components after being subjected to different blast loads of 1, 5 and 10 Kg TNT at a SoD of 1 m above the center of the front RC panel, respectively. As the blast load changes from 1 Kg TNT to 10 kg TNT, the material status of the sand changes from elastic to plastic to bulk failure. Once the sand layer changed its material status from elastic to plastic or bulk failure, as shown in the three blast load cases in Figure 6.9, the sand layer compacted and imparted any additional loads to the back RC panel. Due to the poor elasticity of the sand layer, it experiences plastic compaction, which increases as the applied load increases until reaching the full compaction level. Accordingly, any excess energy will be imposed on the back RC panel. It can be observed that plastic zones occurred at the edges of the back RC panel in the case of 1 Kg TNT that can be considered as medium damage, as shown in Figure 6.9(a). As for the 5 Kg and 10 Kg TNT cases, many plastic zones occurred in the back panel that can be considered as severe damage, as observed in Figure 6.9(b and c). In addition, due to the existence of the sand layer as a shock-absorbing cushion beneath the front RC panel, the front RC panel did not suffer significant damage and imparted most of the applied energy to the sand layer.



(a) 1 Kg TNT

(b) 5 Kg TNT



(c) 10 Kg TNT

Figure 6.9 Material status of the front RC panel, sand interlayer and back RC panel after applying three different blast loads on the RSR sandwich panel

From Figures 6.8 and 6.9, it can be concluded that the sand layer in the SR protective system experienced more damage than that in the RSR sandwich panel for each blast loading case. This is attributed to the absence of the front RC panel in the case of SR protective system where the sand layer is directly exposed to the blast wave, which obligates the sand layer to absorb more

blast energy in each loading case than that absorbed by the sand interlayer of the RSR sandwich panel.

Figure 6.10 shows the comparison of damage level (DL) of the back RC panel of the SR, RSR and RHR systems under the three different blast loads considered. The result shows that the back RC panel of the SR experienced severe damage in the three loading cases of 1, 5 and 10 Kg TNT. As for the RSR sandwich panel, the back RC panel experienced medium damage under the blast load of 1 Kg TNT and severe damage in the loading case of 5 and 10 Kg TNT. On the other hand, the back panel of the RHR sandwich panel suffered no damage under the blast loads of 1 Kg and 5 Kg TNT while it experienced slight damage under the blast load of 10 Kg TNT. This shows that the RHR sandwich panel has a robust blast resistant performance when compared with the SR and RSR protective systems.

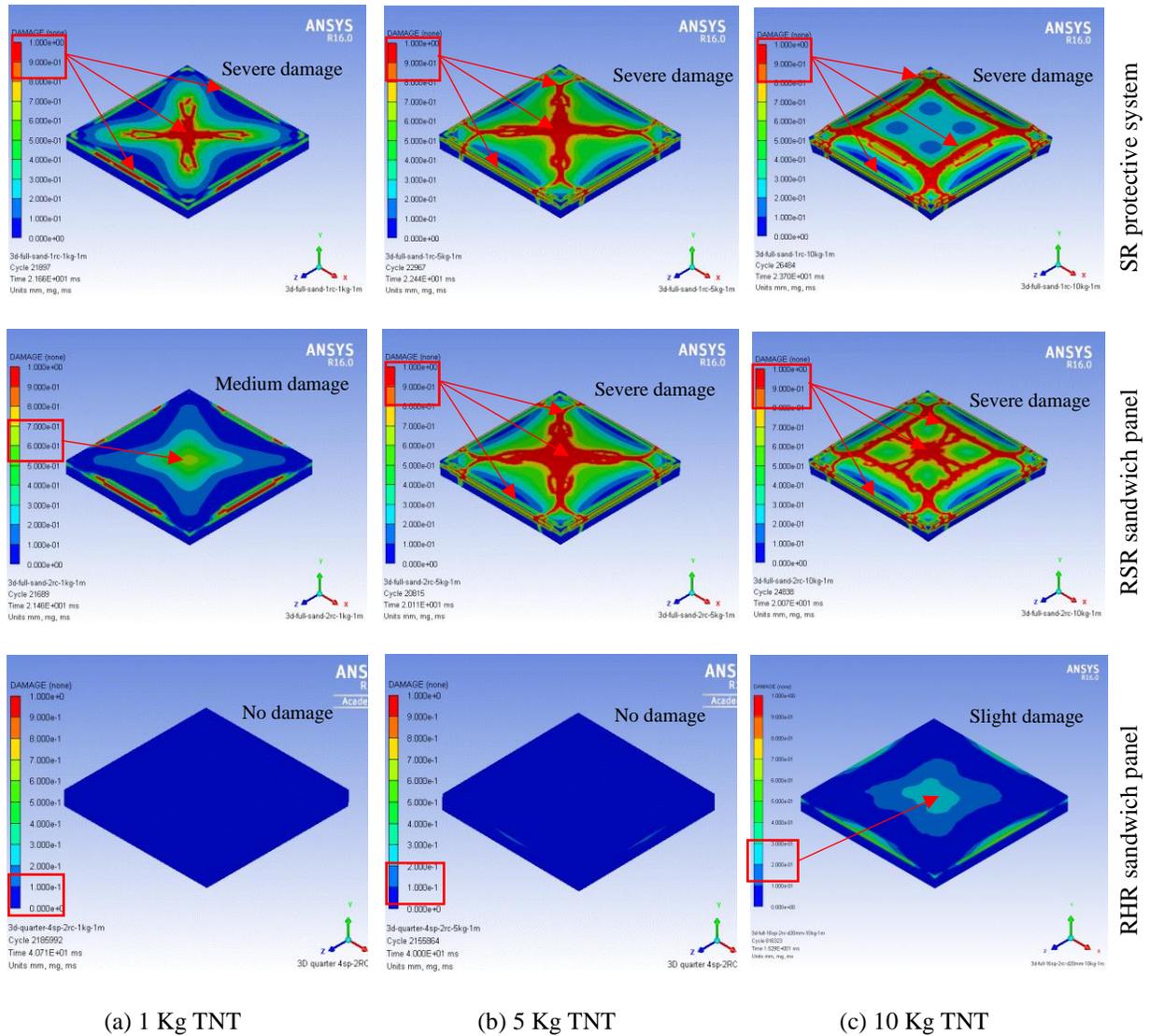


Figure 6.10 Damage contours of the back RC panel of the SR, RSR and RHR systems when subjected to 1, 5 and 10 Kg TNT at a SoD of 1 m

Figure 6.11 shows a comparison between the plastic work done by the front RC panels for RSR and RHR sandwich panel under the three blast loads considered. In the case of the RSR sandwich panel, it is found that the back RC panel experienced more plastic work than that observed on the front RC panel, which conflicts with the main objective required from any protective system. The difference between the maximum plastic work done by the front and the back RC panels for the

RSR sandwich panel under the three different load cases of 1, 5 and 10 Kg TNT are 98 %, 89 % and 66 %, respectively.

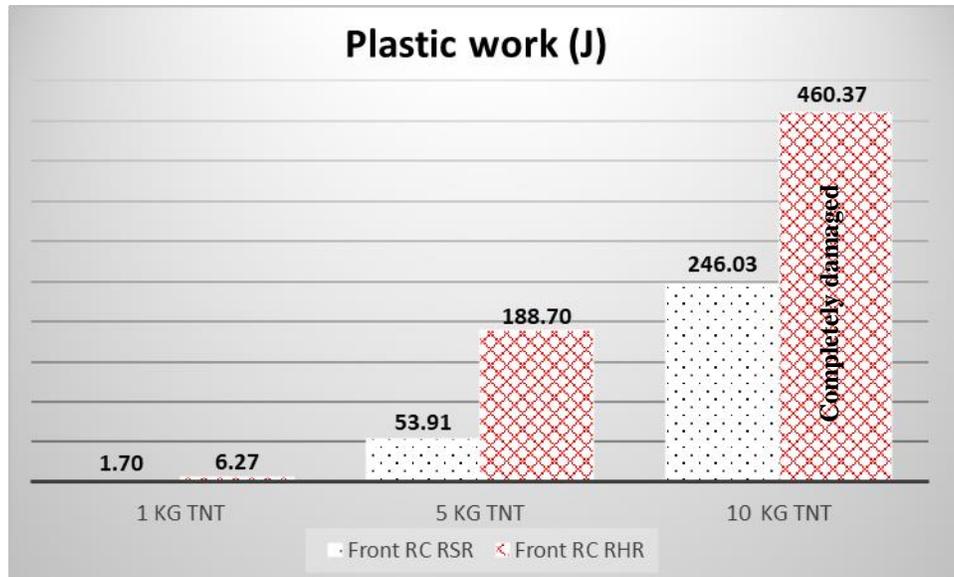


Figure 6.11 Comparison of the maximum plastic work done by the front RC panel of the RSR and RHR sandwich panels

Figure 6.12 shows a comparison between the plastic work done by the back RC panel of the SR, RSR and RHR under the three blast loads considered. It is found that the plastic work done by the back RC panel of the RHR sandwich panel is significantly less than the plastic work done by its counterpart of the SR and RSR protective systems. The reduction percentages of the plastic work done by the back RC panel of the RHR sandwich panel under the load cases of 1, 5 and 10 Kg TNT by 99.7 %, 98 % and 73 %, respectively when compared with the RSR sandwich panel and by 99.8 %, 98 % and 66 %, respectively when compared with the SR protective system.

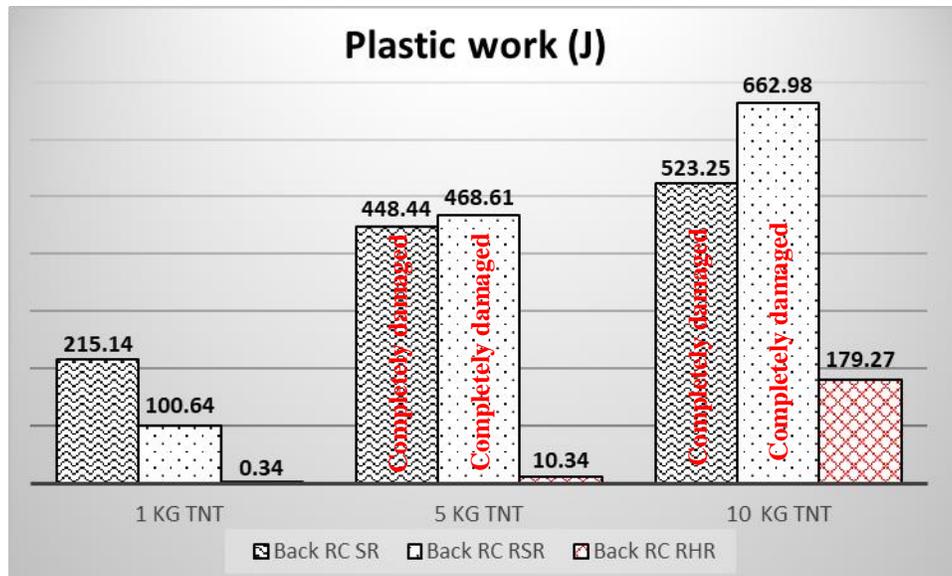


Figure 6.12 Comparison of the maximum plastic work done by the back RC panel of the SR, RSR and RHR protective systems

In addition, the total and internal energy are analyzed and discussed for each component of the SR and RSR to evaluate the efficiency and effectiveness of the dry sand layer/interlayer in mitigating the imparted energy to the back RC Panel when compared with the helical springs interlayer. Figures 6.13, 6.14 and 6.15 show the total, internal and kinetic energy time absorbed by the components of the RSR and RHR sandwich panels under 1, 5 and 10 Kg TNT at a SoD of 1 m.

For the front RC panel, it is found that the maximum total energy dissipated by the front RC panel of the RHR sandwich panel under the three different blast loads of 1, 5 and 10 Kg TNT is greater than that dissipated by the front RC panel of the RSR sandwich panel by 95 %, 112 % and 141 %, respectively. In addition, it is found that the maximum kinetic energy absorbed by the front RC panel of the RHR under the three different blast loads of 1, 5 and 10 Kg TNT is greater than that absorbed by the front RC panel of the RSR by 104 %, 119 % and 150 %, respectively. On the other

hand, the internal energy gained by the front RC panel of the RHR under the three different blast loads of 1, 5 and 10 Kg TNT is less than that gained by the front RC panel of the RSR by 63 %, 24 % and 13 %, respectively. These results can be explained as in the case of the RHR sandwich panel, the front RC panel dissipated a considerable amount of energy mainly in the form of kinetic energy and a small portion in the form of internal energy due to the existence of the elastic supports beneath it, which enforces the front RC panel to gain more kinetic energy. As for the RSR sandwich panel, the front RC panel mainly dissipated the applied blast energy in the form of instantaneous kinetic energy at the beginning of its response, which decayed rapidly. During that initial response, the internal energy increased gradually to a permanent value, which is considered as the plastic energy dissipation. The reason behind that behavior is the existence of the sand interlayer beneath the front RC panel, which has poor elastic behavior where it rapidly damped out the vibration of the RC panel causing the increase of the internal energy gained by the front RC panel.

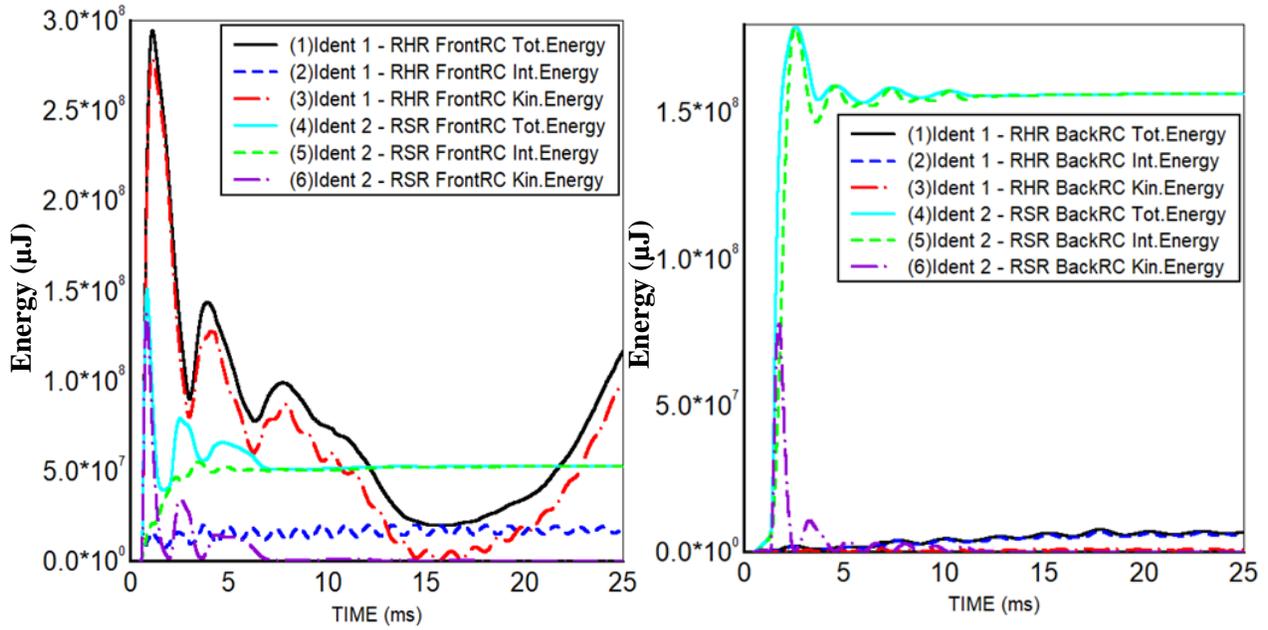
For the core layer, it is found that the helical springs interlayer mainly dissipated the applied blast energy in the form of elastic internal energy where it is released again. A small portion of the dissipated energy is gained as kinetic energy. This is attributed to the elastic behavior of the helical springs located in the core layer. As for the sand interlayer, it absorbs a considerable amount of energy, which mainly gained in a form of plastic internal energy and a small portion in the form of kinetic energy. At the very beginning of the sand response, sand interlayer instantaneously gained a considerable amount of energy mainly in the form of internal energy and then sharply decreased to a permanent value, which is the plastic internal energy value. The difference between the maximum energy dissipation value and the permanent value in the amount of elastic energy

dissipated by the sand interlayer. The reason behind that behavior is that when the blast load hit the front RC panel of the RSR sandwich panel, most of the applied energy is imparted to the sand interlayer. Accordingly, the sand layer absorbed a considerable amount of that applied energy in the form of plastic internal energy by performing compaction between its solid particles.

It is found that the amount of elastic energy dissipated by the helical springs interlayer under the three different blast loads of 1, 5 and 10 Kg TNT is greater than that dissipated by the sand interlayer by 4 %, 70 % and 346 %, respectively. This result indicates that the elastic energy dissipated by the helical springs interlayer increases significantly by increasing the blast load. On the contrary, the elastic energy dissipated by the sand interlayer decreases by increasing the blast load.

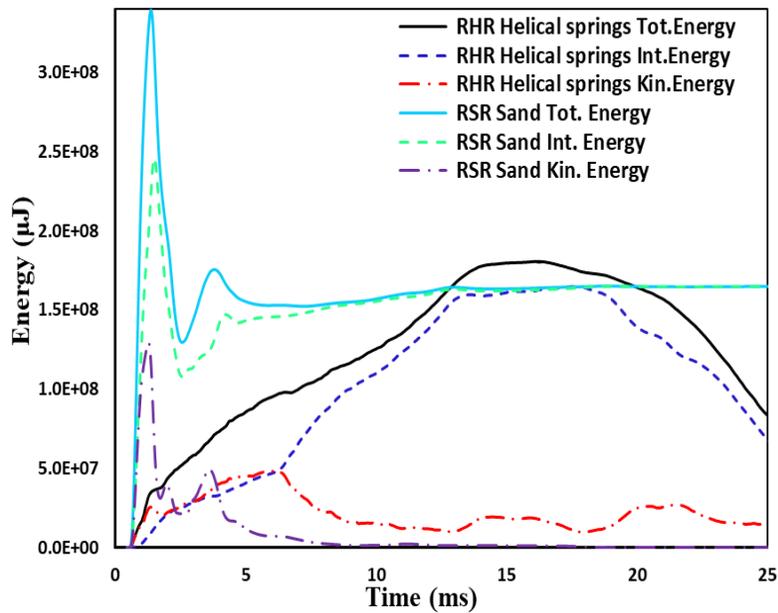
For the back RC panel, it is found that the maximum total energy dissipated by the back RC panel of the RHR sandwich panel under the three different blast loads of 1, 5 and 10 Kg TNT is less than that dissipated by the back RC panel of the RSR sandwich panel by 96 %, 95 % and 85.5 %, respectively. In addition, it is found that the maximum kinetic energy absorbed by the back RC panel of the RHR under the three different blast loads of 1, 5 and 10 Kg TNT is less than that absorbed by the back RC panel of the RSR by 99 %, 99 % and 98 %, respectively. The internal energy gained by the back RC panel of the RHR under the three different blast loads of 1, 5 and 10 Kg TNT is less than that gained by the back RC panel of the RSR by 96 %, 94 % and 81 %, respectively. These results can be explained as in the case of the RHR sandwich panel, the helical springs interlayer stored the imparted energy gradually and releases it out after reaching the maximum displacement, which enforces the front RC panel to absorb a considerable amount of

the applied load and accordingly, the two layers dissipate most of the applied energy before reaching the back RC panel, as shown in Figures 6.13, 6.14 and 6.15. As for the RSR sandwich panel, the front RC panel mainly dissipated the applied blast energy in the form of instantaneous kinetic energy at the beginning of its response, which decayed rapidly due to the existence of the sand interlayer. During that moment, the sand interlayer absorbs a considerable amount of the applied blast load in the form of plastic compaction and partially imparting the remaining load to the back RC panel. This plastic compaction increases by increasing the applied load until reaching the full compaction state, where the sand layer becomes a rigid layer. Consequently, excessive energy will be imparted to the back RC panel and absorbed in the form of plastic internal energy. Figures 6.13, 6.14 and 6.15 show the total, internal and kinetic energy time absorbed by the components of the RSR and RHR protective systems under 1, 5 and 10 Kg TNT at a SoD of 1 m, respectively.



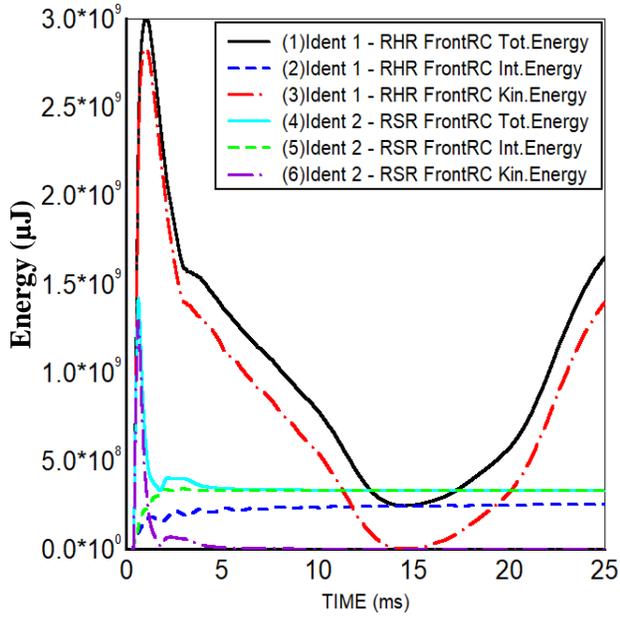
Front RC panel

Back RC panel

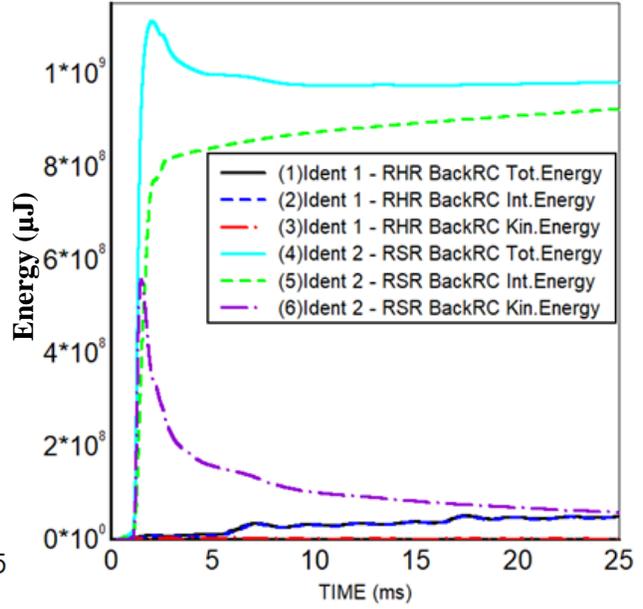


Core layer

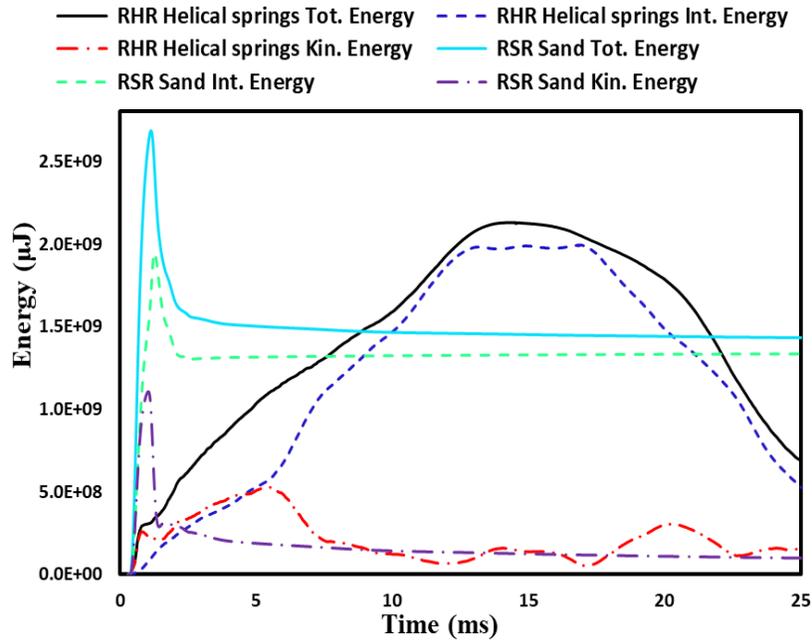
Figure 6.13 Comparison between the total, internal and kinetic energy absorbed by the components of the RSR and RHR sandwich panels under 1 Kg TNT at a SoD of 1 m



Front RC panel

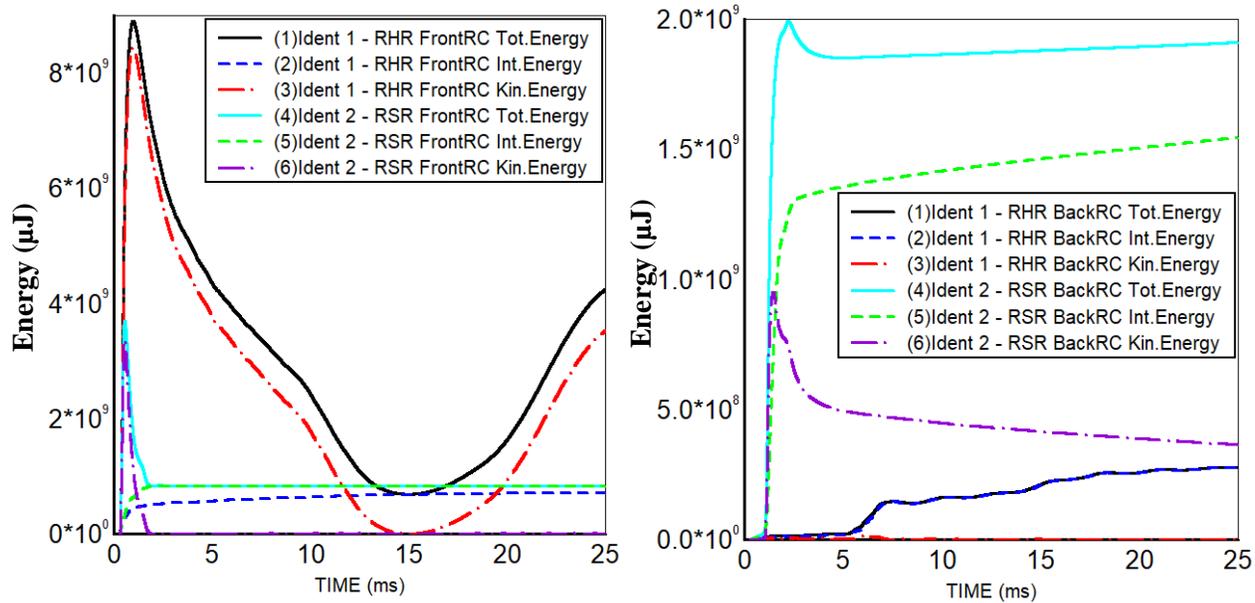


Back RC panel



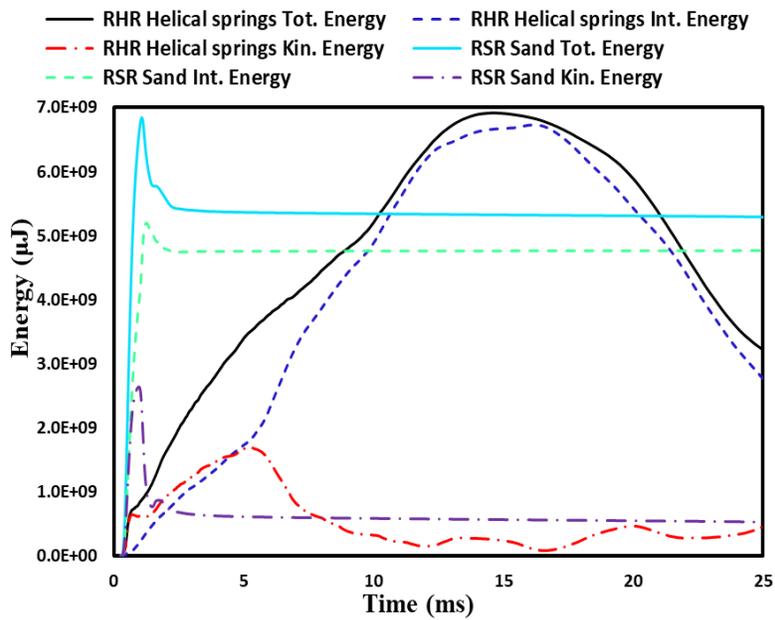
Core layer

Figure 6.14 Comparison between the total, internal and kinetic energy absorbed by the components of the RSR and RHR sandwich panels under 5 Kg TNT at a SoD of 1 m



Front RC panel

Back RC panel



Core layer

Figure 6.15 Comparison between the total, internal and kinetic energy absorbed by the components of the RSR and RHR sandwich panels under 10 Kg TNT at a SoD of 1 m

For the case of SR protective system, Figures 6.16, 6.17 and 6.18 show the total, internal and kinetic energy time absorbed by the components of the SR protective systems under 1, 5 and 10 Kg TNT at a SoD of 1 m, respectively. Due to the different nature of this protective system, only the back RC panel of the RHR sandwich panel is illustrated in the figures to observe the different behavior of the back RC panel for each protective system.

For the sand layer, a considerable amount of energy dissipated in the form of plastic internal energy due to the exposure of the sand layer to the blast wave directly. It is found that the amount of energy dissipated by the sand layer of the SR is significantly greater than that dissipated by the sand interlayer of the RSR sandwich panel. This is attributed to the difference in depth and location as the sand layer is 35 cm in the case of SR, whereas the sand layer is 25 cm in the case of RSR and the sand layer exposed to the blast load in the case of SR, whereas the sand interlayer is located beneath the front RC panel in the case of RSR .

For the back RC panel, it is found that the maximum total energy dissipated by the back RC panel of the RHR sandwich panel under the three different blast loads of 1, 5 and 10 Kg TNT is less than that dissipated by the back RC panel of the SR sandwich panel by 98 %, 95 % and 86 %, respectively. In addition, it is found that the maximum kinetic energy absorbed by the back RC panel of the RHR under the three different blast loads of 1, 5 and 10 Kg TNT is less than that absorbed by the back RC panel of the SR by 99 %, 99 % and 98 %, respectively. The internal energy gained by the back RC panel of the RHR under the three different blast loads of 1, 5 and 10 Kg TNT is less than that gained by the back RC panel of the SR by 98 %, 94 % and 82 %, respectively. In addition, it is found that the amount of energy dissipated by the back RC panel of

the SR protective system is relatively greater than that dissipated by the back RC panel of the RSR. This is attributed to the early failure of the sand layer of the SR system due to the full compaction where the sand layer becomes a rigid layer and unable to absorb any more energy. Consequently, excessive energy will be imparted to the back RC panel and gained in the form of plastic internal energy.

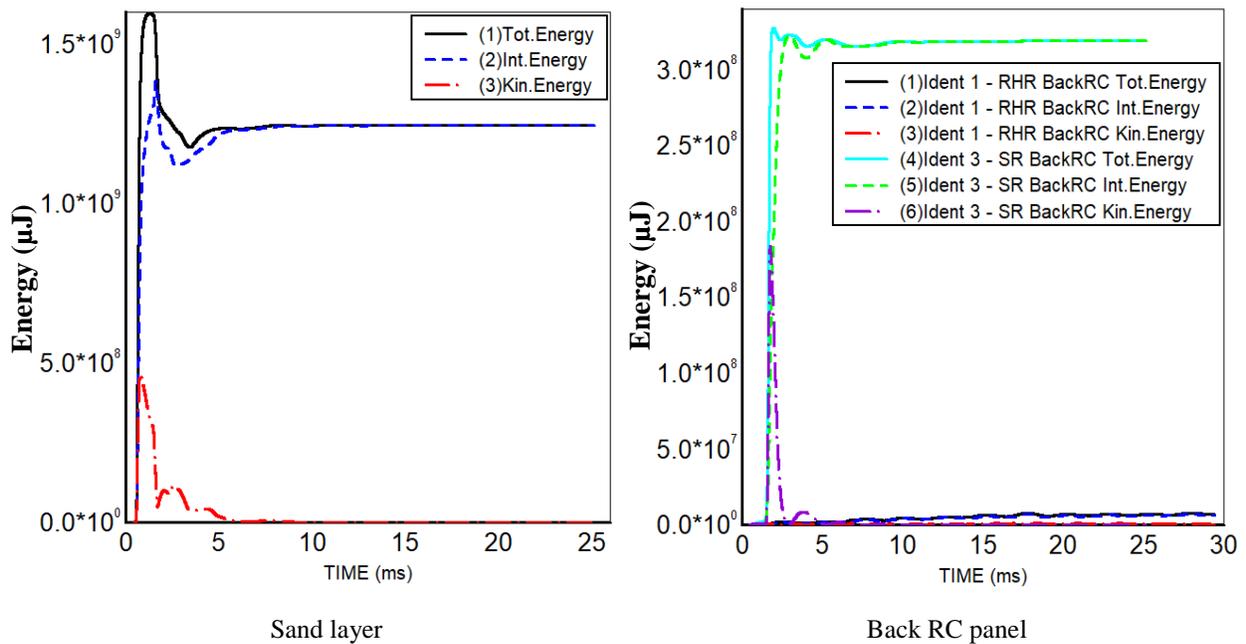


Figure 6.16 The total, internal and kinetic energy absorbed by the sand layer of the SR protective system and the back RC panel of the SR and RHR systems under 1 Kg TNT at a SoD of 1 m

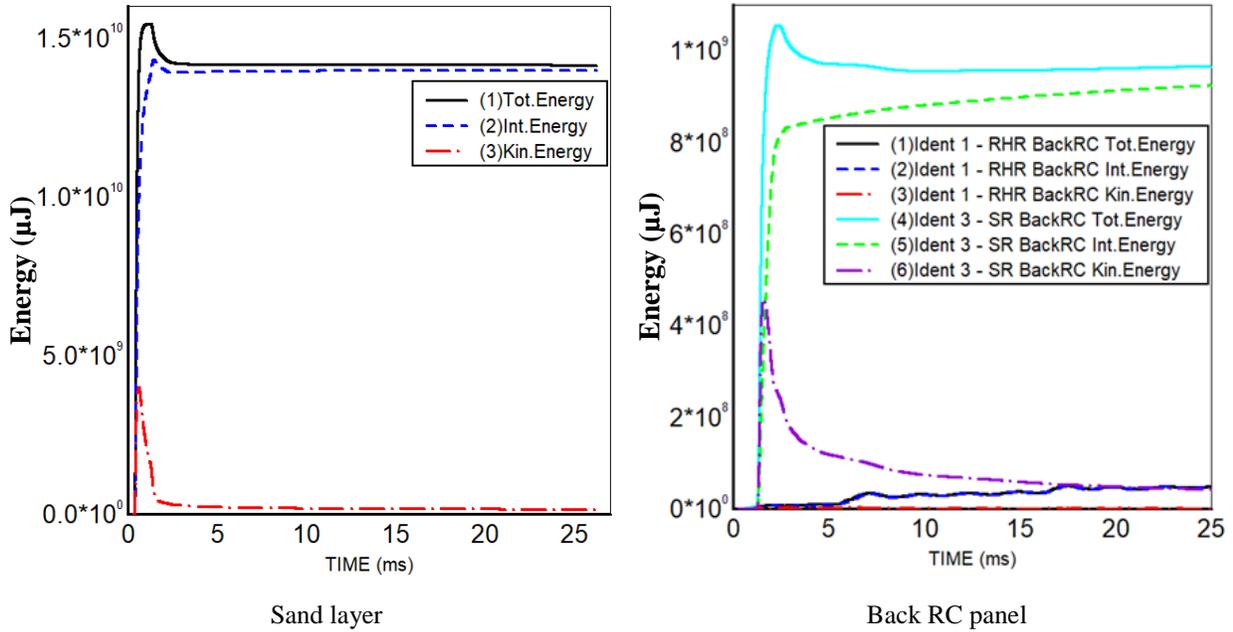


Figure 6.17 The total, internal and kinetic energy absorbed by the sand layer of the SR protective system and the back RC panel of the SR and RHR systems under 5 Kg TNT at a SoD of 1 m

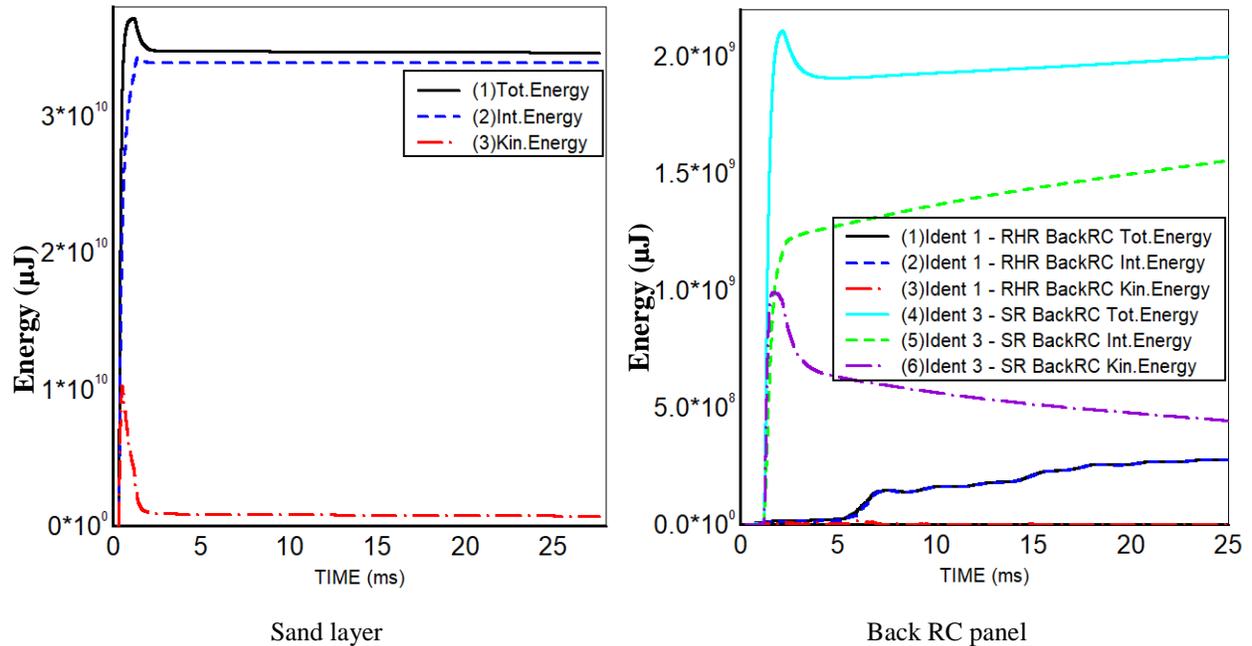


Figure 6.18 The total, internal and kinetic energy absorbed by the sand layer of the SR protective system and the back RC panel of the SR and RHR systems under 10 Kg TNT at a SoD of 1 m

Figure 6.19 shows the maximum total energy dissipated by the main components of the SR, RSR and RHR protective system under the three different blast loads. It is found that the total energy dissipated by any sandwich panel increases by increasing the blast load. It is worth mentioning that the total energy dissipated by the RHR sandwich panel is less than that dissipated by RSR and SR protective system, respectively. This can be explained as due to the existence of the front RC panel and helical springs interlayer, which reflects a considerable portion of the applied blast energy in the opposite direction, which accordingly, decreases the total energy absorbed by the sandwich panel. On the contrary, the sand layer in the SR and RSR protective systems absorbs most of the applied energy as plastic internal energy in a form of plastic compaction, which accordingly increases the total energy dissipated by the SR and RSR protective system. Only, in the case of 10 Kg TNT, the total energy dissipated by the RHR is higher than that of the RSR. This is due to the full damage of the front RC panel, which allows excess energy to be absorbed by the back RC panel.

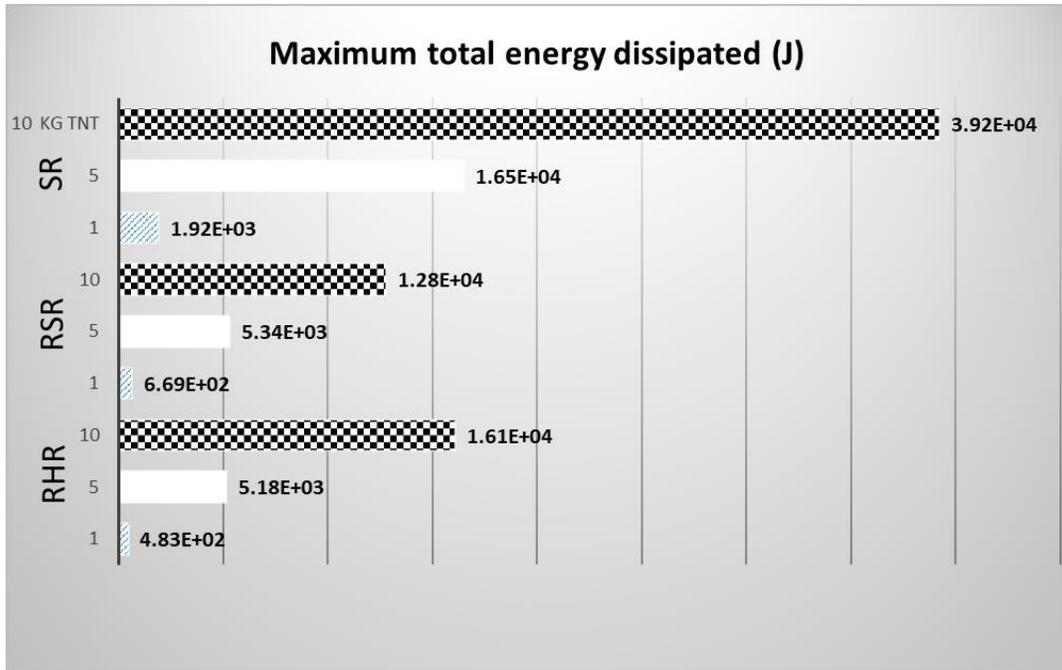


Figure 6.19 The maximum total energy dissipated by the SR, RSR and RHR protective systems under the three different blast loads

Figure 6.20 shows the percentage of the total energy dissipated by each component of the SR, RSR and RHR protective systems under the three different blast loads. It can be observed that helical spring's interlayer dissipated an average value of 40.5 % of the total energy dissipated by the entire RHR sandwich panel under the three loading cases. For the front RC panel, it absorbed a considerable amount of the applied blast energy of 58 %. For the back RC panel, it absorbed a negligible average value of 1.5 %. As for the RSR sandwich panel, the sand interlayer dissipated an average value of 51 % of the total energy dissipated by the entire RSR sandwich panel. For the front RC panel, it absorbed an average value of 26 %. For the back RC panel, it absorbed an average value of 23 %. As for the SR, the sand layer dissipated an average value of 90 % of the total energy dissipated by the entire SR protective system. For the back RC panel, it absorbed an average value of 10 %. It noticed that the front RC panel of the RHR sandwich panel dissipated

the largest percentage of the applied energy due to the elastic behavior of the helical springs interlayer. In contrast, due to the plastic behavior of the sand interlayer in the RSR sandwich panel, the sand interlayer absorbed the largest amount of the applied blast energy. On the other hand, the average energy absorbed by the front RC panel of the RHR sandwich panel is 2.3 times that absorbed by the front RC panel of the RSR sandwich panel. In addition, the average energy percentage absorbed by the back RC panel of the RSR sandwich panel is 22 times that absorbed by the back RC panel of the RHR sandwich panel.

These results show that the new proposed RHR sandwich panel can protect the back RC panel from being damaged more than that achieved by the RSR sandwich panel. Accordingly, the RHR sandwich panel can withstand additional blast shot in the case of 1 and 5 Kg TNT without being replaced when compared with the RSR sandwich panel. As for the SR, most of the applied blast energy is absorbed by the sand layer in a form of plastic internal energy by performing plastic compaction between its solid particles. This leads to the early damage of the sand layer when compared with the RSR sandwich panel and accordingly leads to the early failure of the back RC panel by absorbing a considerable amount of energy.

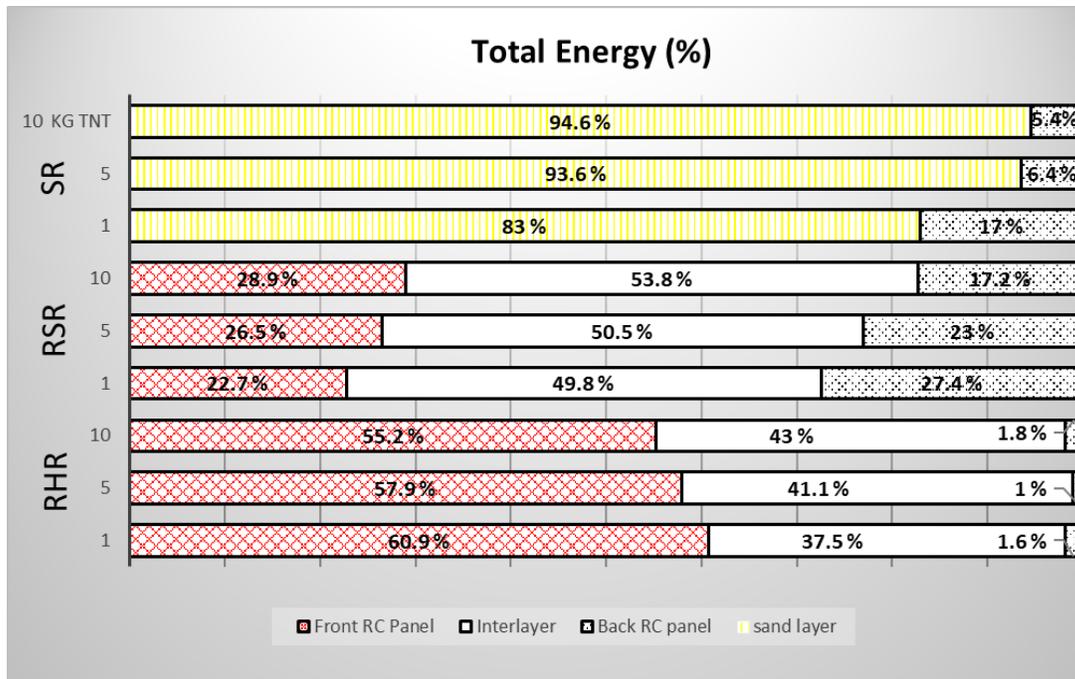


Figure 6.20 Ratio of the total energy dissipated by each component of the SR, RSR and RHR protective systems for the three different blast loads

In addition, the normal stress-time history is analyzed for each protective system to evaluate the reduction percentage between the applied normal stress induced by the blast wave on the adjacent surface of the front panel and that imparted to the upper surface of the back RC panel for each sandwich panel. This study shows the influence of the protective layers in reducing the imparted stresses to the back RC panel. The normal stress-time histories are monitored at the midpoint of the upper surface of the front layer and back RC panel of the SR, RSR and RHR protective systems.

Figures 6.21, 6.22 and 6.23 shows a comparison of the normal stress-time histories at the nominated locations for each sandwich panel under the three blast loading cases. It is found that the RHR sandwich panel outperformed the SR and RSR in reducing the imparted stresses to the

back RC panel. This is attributed to the existence of the helical springs interlayer, which has a significant influence on stress reduction due to its excellent shock absorption and its durability.

For the RHR sandwich panel, the reduction percentages between the maximum normal stress values applied on the front and back RC panels are 91 %, 94 % and 94 % in the blast loading cases of 1, 5 and 10 Kg TNT, respectively. As for the RSR sandwich panel, the maximum normal stress is decreased by 60 %, 69 % and 65 % under the blast loading cases 1, 5 and 10 Kg TNT, respectively. As for the SR, the maximum normal stress is decreased by 25 %, 59 and 61 % under the blast loading cases 1, 5 and 10 Kg TNT, respectively. These results show the failure of the RSR sandwich panel in reducing the imparted normal stresses to the back RC panel with a considerable amount. In addition, these results indicate that the maximum normal stress is reduced significantly when using helical springs as an interlayer instead of the sand layer. Besides, it can be observed that the RSR sandwich panel reduced the maximum normal stress better than that reduced by the SR protective system.

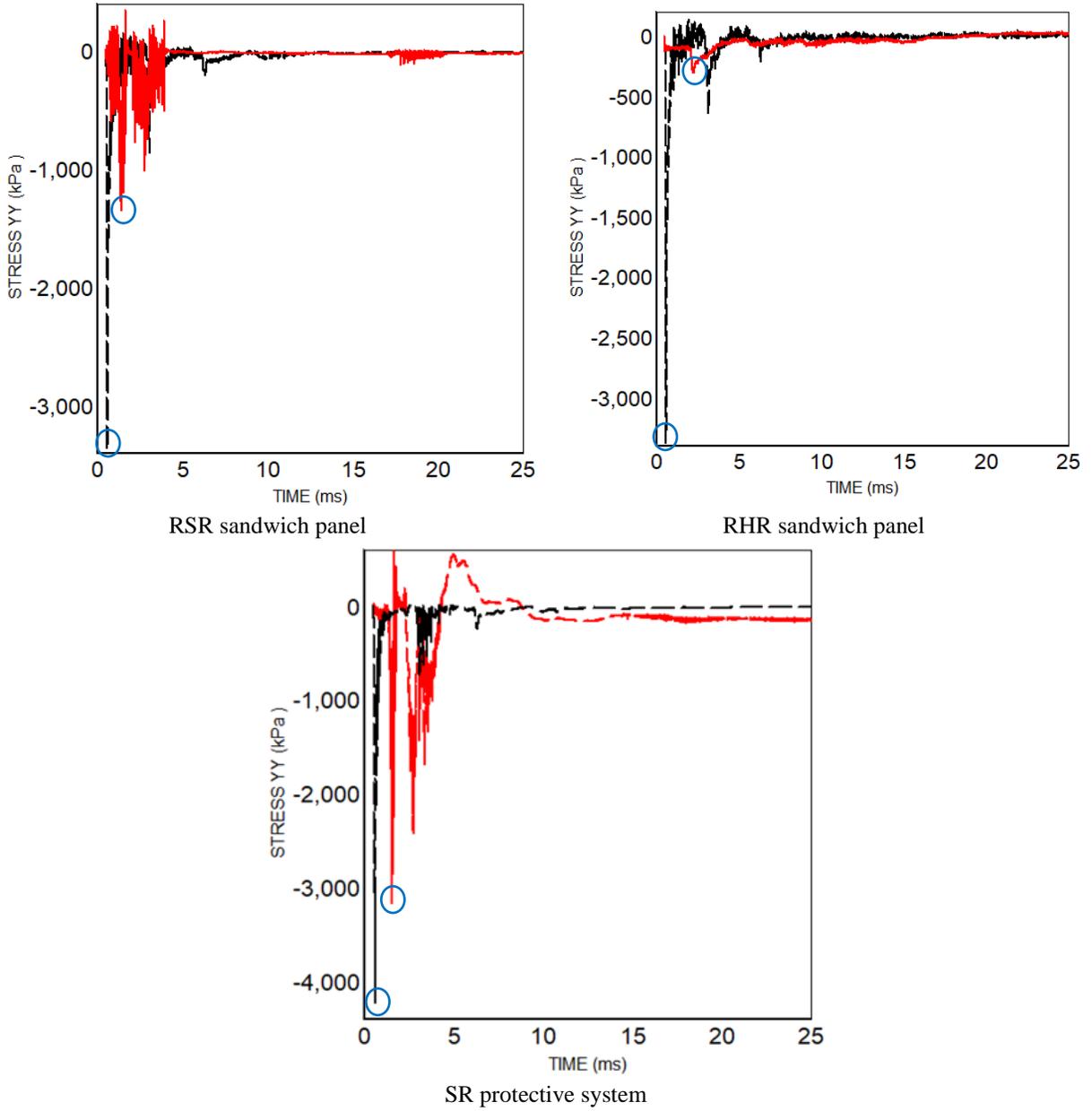


Figure 6.21 Stress time histories at the center of the upper face of the front layer (black color) and back RC panel (red color) for the SR, RSR and RHR systems when subjected to 1 Kg TNT at a SoD of 1 m

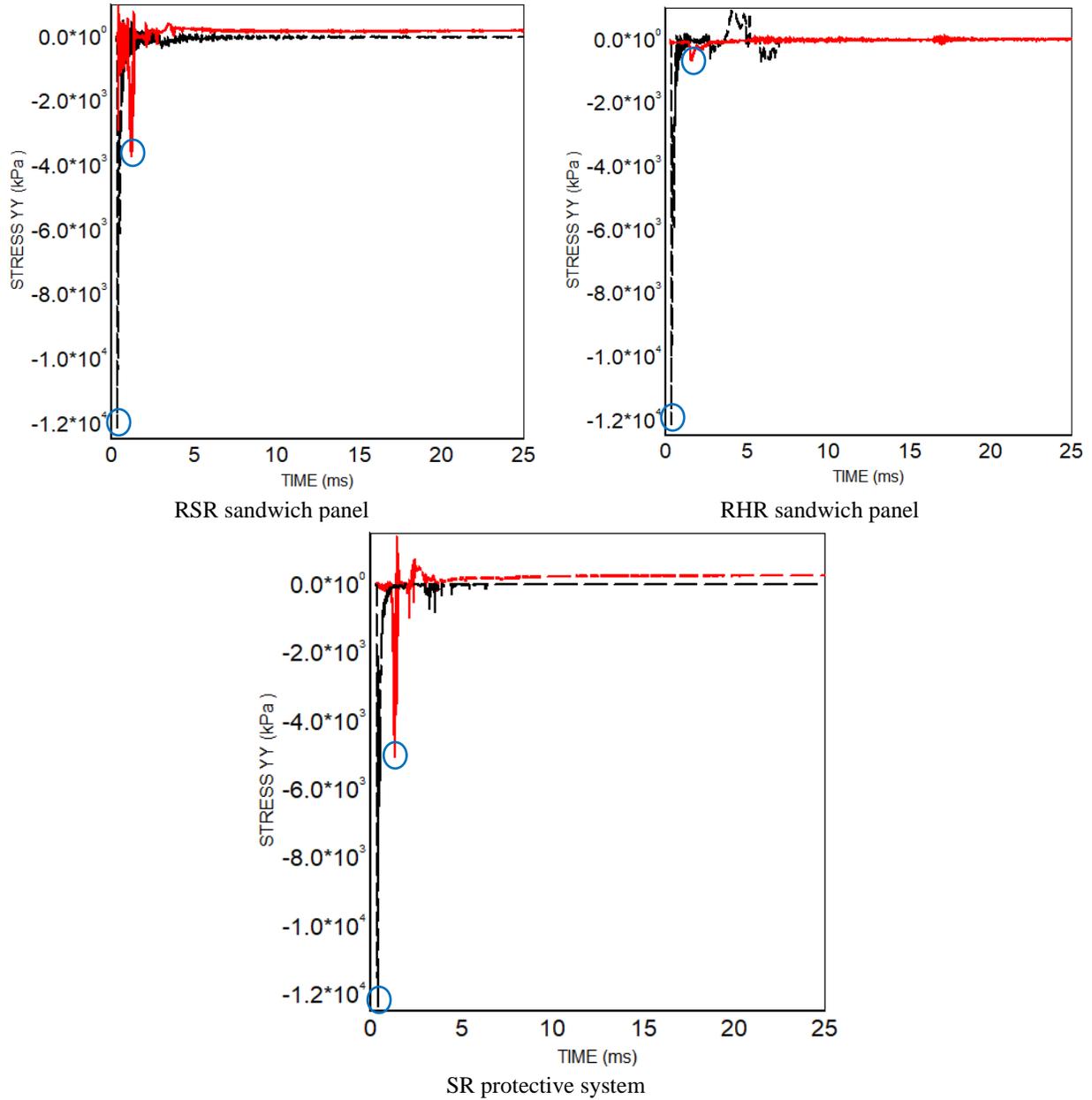


Figure 6.22 Stress time histories at the center of the upper face of the front layer (black color) and back RC panel (red color) for the SR, RSR and RHR systems when subjected to 5 Kg TNT at a SoD of 1 m

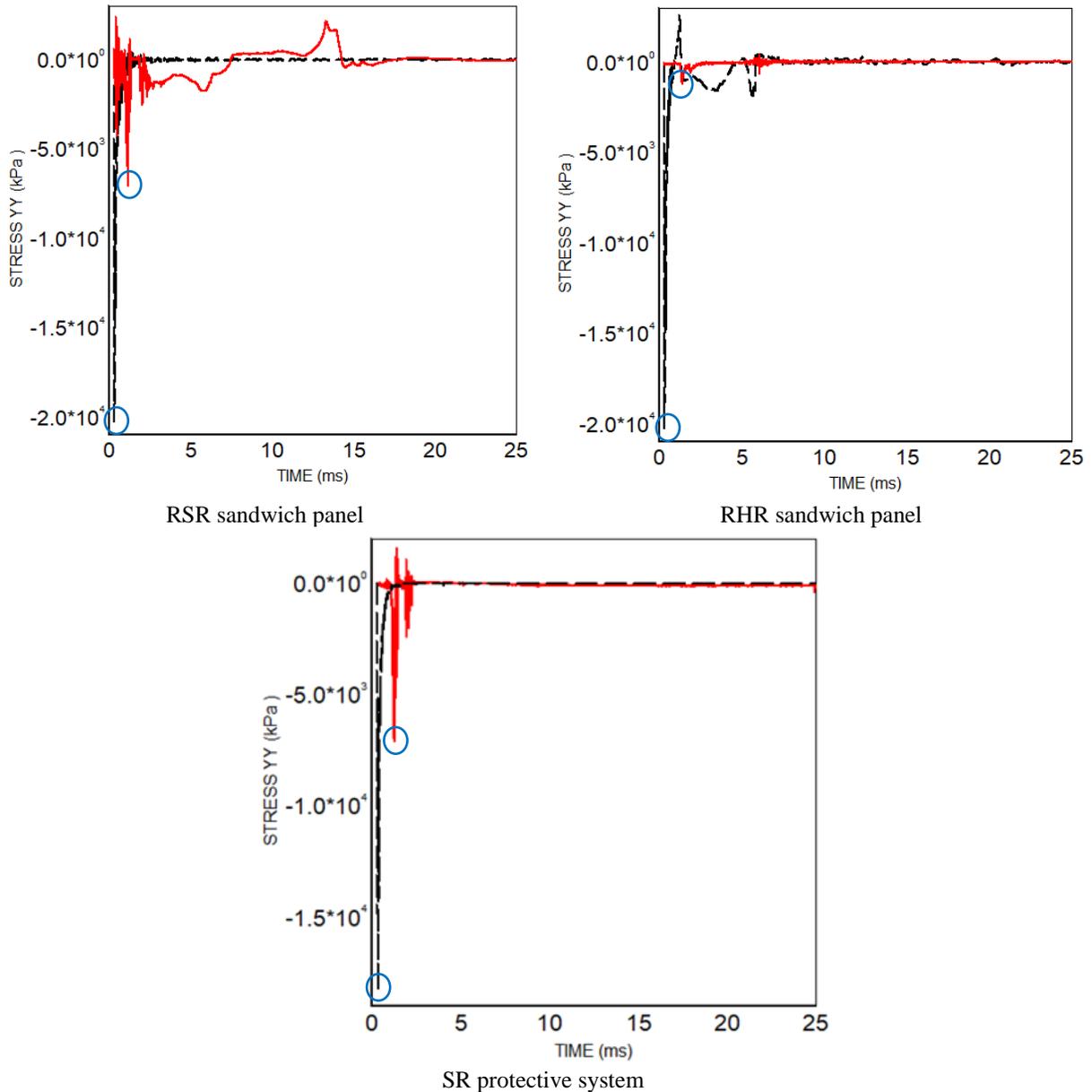


Figure 6.23 Stress time histories at the center of the upper face of the front layer (black color) and back RC panel (red color) for the SR, RSR and RHR when subjected to 10 Kg TNT at a SoD of 1 m

6.4 Summary

RHR sandwich panel is an innovative protective layer developed to protect shallow underground structures. In this Chapter, the blast resistant behavior of the RHR is compared with the SR

protective system and RSR sandwich panel. Detailed finite element models of the SR, RSR and RHR systems are developed. Each system is subjected to three levels of blast loads. RHR provides many advantages to the underground structures: 1) Reduction in weight, where the weight of the RHR is minimum compared to the design deadweight of typical underground structures. Hence, it can be used as either in new construction or as a retrofit to underground structures; 2) Ability to withstand repeated blast loads; 3) ability to be repaired efficiently by replacing only the front RC panel when subjected to high blast loads within the considered range. The result shows that the newly proposed RHR sandwich panel can be used as an effective replacement of the SR and RSR sandwich panel. The results show that the total weight of the two first layers of the RHR sandwich panel is lighter than the sand layer of the SR and the two first layers of the RSR systems by 58 % and 59 %, respectively. The reduction percentage in the plastic work done by the back RC panel of RHR sandwich panel is 99.7 %, 98 % and 73 %, respectively, when compared with the RSR sandwich panel while it is 99.8 %, 98 % and 66 %, respectively when compared with the SR protective system. In addition, the RHR sandwich panel dissipated a considerable amount of the applied energy in the form of elastic internal energy, which released again after reaching its maximum displacement. On the contrary, the RSR and SR systems dissipated the applied energy in the form of plastic internal energy, which accordingly allows a considerable amount of energy to be imparted to the back RC panel and absorbed as plastic internal energy. These results emphasize the crucial role of the helical springs interlayer in protecting the back RC panel from being damaged by decreasing the amount of the imparted blast energy transmitted to the back RC panel. In addition, the results show the important role of the front RC panel, in the case of RSR, which decreases the amount of energy absorbed by the sand layer and consequently, delaying the

entire failure of the sand layer, when compared with the behavior of the sand layer of the SR protective system which exposed directly to the blast load.

Chapter 7: Parametric study on the performance of the RHR under free air blast loads

In Chapters 3 and 5, the blast resistant capability of the newly proposed RHR sandwich panel is verified. In addition, in Chapter 6, the performance of the RHR over the SR and RSR systems is compared. In this Chapter, a comprehensive parametric study on the design of the RHR interlayer is presented.

7.1 Parametric study factors

In Chapter 3, the experimental observation shows the influence of changing the whole stiffness of the helical springs interlayer on the damage pattern of the RHR sandwich panel against blast loads and the maximum displacement of the front RC panel. In Chapter 5, the numerical results agree well with the experimental findings of the important role of the helical springs interlayer. In addition, the numerical analysis shows the significant effect of helical springs on mitigating the imparted blast loads to the back RC panel by absorbing a considerable amount of the applied blast energy in the form of elastic internal energy. In chapter 6, the comparison between the behavior of the SR, RSR and RHR protective systems shows the important role of the helical springs interlayer on controlling the energy dissipation process. This can be explained as the helical springs interlayer stores a portion of the applied energy in the form of elastic internal energy, which accordingly enforces the front RC panel to gain a considerable amount of kinetic energy and a portion in the form of internal energy. Consequently, this energy dissipation methodology delays the damage of the front and back RC panels. In contrast, the front RC panel in the case of the RSR sandwich panel absorbs a small amount of the applied energy and most of the applied energy is absorbed by

the sand interlayer. In addition, the back RC panel suffers severe damage due to the early failure of the sand interlayer after absorbing a considerable amount of the applied energy. This is attributed to the different nature of the sand and helical springs interlayer.

Due to the important role of the helical springs interlayer, this Chapter focuses on the performance of the interlayer, which consists of various numbers of compression helical springs. As mentioned above, the main factor, which affects the behavior of the helical springs interlayer, is its whole stiffness. Accordingly, this parametric study is applied by changing the whole stiffness of the helical springs interlayer under different scaled distance. As known, any helical spring has many specifications that control its stiffness. One of the main parameters that have a significant influence on the stiffness is the spring wire diameter. Hence, different wire diameters of 10 mm, 15 mm and 20 mm with individual stiffness of 7.72 N/mm, 43.59 N/mm and 156.77 N/mm, respectively, are used in this study.

It is simply observed that a small increase in the wire diameter causes a considerable increase in the stiffness. For example, in the case of the RHR sandwich panel with 16 helical springs located in the interlayer, when the wire diameter of helical springs changed from 20 mm to 15 mm, the whole stiffness of the core layer decreased by 72 % and the whole core weight by 42 %. It is obvious that decreasing the wire diameter of each helical spring by 5 mm makes a significant reducing in its spring stiffness. In addition to changing the wire diameter, the number of the helical springs are changed. The numbers of helical spring used in this study are 7, 9, 16 and 25 helical springs. Besides, different blast loads of 1, 5 and 10 Kg TNT at a SoD of 1 m are used in this study to investigate the performance of the RHR sandwich panel under a different scaled distance of 1

$\text{m/Kg}^{1/3}$, $0.58 \text{ m/Kg}^{1/3}$ and $0.46 \text{ m/Kg}^{1/3}$. The helical springs are located as an array for each specimen, as shown in Figure 7.1. Thirty-six finite element models are created for this parametric study. Table 7.1 shows the outlines of this parametric study. Each sandwich panel is named according to the number of helical springs located in the interlayer, the wire diameter of the spring coil and the blast weight applied at a fixed SoD of 1 m, respectively. For instance, RHR-7-10-1 refers to the RHR sandwich panel, which has 7 helical springs in the interlayer. The wire diameter of these springs is 10 mm and the scaled distance is $1 \text{ m/Kg}^{1/3}$ which is calculated from detonating 1 Kg TNT blast weight at a SoD of 1 m from the center of the front RC panel of the RHR sandwich panel. The maximum allowable displacements for helical spring with wire diameters of 10, 15 and 20 mm are 187.5, 156.25 and 125 mm, respectively.

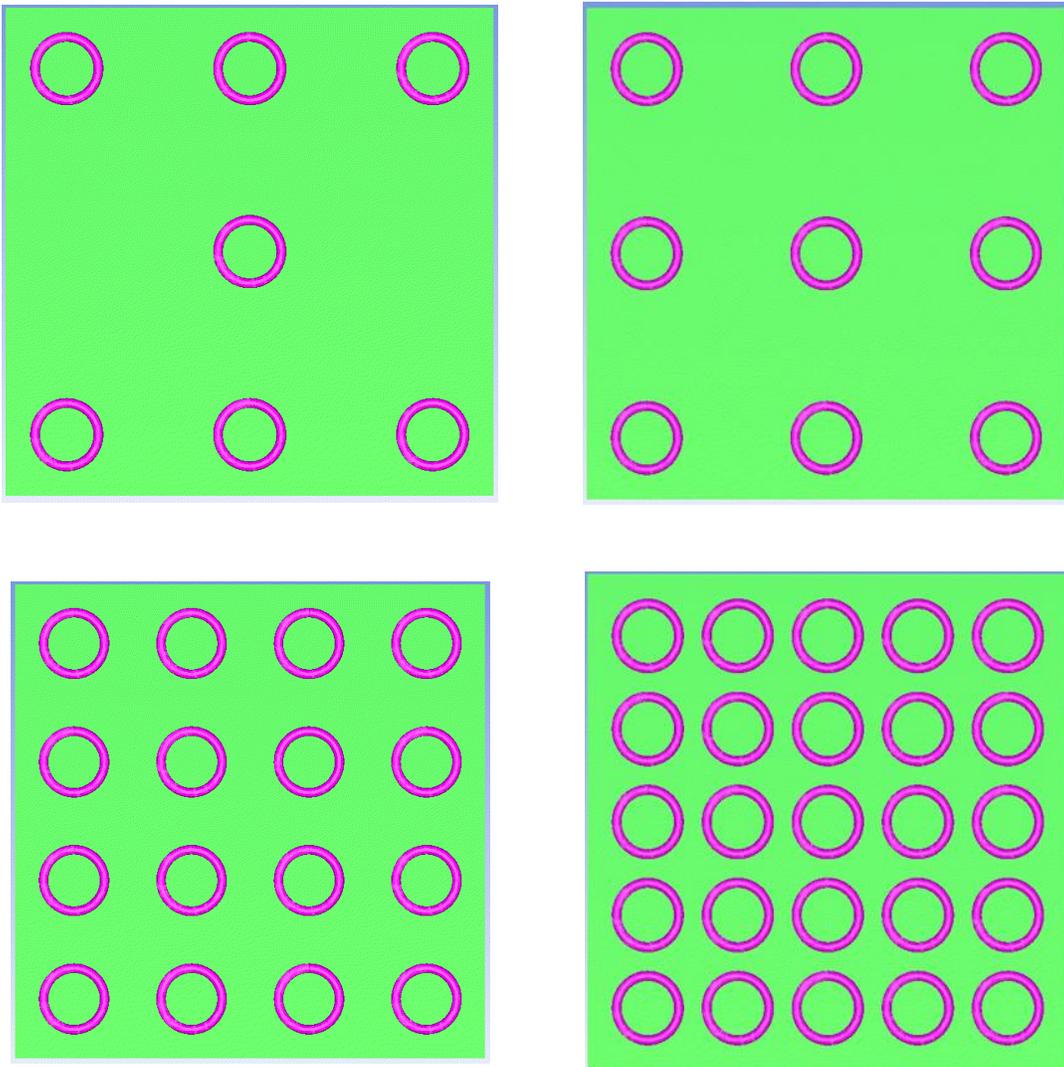


Figure 7.1 Different helical spring arrangements used in the parametric study

Table 7.1 Outlines of the RHR sandwich panel parameters used in this study

No.	Name	Number of helical springs	Wire Diameter (mm)	Blast weight (Kg)	Interlayer weight (Kg)	Interlayer stiffness (N/mm)
1	RHR-7-10-1	7	10	1	13	54
2	RHR-7-10-0.58			5		
3	RHR-7-10-0.46			10		
4	RHR-7-15-1		15	1	27	305
5	RHR-7-15-0.58			5		
6	RHR-7-15-0.46			10		
7	RHR-7-20-1		20	1	47	1097
8	RHR-7-20-0.58			5		
9	RHR-7-20-0.46			10		
10	RHR-9-10-1	9	10	1	16	70
11	RHR-9-10-0.58			5		
12	RHR-9-10-0.46			10		
13	RHR-9-15-1		15	1	35	392

14	RHR-9-15-0.58			5		
15	RHR-9-15-0.46			10		
16	RHR-9-20-1			1		
17	RHR-9-20-0.58		20	5	60	1411
18	RHR-9-20-0.46			10		
19	RHR-16-10-1			1		
20	RHR-16-10-0.58		10	5	29	124
21	RHR-16-10-0.46			10		
22	RHR-16-15-1			1		
23	RHR-16-15-0.58	16	15	5	62	698
24	RHR-16-15-0.46			10		
25	RHR-16-20-1			1		
26	RHR-16-20-0.58		20	5	107	2508
27	RHR-16-20-0.46			10		
28	RHR-25-10-1	25	10	1	45	193

29	RHR-25-10-0.58			5		
30	RHR-25-10-0.46			10		
31	RHR-25-15-1			1		
32	RHR-25-15-0.58		15	5	97	1090
33	RHR-25-15-0.46			10		
34	RHR-25-20-1			1		
35	RHR-25-20-0.58		20	5	167	3919
36	RHR-25-20-0.46			10		

7.2 Numerical results and discussion

In this section, the results obtained from the numerical parametric study are presented and discussed. The results are expressed in the form of the maximum displacement of the front RC panel, the maximum energy absorbed by the components of the RHR sandwich panel. These results show the effect of changing the interlayer stiffness on the behavior of the RHR sandwich panel. In this study, the total stiffness of the interlayer is changed by changing the number of helical springs located in the interlayer and changing the wire diameter of the spring coil. Figure 7.2 shows the effect of changing the wire diameter and the number of helical springs on the total stiffness of the interlayer. Figure 7.3 shows the relationship between the interlayer weight and the total stiffness of the interlayer. It is observed that a small increase in interlayer weight causes a significant increase in total interlayer stiffness. For each number of helical springs, when the weight of the interlayer increases by 117 % and 271 %, the total stiffness of the interlayer increases by 465 % and 1931 %, respectively. These results emphasize that the helical springs interlayer can provide high strength by adding a small weight. Accordingly, it fulfills the main concept of this research: high strength low weight layer.

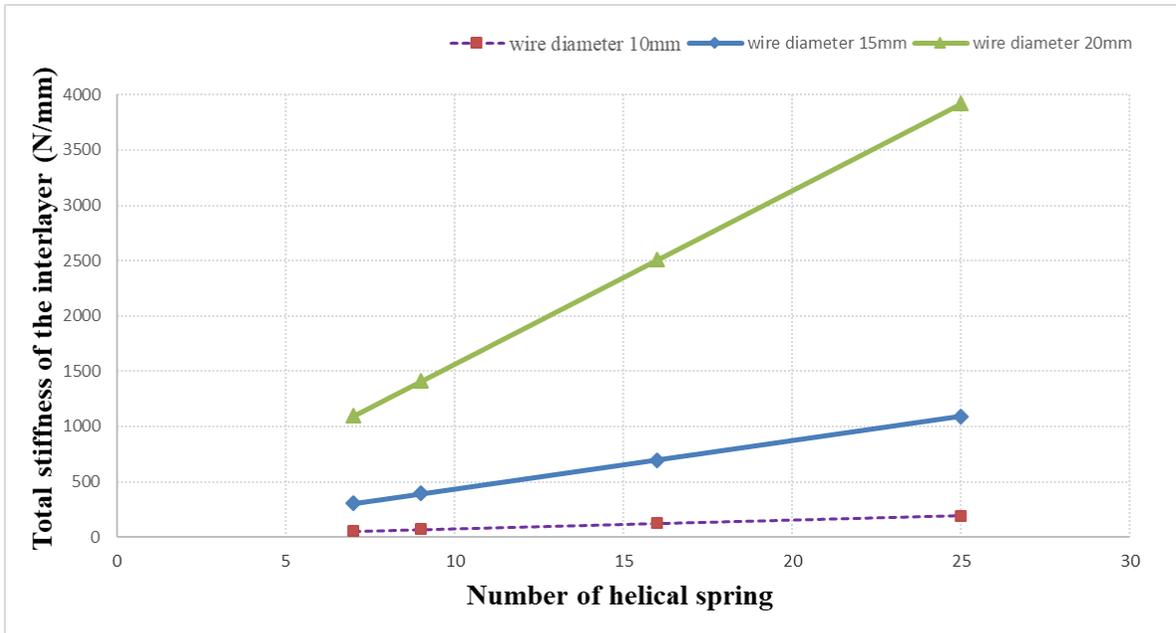


Figure 7.2 Effect of changing the wire diameter and the number of helical springs on the total stiffness of the interlayer

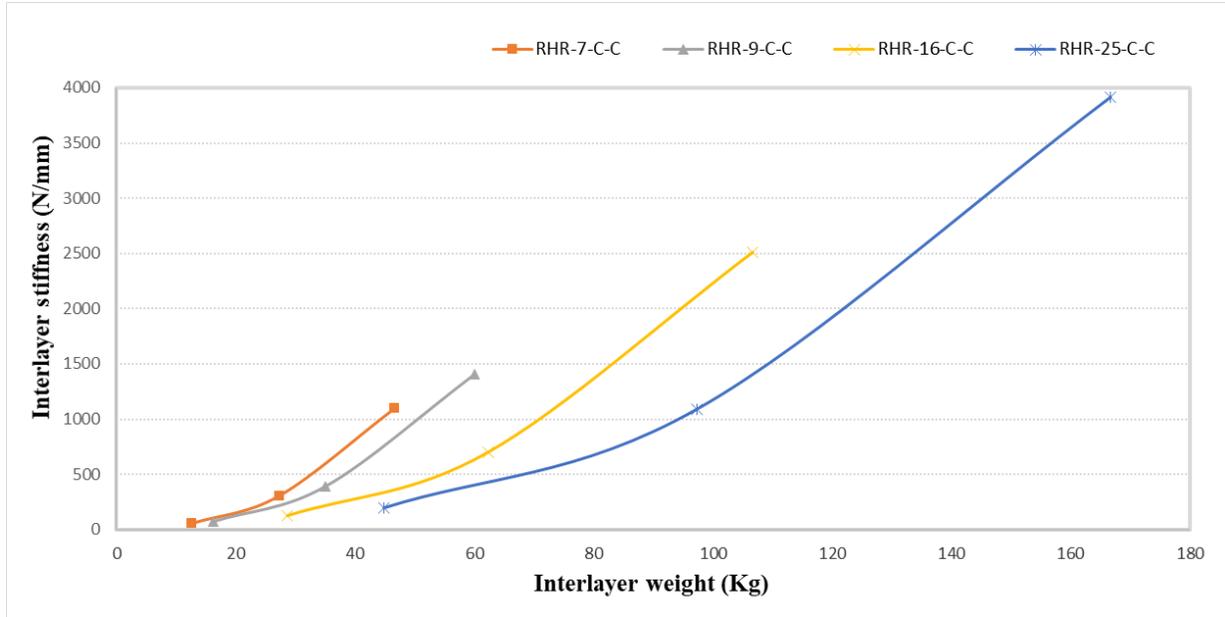


Figure 7.3 Effect of changing the interlayer weight on the total stiffness of the interlayer

7.2.1 Displacement analysis

In this section, the displacement of the front RC panel of the RHR sandwich panel is studied by changing the wire diameter of helical springs located in the interlayer, the number of helical springs and the scaled distance. The numerical results show the effect of changing the wire diameter and changing the number of helical springs on the maximum displacement of the front RC panel under different scaled distances of 1, 0.58 and 0.46 m/Kg^{1/3}.

Figure 7.4 shows the relationship between the displacement of the front RC panel and the wire diameter of the helical springs when using different numbers of helical springs in the interlayer and changing the scaled distance. Notice that, C is referred to Changeable value of the wire diameter. For example, RHR-7-C-1 means RHR with 7 helical springs and different wire diameters of 10, 15 and 20 mm under a scaled distance of 1 m/Kg^{1/3}. It is generally observed that changing the wire diameter of the helical spring located in the interlayer significantly affects the displacement of the front RC panel, as shown in Figure 7.4.

For RHR-7 under a scaled distance of 1 m/Kg^{1/3}, the reduction percentages of the maximum displacement of the front RC panel when using wire diameters of 10, 15 and 20 mm are 0 %, 58 % and 77 %, respectively. Whereas under a scaled distance of 0.58 m/Kg^{1/3}, the reduction percentages of the maximum displacement when using 10, 15 and 20 mm wire diameters are 0 %, 49 % and 71 %, respectively. Whereas under a scaled distance of 0.46 m/Kg^{1/3}, the reduction percentages of the maximum displacement when using 10, 15 and 20 mm wire diameters are 0 %, 27 % and 53 %, respectively.

For RHR-9 under a scaled distance of $1 \text{ m/Kg}^{1/3}$, the reduction percentages of the maximum displacement when using 10, 15 and 20 mm wire diameters are 0 %, 58 % and 77 %, respectively. Whereas under a scaled distance of $0.58 \text{ m/Kg}^{1/3}$, the reduction percentages of the maximum displacement when using 10, 15 and 20 mm wire diameters are 0 %, 54 % and 74 %, respectively. Whereas under a scaled distance of $0.46 \text{ m/Kg}^{1/3}$, the reduction percentages of the maximum displacement when using 10, 15 and 20 mm wire diameters are 0 %, 28 % and 57 %, respectively.

For RHR-16 under a scaled distance of $1 \text{ m/Kg}^{1/3}$, the reduction percentages of the maximum displacement when using 10, 15 and 20 mm wire diameters are 0 %, 66 % and 78 %, respectively. Whereas under a scaled distance of $0.58 \text{ m/Kg}^{1/3}$, the reduction percentages of the maximum displacement when using 10, 15 and 20 mm wire diameters are 0 %, 60 % and 77 %, respectively. Whereas under a scaled distance of $0.46 \text{ m/Kg}^{1/3}$, the reduction percentages of the maximum displacement when using 10, 15 and 20 mm wire diameters are 0 %, 44 % and 69 %, respectively.

For RHR-25 under a scaled distance of $1 \text{ m/Kg}^{1/3}$, the reduction percentages of the maximum displacement when using 10, 15 and 20 mm wire diameters are 0 %, 62 % and 80 %, respectively. Whereas under a scaled distance of $0.58 \text{ m/Kg}^{1/3}$, the reduction percentages of the maximum displacement when using 10, 15 and 20 mm wire diameters are 0 %, 59 % and 78 %, respectively. Whereas under a scaled distance of $0.46 \text{ m/Kg}^{1/3}$, the reduction percentages of the maximum displacement when using 10, 15 and 20 mm wire diameters are 0 %, 59 % and 77 %, respectively.

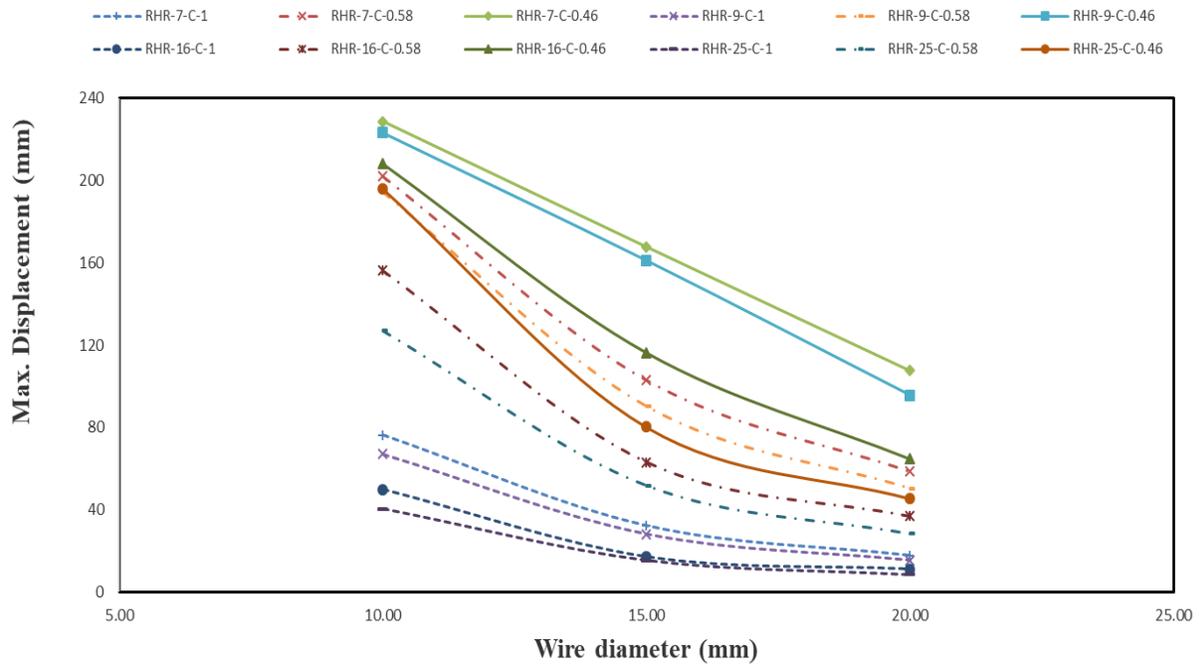


Figure 7.4 Relationship between the front RC panel displacements and wire diameters when using different numbers of helical springs under different scaled distance of 1, 0.58 and 0.46 m/Kg^{1/3}

Figure 7.5 shows the relationship between the reduction percentage of the maximum displacement of the front RC panel and the scaled distance for each number of helical springs using different wire diameters. Notice that, in Figure 7.5, C is referring to the Changeable value of the number of helical springs. This can be explained that as the scaled distance increases, the intensity of the applied load increases which makes the load more impulsive. In general, it can be observed that the reduction percentage of the maximum displacement of the front RC panel decreases by decreasing the scaled distance except for the case of 25 helical springs, in which the reduction percentages are almost the same for the three scaled distance considered, as shown in Figure 7.5. For 7 helical springs, the average reduction value of the maximum displacement for the wire diameter of 15 mm and 20 mm is 44.5 % and 67 %, respectively, with respect to the wire diameter

of 10 mm. For 9 helical springs, the average reduction value of the maximum displacement for wire diameter 15 mm and 20 mm is 45 % and 69 %, respectively. For 16 helical springs, the average reduction value of the maximum displacement for wire diameter 15 mm and 20 mm is 56.5 % and 74 %, respectively. Whereas for 25 helical springs, the average reduction value of the maximum displacement for wire diameter 15 mm and 20 mm is 60 % and 78 %, respectively. Accordingly, the best number of helical springs which can be used as an interlayer for the RHR sandwich panel under the studied range of scaled distance is 25 as in this case the reduction percentage of the maximum displacement of the front RC panel is more than that in the cases of 16, 9 and 7 helical springs, respectively.

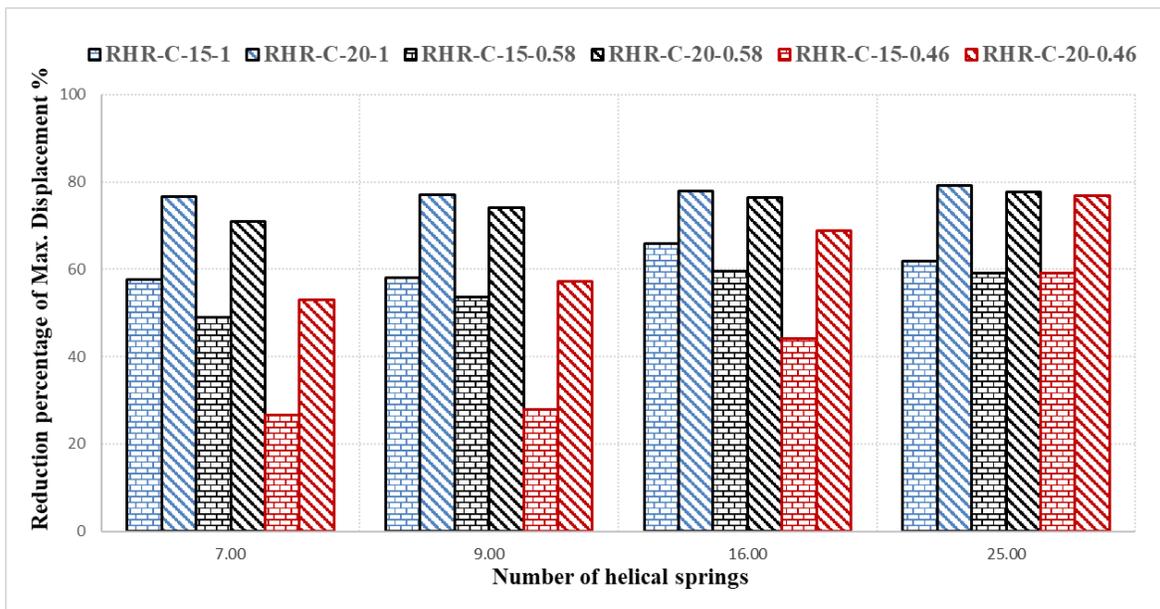


Figure 7.5 Effect of changing the scaled distance on the reduction percentage of the maximum displacement of the front RC panel using different numbers of helical springs with different wire diameters

Figure 7.6 shows the relationship between the front RC panel displacements and the total stiffness of the helical springs interlayer under different scaled distances of 1, 0.58 and 0.46 m/Kg^{1/3}. In

general, it can be observed that the maximum displacement of the front RC panel decreases significantly as the interlayer stiffness increases until reaching a certain stiffness value of about 698 N/mm. After that, any increase in the interlayer stiffness causes a small decrease in the maximum displacement as shown in the figure below. From Figure 7.6, the best interlayer stiffnesses, which give proper maximum displacements, under the range of scaled distance considered, is almost between 700 to 1400 N/mm. These stiffness values are based on the considered helical springs in this study, which can be easily found in the market. The importance of including the maximum displacement in the design is to avoid reaching the closed length of the helical springs, which can result in an increase in the plastic work done by the back panel and it might lead to permanent damage to the body of the helical springs. Accordingly, it is recommended to check the maximum displacement value after designing the helical springs interlayer. The maximum displacement of the front RC panel for each RHR system is presented in Table 7.2.

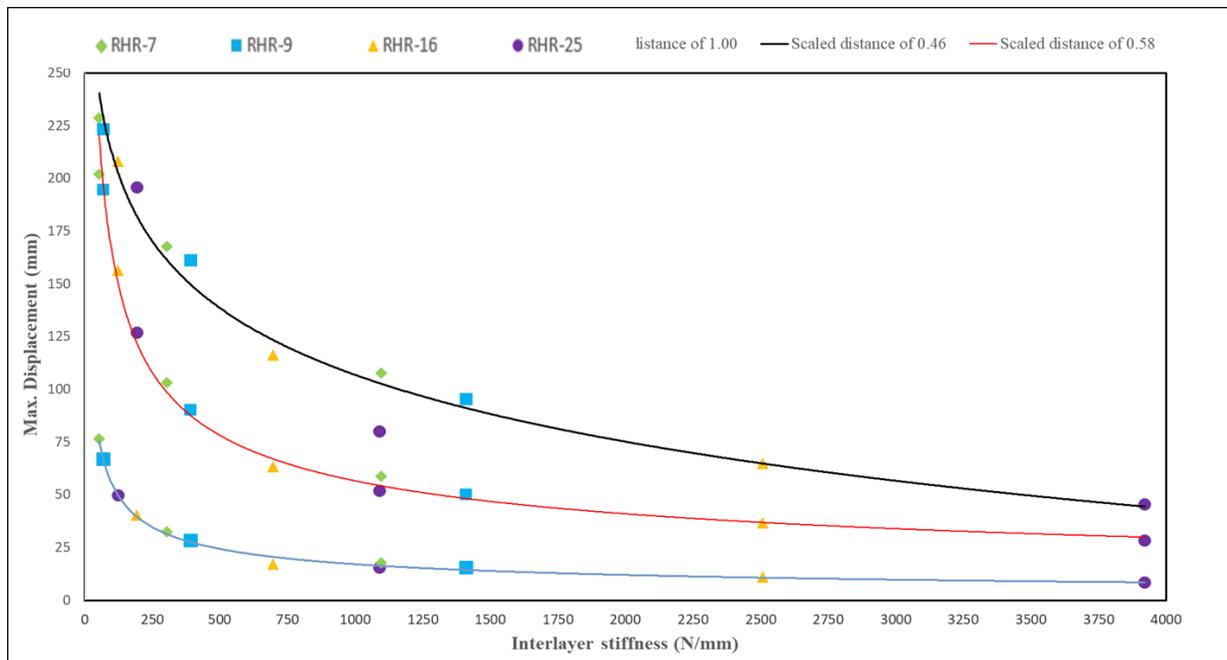


Figure 7.6 Relationship between the maximum displacements of the front RC panel and total stiffness of the interlayer under different scaled distance of 1, 0.58 and 0.46 m/Kg^{1/3}

7.2.2 Energy dissipation analysis

In this section, the energy dissipated by each component of the RHR sandwich panel is evaluated by changing the same parameters mentioned in the previous section. The total energy dissipated by the front RC panel, helical springs interlayer and the back RC panel is presented to investigate the effect of changing the core parameters on the RHR sandwich panel performance. The total energy here is the sum of the internal and kinetic energy gained by the component. Table 7.2 shows the maximum total energy dissipated by each component of the 36 RHR sandwich panel and presents the plastic work done by the front and back RC panel for each sandwich panel. Besides, this table shows which helical springs interlayer reached the closed length. Notice that the red color presented on some cells of the table indicates that the RC panel is totally damaged, where the DL exceeded 0.8 according to the damage level categorization mentioned in Chapter 4.

Table 7.2 The numerical results for the RHR sandwich panel

No.	Name	Maximum total energy dissipated (J)			Plastic work (J)		Maximum displacement (mm)	Closed length of helical spring
		Front RC panel	Helical springs interlayer	Back RC panel	Front RC panel	Back RC panel		
1	RHR-7-10-1	325.36	232.79	6.53	9.44	0.09	76.28	
2	RHR-7-10-0.58	3315.30	2182.73	181.21	246.36	67.45	202.02	Reached
3	RHR-7-10-0.46	9293.00	4959.93	1019.80	1417.00	560.82	228.68	Reached
4	RHR-7-15-1	319.91	283.00	3.31	8.58	0.04	32.25	
5	RHR-7-15-0.58	3251.70	2463.94	25.09	197.66	5.70	102.94	
6	RHR-7-15-0.46	9153.80	6810.15	513.71	831.95	304.54	167.71	Reached
7	RHR-7-20-1	314.32	199.46	6.24	8.69	0.99	17.76	
8	RHR-7-20-0.58	3258.80	2167.72	39.03	204.72	14.77	58.50	
9	RHR-7-20-0.46	9636.5	7099.35	152.47	479.19	95.21	107.54	
10	RHR-9-10-1	324.50	236.28	6.63	9.26	0.07	67.05	
11	RHR-9-10-0.58	3302.70	2206.75	94.62	221.72	19.78	194.47	Reached
12	RHR-9-10-0.46	9247.70	5179.63	937.45	1386.4	495.23	223.30	Reached

13	RHR-9-15-1	317.43	282.40	3.47	8.23	0.03	28.18	
14	RHR-9-15-0.58	3218.10	2517.05	24.51	195.08	0.04	90.13	
15	RHR-9-15-0.46	9062.80	7230.60	178.39	513.15	88.46	161.11	Reached
16	RHR-9-20-1	309.04	194.81	6.05	0.01	0.008	15.41	
17	RHR-9-20-0.58	3199.00	2174.42	33.11	4.82	3.62	50.17	
18	RHR-9-20-0.46	9469.10	7132.98	157.36	273.39	257.24	95.52	
19	RHR-16-10-1	321.54	221.77	6.34	8.59	0.06	51.19	
20	RHR-16-10-0.58	3256.80	2176.33	47.24	189.63	9.54	156.14	
21	RHR-16-10-0.46	9085.30	5741.08	1181.10	728.43	611.38	208.06	Reached
22	RHR-16-15-1	308.70	286.14	3.21	6.84	0.006	16.97	
23	RHR-16-15-0.58	3099.30	2596.77	25.00	185.83	2.23	63.08	
24	RHR-16-15-0.46	8737.50	7126.31	64.50	391.96	11.08	116.25	
25	RHR-16-20-1	294.47	181.14	6.47	6.26	0.26	11.00	
26	RHR-16-20-0.58	2999.40	2130.58	37.86	187.54	7.85	36.70	
27	RHR-16-20-0.46	8893.70	6916.93	220.15	441.66	118.24	64.64	

28	RHR-25-10-1	318.83	230.79	6.94	5.81	0.007	40.28	
29	RHR-25-10-0.58	3216.00	2304.24	49.94	176.15	1.64	127.03	
30	RHR-25-10-0.46	8897.30	6540.24	1325.90	724.61	355.52	195.90	Reached
31	RHR-25-15-1	298.25	244.55	5.27	5.52	0.01	15.37	
32	RHR-25-15-0.58	2951.80	2485.67	32.71	167.10	2.08	51.78	
33	RHR-25-15-0.46	8333.30	6984.21	88.71	383.39	12.77	80.11	
34	RHR-25-20-1	277.40	169.92	8.93	4.74	0.06	8.43	
35	RHR-25-20-0.58	2761.70	2046.26	73.41	162.41	26.58	28.24	
36	RHR-25-20-0.46	8230.30	5855.97	1802.7	451.65	553.22	45.38	

Figures 7.7, 7.8, 7.9 and 7.10 show the relationship between the plastic work done by the front RC panel and back RC panels and the variation of the interlayer stiffness under the considered range of scaled distance.

In the case of RHR-7, the plastic work done by the front and back RC panels is decreased by increasing the interlayer stiffness except for the back RC panel in the case of the scaled distance of $0.46 \text{ m/Kg}^{1/3}$, where the plastic work begins to increase slightly. It can be observed that the best interlayer stiffness range is 800 to 1100 N/mm for the scaled distance range considered. In the case of RHR-9, the plastic work done by the front and back RC panels is decreased by increasing the interlayer stiffness except for the back RC panel in the case of the scaled distance of $0.46 \text{ m/Kg}^{1/3}$, where the plastic work begins to increase considerably. Accordingly, the best interlayer stiffness range can be considered between 250 to 900 N/mm. As for the RHR-16, the plastic work done by the front and the back RC panels decreases by increasing the interlayer stiffness except for the case of the scaled distance of $0.46 \text{ m/Kg}^{1/3}$, in which the front and back RC panels start to considerably increase after reaching a certain value of the interlayer stiffness. It can be observed that the best range for the interlayer stiffness is between 700 to 1400 N/mm. In the case of RHR-25, the plastic work done by the back panel significantly increases after reaching a certain value of the interlayer stiffness under the scaled distance of $0.46 \text{ m/Kg}^{1/3}$. This is attributed to the full damage of the front RC panel in the case of the scaled distance of $0.46 \text{ m/Kg}^{1/3}$, which allows excessive blast loads to be imparted to the back RC panel, which results in an increase in the plastic work done by the back RC panel. Accordingly, the best range for the interlayer stiffness can be considered between 800 and 1400 N/mm for the scaled distance considered.

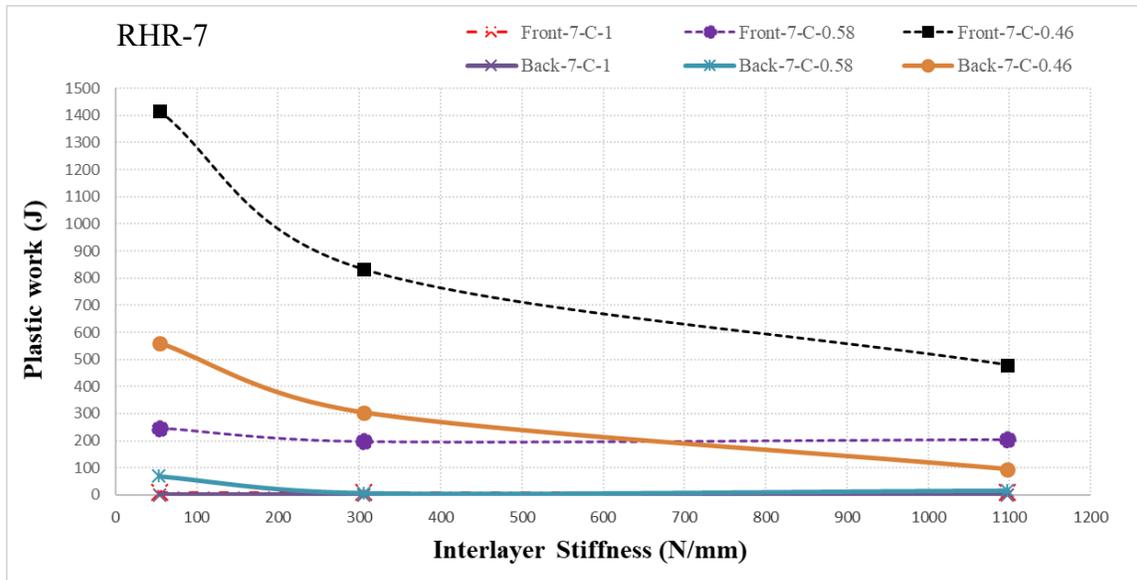


Figure 7.7 Relationship between the plastic work done by the front and back RC panel of the RHR-7 and the interlayer stiffness under the three scaled distance of 0.46, 0.58 and 1 m/Kg^{1/3}

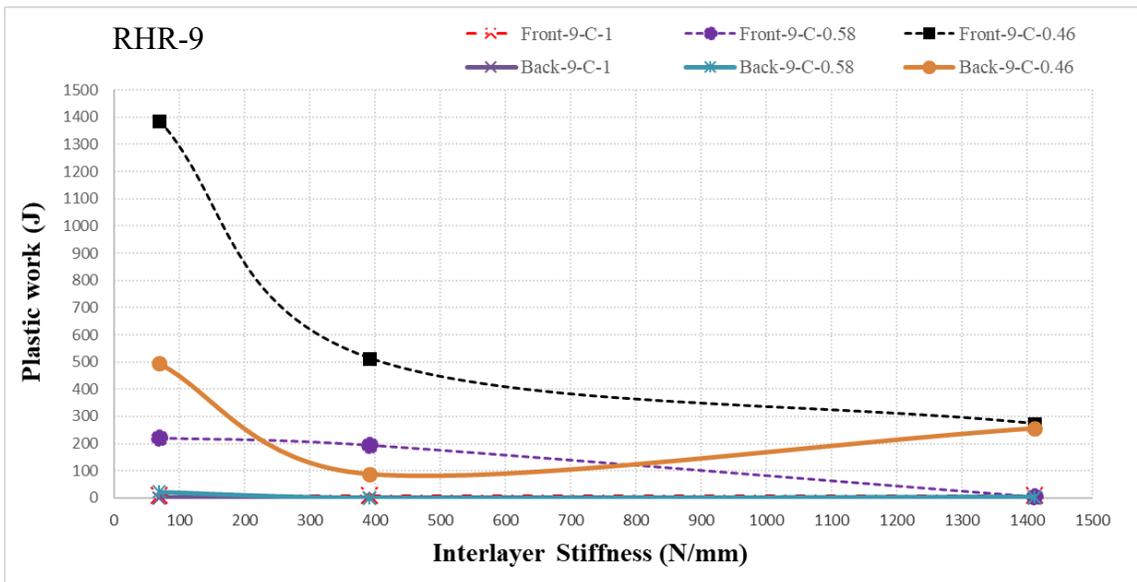


Figure 7.8 Relationship between the plastic work done by the front and back RC panel of the RHR-9 and the interlayer stiffness under the three scaled distance of 0.46, 0.58 and 1 m/Kg^{1/3}

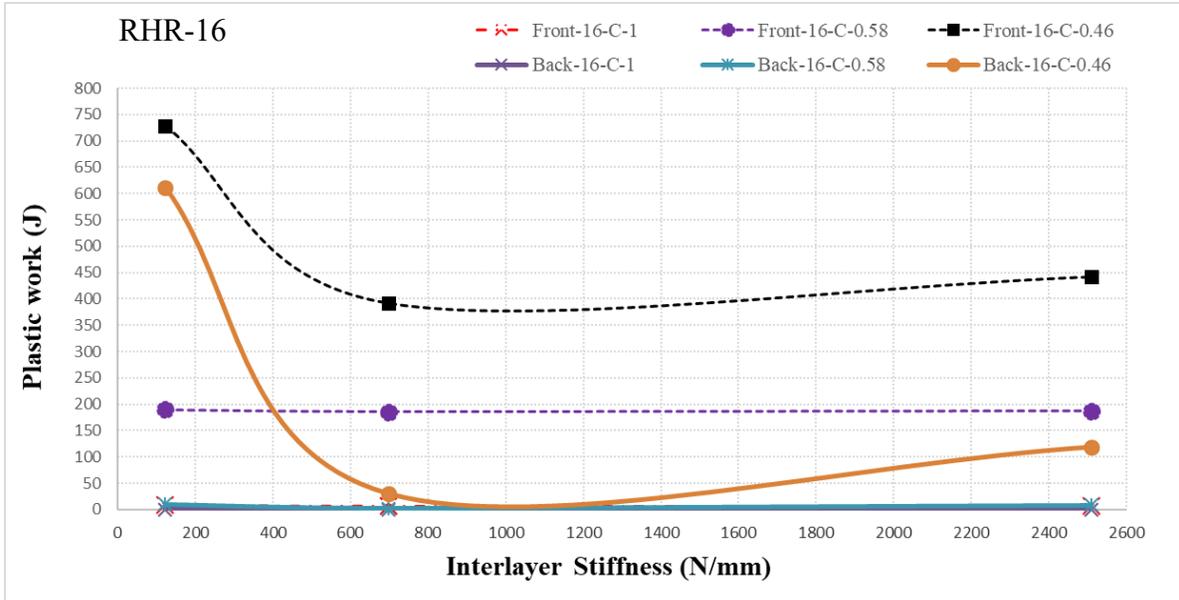


Figure 7.9 Relationship between the plastic work done by the front and back RC panel of the RHR-16 and the interlayer stiffness under the three scaled distance of 0.46, 0.58 and 1 m/Kg^{1/3}

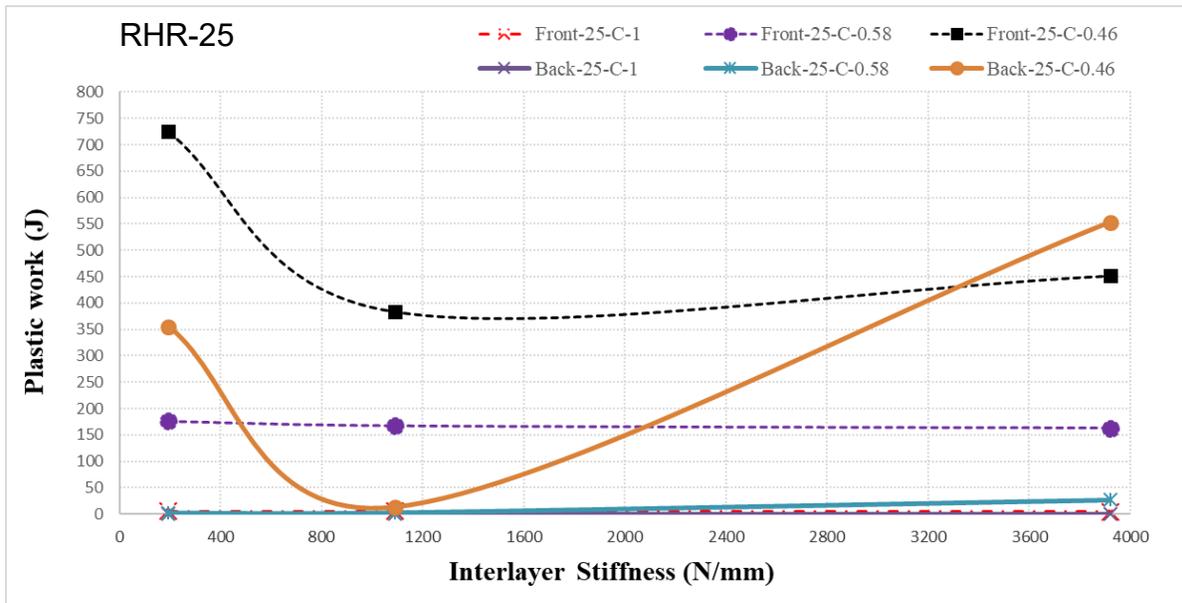


Figure 7.10 Relationship between the plastic work done by the front and back RC panel of the RHR-25 and the interlayer stiffness under the three scaled distance of 0.46, 0.58 and 1 m/Kg^{1/3}

From table 7.2, it can be observed that the maximum total energy dissipated by the front RC panel of the studied RHR sandwich panels absorbed a considerable amount of the applied blast energy with an average of 58 % of the total energy dissipated by the three components (front RC panel, Helical springs interlayer and the back RC panel). As for the helical springs interlayer, it absorbed an average value of 40.5 % and for the back RC panel, it absorbed a negligible amount of the applied blast energy of an average of 2 %. Accordingly, the average value of the total energy absorbed by the front RC panel and the helical springs interlayer is 98 % of the entire applied energy value. These results show the significant role of the helical springs interlayer which directed a considerable amount of energy to the front RC panel and absorbed a considerable portion of the imparted blast energy in a form of internal energy, which released after reaching the maximum displacement. Finally, a small amount of energy imparted to the back RC panel. Figure 7.11 shows the total absorbed energy by each component of the studied RHR sandwich panels under different scaled distance.

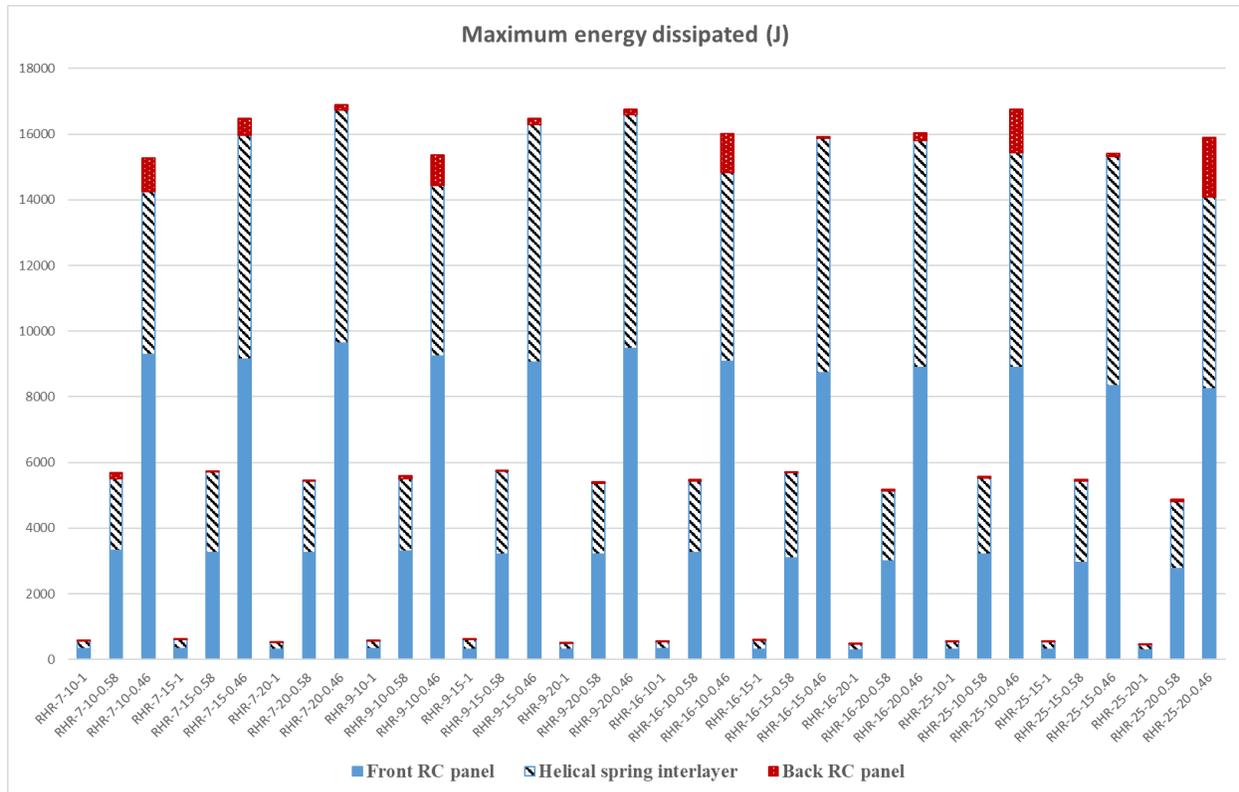


Figure 7.11 Total energy dissipated by Front RC panel, helical springs interlayer and back RC panel under three different scaled distance

After calculating the helical springs interlayer stiffness according to the designed blast load, Figure 7.6 should be used to ensure that the close length of the helical springs is not reached under the maximum displacement of the front RC panel. After that, designers can use Figures 7.7 to 7.10 to select the number of helical springs to have the lowest plastic energy experienced by the back RC panel.

7.3 Summary

The experimental and numerical study applied on the RHR sandwich panel under the free air blast loads reveals the crucial influence of the helical springs interlayer on the blast resistant behavior

of the entire sandwich panel. This study shows the main role of the helical springs interlayer in distributing the energy dissipation process where most of the applied blast energy is dissipated before reaching the back RC panel. In addition, the results indicate that the displacement of the front RC panel and the amount of energy dissipated by each component of the RHR sandwich panel is affected by the helical springs interlayer stiffness. Accordingly, a parametric study is conducted on the helical springs interlayer stiffness. This stiffness is controlled by the number of springs and spring wire diameter hence both these variables are studied. In addition, this study is conducted under different scaled distance. The results show that the average value of the total energy absorbed by the front RC panel and helical springs interlayer is 98 % of the entire applied energy. The results are represented in a form of chart presenting the relationship between the total stiffness of the helical springs interlayer and the maximum displacement of the front RC panel under different scaled distance. By using this chart, blast designers can check whether the designed helical springs reach their closed length or not under the range of scaled distance considered. In addition, another set of charts is presented to obtain the plastic work done by the front and back RC panel of the RHR sandwich panel. By using these charts, blast engineers can obtain the plastic work done of a specific interlayer stiffness and choose the number of helical springs that produce the lower value of the work done by the back RC panel.

Chapter 8: Conclusions and future work

In this Chapter, summary and conclusions are presented and some recommendations for future research are suggested.

8.1 Summary and conclusions

Sandwich blast resistant panels are commonly used to protect vital shallow underground structures. In such assemblies, the front face of the sandwich panel is designed to resist the blast load and the interlayer is designed to prevent the blast energy from reaching the back panel. The objective is to allow the sandwich panel to be repaired efficiently. Hence, the protected underground structure can be used against recurrent blast loads. In the literature, to protect these structures, sand layers have been commonly used as a core layer, within a sandwich assembly, or as a protective layer, sand only (no sandwich assembly). However, the sand layer is usually very heavy and not very efficient in taking additional blast loads due to the plastic behavior of the sand layer. In addition, the existence of moisture/water in the pores decreases the amount of internal energy absorbed by the sand layer as water will prevent the compression process and will be trapped in the pores. Accordingly, in this thesis, a novel sandwich panel, named RC panel - Helical springs- RC panel (RHR) sandwich panel, which consists of normal strength reinforced concrete (RC) panels at the front and back RC panels separated by a number of steel compression helical springs in the middle, is proposed. Before starting the numerical study in this research, a 3D nonlinear numerical study is carried out to evaluate the Riedel-Hiermaier-Thoma (RHT) concrete model ability to simulate the realistic behavior of concrete under various loading conditions. A parametric modification is proposed to identify the best parameters for the RHT model at the material level testing. For the component level testing, the modified RHT model is used to simulate the post softening behavior

of plain concrete (PC) panel under free air blast load. The numerical response is compared with experimental test results. The results show the proposed numerical model can accurately simulate the crack trajectory and the damage pattern of the simply supported PC panel under free air blast load better than the previous modified RHT models, which are found in the literature. Accordingly, a detailed 3D nonlinear numerical analysis is proposed using the nonlinear finite element software, AUTODYN. The accuracy of the developed blast load and RHR Sandwich panel finite element models are validated using experimental results. The results show that the proposed finite element model can be used efficiently and effectively to simulate the nonlinear dynamic behavior of the newly proposed RHR sandwich panels under different ranges of free air blast loads. Subsequently, to evaluate the performance of the RHR sandwich panel against free blast loads, a benchmark study is conducted. The performance of the RHR sandwich panel is compared against the Sand – RC panel (SR) protective system and the RC panel – Sand - RC panel (RSR) sandwich panel. SR protective layer consists of a sand layer and back RC panel. The depth of the sand layer of the SR protective system is the summation of the depth of the front RC panel and helical springs interlayer. Whereas, RSR uses the same configuration as the RHR, except the helical springs are replaced with normal density dry sand layer having the same depth. To achieve that, detailed 3D finite element models of the SR, RSR and RHR are developed using the software ANSYS AUTODYN. The behavior of the RHR is verified using available experimental results, while the behavior of the SR and RSR is verified by validating the dry sand numerical model using previous experimental data. The results show that the RHR has better blast resistant performance in the blast energy dissipation than the SR and RSR under the levels of free blast loads considered. This shows that the newly proposed RHR can be used as an efficient protective layer for the shallow underground structures. Finally, a parametric study is then conducted on the helical springs

interlayer using the validated finite element model. The results show that the helical springs interlayer parameters have a significant effect on the performance of the entire sandwich panel. The selection of the optimum parameters of the springs is mainly controlled by the displacement of the front RC panel and the plastic work done by the front and back RC panels. For the experimental and the numerical study conducted in this thesis, the following observations are obtained:

- Good conformity between the numerical, empirical and experimental results for the free air blast test where the difference between the simulated, calculated and measured peak overpressure values are less than 3 %.
- For the 2D explosion modeling, the difference between the numerical and calculated peak overpressure for 1, 5 and 10 Kg TNT detonated at a SoD of 1 m are 3.4 %, 5.4 %, and 5.9 %, respectively. For the 3D explosion modeling, errors are 8.8 %, 2.7 %, and 5.6 %, respectively. These results show the ability of the developed blast finite element simulation to model a realistic behavior of the explosion process.
- To overcome the difficulty of simulating helical springs in AUTODYN, a 3D solid element model is imported in the AUTODYN program, which revealed a more realistic behavior than the other aforementioned modeling techniques with an acceptable error of 6.7 % when compared with the physical stiffness measured in the factory.
- The numerical simulation of concrete panels under free air blast loads using the proposed RHT model address well the damage pattern and the crack trajectory when compared with the corresponding experimental observations.
- The ability of the developed numerical model of the RHR, RSR and SR protective systems in simulating an accurate behavior under different free air blast loads when

compared with the corresponding experimental results. Good consistency between the observed and simulated maximum displacements and the damage level of the components of the studied protective systems.

- Based on the experimental observation, the RHR sandwich panel can withstand more than one blast shot in the range considered and changing the helical springs interlayer stiffness affects the damage level of the front and back RC panels.
- For the studied range of the scaled distance, no considerable displacements or considerable damage are observed on the back panel of the RHR sandwich panel. In addition, the helical springs still in their elastic state after each blast shot. The average value of the total energy absorbed by the front RC panel and helical springs interlayer is 98 % of the entire applied energy value.
- The helical springs interlayer has a significant role in dissipating a considerable amount of the applied blast energy in a form of elastic energy. On the other hand, the sand layer of the RSR and SR protective systems experienced plastic deformation, which leads to a significant failure of the back RC panel.
- The interlayer of the RHR-16-20-C is 84 % lighter than that of RSR. The total weight of the two first layers of the RHR-16-20-C sandwich panel is 58 % and 59 % lighter than the sand of the SR and the two first layers of the RSR, respectively.
- For the RSR sandwich panel, the damage level observed on the back RC panel under the three different blast loads is more than that observed on the front RC panel due to the existence of the sand layer as a shock-absorbing cushion to the front RC panel. The maximum plastic work done by the back RC panels is greater than that done by the

front RC panel under the three different load cases of 1, 5 and 10 Kg TNT by 98 %, 89 % and 66 %, respectively.

- For the RHR sandwich panel, the helical springs interlayer dissipates an average value of 40.5 % of the total energy dissipated by the entire system in a form of elastic energy. As for the RSR sandwich panel, the dry sand layer dissipates an average value of 51 % of the total energy dissipated by the entire system in a form of plastic energy. The amount of elastic energy dissipated by the helical springs interlayer under the three different blast loads of 1, 5 and 10 Kg TNT is greater than that dissipated by the sand interlayer by 4 %, 70 % and 346 %, respectively.
- The reduction percentage in the plastic work done by the back RC panels when using 16 helical springs in the interlayer under the load cases of 1, 5 and 10 Kg TNT by 99.7 %, 98 % and 73 %, respectively when compared with the RSR sandwich panel and by 99.8 %, 98 % and 66 %, respectively when compared with the SR protective system. This result emphasizes that the RHR sandwich panel can protect the back RC panel significantly more than the SR and RSR protective systems.
- The maximum total energy dissipated by the front RC panel of the RHR sandwich panel under the three different blast loads of 1, 5 and 10 Kg TNT is greater than that dissipated by the front RC panel of the RSR sandwich panel by 95 %, 112 % and 141 %, respectively.
- The reduction percentage between the maximum normal stress values applied on the front face of the front and back RC panels of the RHR are 91 %, 94 % and 94 % in the blast loading cases 1, 5 and 10 Kg TNT, respectively. As for the RSR sandwich panel, the maximum normal stress is decreased by 60 %, 69 % and 65 % under the blast

loading cases 1, 5 and 10 Kg TNT, respectively. As for the SR, the maximum normal stress is decreased by 25 %, 59 and 61 % under the blast loading cases 1, 5 and 10 Kg TNT, respectively.

- The average reduction percentages between the peak overpressure values at the front face of the front RC panel and back face of the back RC panel of the RHR sandwich panel under the considered range of the blast loads are 93 %, 96 %, and 97 %, respectively.
- The best number of helical springs that can be used as an interlayer for the RHR sandwich panel, under the studied scaled distance, is 25 helical springs. This is attributed to the highest reduction percentage of the maximum displacement of the front RC panel, under the studied scaled distance.
- Based on the maximum displacement of the front RC panel and the plastic work done by the front and the back RC panels for the studied RHR sandwich panels, it can be observed that the best range of the stiffness of helical springs interlayer is between 700 to 1400 N/mm. Hence, designing the helical springs within this range will optimal the blast resistant behavior of the entire RHR sandwich panel under the range of blast load considered.

Overall, this thesis has demonstrated that the newly proposed RHR sandwich panel has superior performance when compared with the SR and RSR protective systems under the three levels of blast load considered. Hence, it can be used as a potentially effective protective layer for the vital shallow underground structures. Accordingly, a parametric study is carried out and the results are expressed in a form of chart presenting the relationship between the total stiffness of the helical

springs interlayer and the maximum displacement of the front RC panel for different scaled distance. Lastly, design charts are presented to obtain the plastic work done by the front and back RC panel of a RHR sandwich panel under different blast loads.

8.2 Recommendations for future work

In this section, several recommendations are proposed for future research based on the contributions presented in this thesis. The following research directions can be investigated:

- In this research, a single layer of helical springs is used in the interlayer of the proposed RHR sandwich panel. A new studying is proposed to investigate the effect of using multi-layers of helical springs, having the same stiffness of the single layer, on the displacement and the amount of the energy dissipated by each component of the RHR sandwich panel.
- In this study, a parametric study is conducted on the RHR sandwich panel by changing different parameters of the interlayer against different scaled distance. A similar parametric study is recommended to investigate the performance of the RHR sandwich panel when changing the front RC panel parameters like compression strength, reinforcement, adding fibers or replacing it with a steel sandwich panel with different core structures like honeycomb and square shape.
- In this thesis, an experimental test is conducted on a scaled RHR sandwich panel under different blast loads. A similar experimental application is suggested to be conducted on a full-scale shallow tunnel or underground structure to obtain a large scale data about the behavior of this proposed protective layer which accordingly, will provide the blast resistant designer with an accurate field date.

- In this study, a detailed 3D solid element is used to simulate the response of the helical springs. The result shows such modeling can effectively simulate the response of the helical spring well. It should be noted, though the proposed modeling approach can be used to model the response well, it is recommended that other simpler models, such as shell element or lump hinge models, should be developed to improve the computation efficiency.
- In this study, the RHT model implemented in AUTODYN is used to model the concrete material under free air blast loads. The simulation result shows that the proposed model can simulate the damage level and the crack trajectory of a simply supported plain concrete panel under free air blast load. It is recommended that such a model be used to simulate the hyperdynamic response of different concrete structures under different boundary conditions.

Bibliography

- Anderson, C.E., 1987. An overview of the theory of hydrocodes. *Int. J. Impact Eng.*
[https://doi.org/10.1016/0734-743X\(87\)90029-7](https://doi.org/10.1016/0734-743X(87)90029-7)
- ANSYS-AUTODYN, 2005. Interactive non-linear dynamic analysis software, version 16, user's manual. Century Dynamics Inc.
- ANSYS, 2007. Theory reference manual. Release 11.0. ANSYS Inc.
- Autodesk Inventor Professional manual, 2010.
- Baker, W.E., 1973. Explosions in Air, Development.
- Benson, D.J., 1992. Computational methods in Lagrangian and Eulerian hydrocode. *Comput. Methods Appl. Mech. Eng.* 99, 2356.
- Benson, D.J., 1990. Computer Methods in Lagrangian and Eulerian Hydrocodes 99, 235–394.
[https://doi.org/10.1016/0045-7825\(92\)90042-i](https://doi.org/10.1016/0045-7825(92)90042-i)
- Bergeron, D., Walker, R., Coffey, C., 1998. Detonation of 100-gram anti-personnel mine surrogate charges in sand - a test case for computer code validation.
- Cheeseman, B.A., Wolf, S., Yen, C.F., Skaggs, R., 2006. Blast simulation of explosives buried in saturated sand. *Fragblast*. <https://doi.org/10.1080/13855140500432045>
- Chen W. F., 1982. *Plasticity in Reinforced Concrete*. McGraw-Hill, New York.
- Codina, R., Ambrosini, D., de Borbón, F., 2016. Experimental and numerical study of a RC member under a close-in blast loading. *Eng. Struct.* 127, 145–158.
<https://doi.org/10.1016/j.engstruct.2016.08.035>
- CONWEP (Conventional Weapons Effects) Computer Software Produced by the U.S. Army Waterways. Experimental Station. Mississippi. USA; 1990.
- Fairlie, G., Bergeron, D., 2002. Numerical simulation of mine blast loading on structures. 17th

Mil. Asp. Blast Symp.

- Fiserova, D., 2006. Numerical analysis of buried mine explosions with emphasis on effect of soil properties on loading. Cranfield University, Cranfield.
- Gebbeken, N., Ruppert, M., 2000. A new material model for concrete in high-dynamic hydrocode simulations. *Arch. Appl. Mech.* 70, 463–478. <https://doi.org/10.1007/s004190000079>
- Goel, M.D., Matsagar, V.A., 2014. Blast-Resistant Design of Structures. *Pract. Period. Struct. Des. Constr.* 19, 04014007. [https://doi.org/10.1061/\(ASCE\)SC.1943-5576.0000188](https://doi.org/10.1061/(ASCE)SC.1943-5576.0000188)
- Govindjee S, Gregory JK, S.J., 1995. Anisotropic modeling and numerical-simulation of brittle damage in concrete. *Int. J. Numer. Methods Eng.* 38, 3611–33.
- Grujicic, M., Pandurangan, B., Cheeseman, B.A., 2006a. A Computational Analysis of Detonation of Buried Mines. *Multidiscip. Model. Mater. Struct.* <https://doi.org/10.1163/157361106778554851>
- Grujicic, M., Pandurangan, B., Cheeseman, B.A., 2006b. The effect of degree of saturation of sand on detonation phenomena associated with shallow-buried and ground-laid mines. *Shock Vib.* <https://doi.org/10.1155/2006/652405>
- Grujicic, M., Pandurangan, B., Huang, Y., Cheeseman, B.A., Roy, W.N., Skaggs, R.R., 2007. Impulse loading resulting from shallow buried explosives in water-saturated sand. *Proc. Inst. Mech. Eng. Part L J. Mater. Des. Appl.* <https://doi.org/10.1243/14644207JMDA96>
- Grujicic, M., Pandurangan, B., Summers, J.D., Cheeseman, B.A., Roy, W.N., Skaggs, R.R., 2008. Application of the modified compaction material model to the analysis of landmine detonation in soil with various degrees of water saturation. *Shock Vib.* <https://doi.org/10.1155/2008/765494>
- Hao, H., Ma, G., Zhou, Y., 1998. Numerical simulation of underground explosions. *Fragblast* 2,

383–395. <https://doi.org/10.1080/13855149809408784>

Henrych, J., 1979. The dynamics of explosion and its use. Elsevier Publications, New York.

Hentz, S., Donzé, F. V., Daudeville, L., 2004. Discrete element modelling of concrete submitted to dynamic loading at high strain rates. *Comput. Struct.* 82, 2509–2524. <https://doi.org/10.1016/j.compstruc.2004.05.016>

Herrmann, W., 1969. Constitutive equation for the dynamic compaction of ductile porous materials. *J. Appl. Phys.* 40, 2490–2499. <https://doi.org/10.1063/1.1658021>

Hooke, R., G. T, G. T, Papin, D., Sturmy, S., Young, J., 1678. Lectures de potentia restitutiva, or, Of spring : explaining the power of springing bodies. London.

Hopkinson, B., 1915. British ordnance board minutes 13565. *Natl. Arch.* Kew, UK.

Hu, G., Wu, J., Li, L., 2016. Advanced Concrete Model in Hydrocode to Simulate Concrete Structures under Blast Loading. *Adv. Civ. Eng.* 2016. <https://doi.org/10.1155/2016/7540151>

Johnson, G.G.R., Cook, W.H.W., 1983. A constitutive model and data for metals subjected to large strains, high strain rates and high temperatures. 7th Int. Symp. Ballist. <https://doi.org/10.1038/nrm3209>

Karlos, V., Solomon, G., 2013. Calculation of blast loads for application to structural components, Publications Office of the European Union. <https://doi.org/10.2788/61866>

Laine, L., Sandvik, A., 2001. DERIVATION OF MECHANICAL PROPERTIES FOR SAND. 4th Asia-Pacific Conf. Shock Impact Loads Struct.

Larcher, M., Gebbeken, N., 2012. Development of EOS data for granular material like sand by using micromodels. *EPJ Web Conf.* <https://doi.org/10.1051/epjconf/20122604005>

Li, X., Miao, C., Wang, Q., Geng, Z., 2016. Antiknock Performance of Interlayered High-Damping-Rubber Blast Door under Thermobaric Shock Wave. *Shock Vib.* 2016.

<https://doi.org/10.1155/2016/2420893>

- Li, X., Zhang, P., Wang, Z., Wu, G., Zhao, L., 2014. Dynamic behavior of aluminum honeycomb sandwich panels under air blast: Experiment and numerical analysis. *Compos. Struct.* 108, 1001–1008. <https://doi.org/10.1016/j.compstruct.2013.10.034>
- Loret, B., Khalili, N., 2000. A three-phase model for unsaturated soils. *Int. J. Numer. Anal. Methods Geomech.* [https://doi.org/10.1002/1096-9853\(200009\)24:11<893::AID-NAG105>3.0.CO;2-V](https://doi.org/10.1002/1096-9853(200009)24:11<893::AID-NAG105>3.0.CO;2-V)
- Lu, X., Hsu, C.-T.T., 2007. Stress-Strain Relations of High-Strength Concrete under Triaxial Compression. *J. Mater. Civ. Eng.* [https://doi.org/10.1061/\(asce\)0899-1561\(2007\)19:3\(261\)](https://doi.org/10.1061/(asce)0899-1561(2007)19:3(261))
- Luccioni B, Araoz G, L.N., 2013. Defining Erosion Limit for Concrete.pdf. *Int. J. Protective structures* 4, 315–340. <https://doi.org/10.1260/2041-4196.4.3.315>
- Malvar, L.J., Crawford, J.E., Wesevich, J.W., Simons, D., 1997. A plasticity concrete material model for DYNA3D. *Int. J. Impact Eng.* 19, 847–873. [https://doi.org/10.1016/S0734-743X\(97\)00023-7](https://doi.org/10.1016/S0734-743X(97)00023-7)
- Matsagar, V.A., 2016. Comparative performance of composite sandwich panels and non-composite panels under blast loading. *Mater. Struct.* 49, 611–629. <https://doi.org/10.1617/s11527-015-0523-8>
- Mazek, S.A., 2014. Performance of sandwich structure strengthened by pyramid cover under blast effect. *Struct. Eng. Mech.* <https://doi.org/10.12989/sem.2014.50.4.471>
- Mazek, S.A., Mostafa, A.A., 2013. Impact of a shock wave on a structure strengthened by rigid polyurethane foam. *Struct. Eng. Mech.* <https://doi.org/10.12989/sem.2013.48.4.569>
- Ngo, T., Mendis, P., Gupta, A., Ramsay, J., 2007. Blast loading and blast effects on structures - An overview. *Electron. J. Struct. Eng.*

- Nurick, G.N., Langdon, G.S., Chi, Y., Jacob, N., 2009. Behaviour of sandwich panels subjected to intense air blast - Part 1: Experiments. *Compos. Struct.* <https://doi.org/10.1016/j.compstruct.2009.04.009>
- Nyström, U., Gylltoft, K., 2011. Comparative numerical studies of projectile impacts on plain and steel-fibre reinforced concrete. *Int. J. Impact Eng.* 38, 95–105. <https://doi.org/10.1016/j.ijimpeng.2010.10.003>
- Nyström, U., Gylltoft, K., 2009. Numerical studies of the combined effects of blast and fragment loading. *Int. J. Impact Eng.* 36, 995–1005. <https://doi.org/10.1016/j.ijimpeng.2009.02.008>
- Pickering, E.G., Chung Kim Yuen, S., Nurick, G.N., Haw, P., 2012. The response of quadrangular plates to buried charges. *Int. J. Impact Eng.* <https://doi.org/10.1016/j.ijimpeng.2012.05.007>
- Prawoto, Y., Ikeda, M., Manville, S.K., Nishikawa, A., 2008. Design and failure modes of automotive suspension springs. *Eng. Fail. Anal.* 15, 1155–1174. <https://doi.org/10.1016/j.engfailanal.2007.11.003>
- Rashad, M., 2013. Study the Behavior of Composite Sandwich Structural Panels Under Explosion Using Finite Element Method. M.Sc. thesis, Military Technical College (MTC), Cairo. [https://doi.org/10.1016/S0422-9894\(08\)71343-6](https://doi.org/10.1016/S0422-9894(08)71343-6)
- Riedel W, Thoma K, H.S., 1999. Penetration of reinforced concrete by BETA-B-500 numerical analysis using a new macroscopic concrete model for hydrocodes, in: *In: Proceedings of 9th International Symposium on Interaction of the Effect of Munitions with Structures. Berlin-Strausberg*, pp. 315–22.
- Riedel, W., 2009. 10 years RHT: A review of concrete modelling and hydrocode applications, in: *Predictive Modeling of Dynamic Processes: A Tribute to Professor Klaus Thoma.* https://doi.org/10.1007/978-1-4419-0727-1_9

- Riedel, W., 2000. Beton unter dynamischen Lasten Meso- und makromechanische Modelle und ihre Parameter. der Bundeswehr Munchen, Freiburg.
- Riedel, W., Kawai, N., Kondo, K., 2009. Numerical assessment for impact strength measurements in concrete materials. *Int. J. Impact Eng.* 36, 283–293.
<https://doi.org/10.1016/j.ijimpeng.2007.12.012>
- Riedel, W., Wicklein, M., Thoma, K., 2008. Shock properties of conventional and high strength concrete: Experimental and mesomechanical analysis. *Int. J. Impact Eng.* 35, 155–171.
<https://doi.org/10.1016/j.ijimpeng.2007.02.001>
- Roser, M., Nagdy, M., Ritchie, H., 2019. Terrorism [WWW Document]. Our World Data. URL <https://ourworldindata.org/terrorism>
- Shimozaki, M., 1997. FEM for springs. Japan Society of Spring Engineers. [In Japanese], Nikkan Kogyo Shimbunsha.
- TM5-1300 (Structures to resist the effects of accidental explosions), 1990.
- Tu, Z., Lu, Y., 2010. Modifications of RHT material model for improved numerical simulation of dynamic response of concrete. *Int. J. Impact Eng.* 37, 1072–1082.
<https://doi.org/10.1016/j.ijimpeng.2010.04.004>
- Tu, Z., Lu, Y., 2009. Evaluation of typical concrete material models used in hydrocodes for high dynamic response simulations. *Int. J. Impact Eng.* 36, 132–146.
<https://doi.org/10.1016/j.ijimpeng.2007.12.010>
- UFC 3-340-02, 2008. Structures to Resist the Effects of Accidental Explosions. *Struct. Congr.* 2011 1867. [https://doi.org/10.1061/41171\(401\)127](https://doi.org/10.1061/41171(401)127)
- Vinson, J.R., 2001. Sandwich Structures Construction. *Appl. Mech. Rev.* 54, 201–214.
- Wahab, M.M.A., Mazek, S.A., 2016. Performance of double reinforced concrete panel against

- blast hazard. *Comput. Concr.* 18, 807–826. <https://doi.org/10.12989/cac.2016.18.4.807>
- Wahl, A., 1963. *Mechanical springs*, 2nd edn. McGraw- Hill, New York.
- Wang, W., Zhang, D., Lu, F., Wang, S. chuan, Tang, F., 2013. Experimental study and numerical simulation of the damage mode of a square reinforced concrete slab under close-in explosion. *Eng. Fail. Anal.* 27, 41–51. <https://doi.org/10.1016/j.engfailanal.2012.07.010>
- Wu, C., Hao, H., Lu, Y., Sun, S., 2004. Numerical simulation of structural responses on a sand layer to blast induced ground excitations. *Comput. Struct.* <https://doi.org/10.1016/j.compstruc.2004.01.003>
- Wu, C., Hao, H., Ma, G., Zhou, Y., 1999. Dynamic response analysis of rock mass with stochastic properties subjected to explosive loads. *Fragblast.* <https://doi.org/10.1080/13855149909408041>
- Xia, Z., Wang, X., Fan, H., Li, Y., Jin, F., 2016. Blast resistance of metallic tube-core sandwich panels. *Int. J. Impact Eng.* <https://doi.org/10.1016/j.ijimpeng.2016.06.001>
- Xu, K., Lu, Y., 2006. Numerical simulation study of spallation in reinforced concrete plates subjected to blast loading. *Comput. Struct.* 84, 431–438. <https://doi.org/10.1016/j.compstruc.2005.09.029>
- Yandzio, E., Gough, M., 1999. *Protection of buildings against explosions*. Ascot: Steel Construction Institute.
- Zhang, M.H., Sharif, M.S.H., Lu, G., 2007. Impact resistance of high-strength fibre-reinforced concrete. *Mag. Concr. Res.* <https://doi.org/10.1680/mac.2007.59.3.199>
- Zhou, X.Q., Hao, H., 2008. Numerical prediction of reinforced concrete exterior wall response to blast loading. *Adv. Struct. Eng.* 11, 355–367. <https://doi.org/10.1260/136943308785836826>
- Zhou, X.Q., Kuznetsov, V.A., Hao, H., Waschl, J., 2008. Numerical prediction of concrete slab

response to blast loading. *Int. J. Impact Eng.* 35, 1186–1200.

<https://doi.org/10.1016/j.ijimpeng.2008.01.004>

Zhu, F., 2008. Impulsive loading of sandwich panels with cellular cores. Swinburne University of Technology, Faculty of Engineering and Industrial Sciences.

Zukas, J.A., 2004. Introduction to hydrocodes. *Stud. Appl. Mech.*